

THE POLARIZATION AND MAGNETIC MOMENT OF THE
SIGMA MINUS HYPERON

By LESLIE LUDWIG DECK

A thesis submitted to

The Graduate School

of

Rutgers, The State University of New Jersey

in partial fulfillment of the requirements

for the degree of

Doctor of Philosophy

Graduate Program in Physics

Written under the direction of

Professor Thomas J. Devlin

and approved by

Thomas J. Devlin
Terence L. Watts
Eric S. Swanson
Ronald Rockmore

New Brunswick, New Jersey

November 1981

ABSTRACT OF THE THESIS

The Polarization and Magnetic Moment of the

Sigma Minus Hyperon

by LESLIE LUDWIG DECK

Thesis Director : Professor Thomas J. Devlin

The magnitude of the polarization of 516,229 inclusively produced Σ^- 's has been measured to be $15.5 \pm 3.6\%$. The Σ^- 's were produced by 400 GeV/c protons on Be at angles of ± 7.5 mr with respect to the incident proton direction and had momenta between 120 and 290 GeV/c, with a mean momentum of 176 GeV/c. The polarization was measured from the asymmetry in the decay $\Sigma^- \rightarrow n + \pi^-$.

The Σ^- magnetic moment was also determined to be $-0.89 \pm 0.14 \mu_N$ corresponding to an anomalous precession angle of $11^\circ \pm 15^\circ$.

ACKNOWLEDGEMENTS

I would like to thank my thesis advisor, Tom Devlin, for introducing me to experimental high energy physics and for his support, advice and constant optimism during the experiment and analysis.

All the members of the neutral hyperon group contributed to this project and special thanks go to Regina Rameika, Byron Lundberg, Craig Dukes and Bill Luk for their help with the data taking, and discussions thereafter.

Bob Handler was an inexhaustable supply of expertise and experience throughout the experiment and subsequent analysis.

Many thanks also go to Lee Pondrom, Andy Beretvas and Marleigh Sheaff for many helpful suggestions and discussions.

I would especially like to thank my wife, Siegi, without whose patience and support this project could not have been completed.

TABLE OF CONTENTS

	page
ABSTRACT	ii
ACKNOWLEDGEMENTS	iii
TABLE OF CONTENTS	iv
LIST OF TABLES	vi
LIST OF FIGURES	vii
1. INTRODUCTION	1
1. Theoretical Background	5
1. Polarization	5
2. Magnetic Moments	6
2. Experimental Background	13
2. THE SPECTROMETER AND APPARATUS	19
1. The Beam Delivery System	19
2. The Apparatus	22
1. The Target Area	22
2. The Charged Beam Collimator	25
3. The Spectrometer	28
1. The Drift Chambers	32
1. Calibration	33
2. Performance	35
3. The Trigger Logic	37
4. The Data Acquisition System	38
3. DATA ANALYSIS I : EVENT RECONSTRUCTION	40
1. Reconstruction Program and Data Summary Tapes	40

2.	The Data Set	44
3.	Event Analysis	46
4.	Event Selection	49
5.	Backgrounds	59
4.	DATA ANALYSIS II : POLARIZATION ANALYSIS	71
1.	Polarization Analysis	71
2.	Polarization and Biases	73
3.	Polarization Results	87
4.	Precession Analysis and Magnetic Moment	87
5.	Systematics	91
6.	Time Dependent Systematics	92
5.	RESULTS	99
6.	APPENDIX	101
1.	The External Monte Carlo	101
2.	The Nonuniformity of the M3 Field Integral	104
3.	The Hybrid Monte Carlo Method	107
4.	The Effect of Backgrounds on the Asymmetry Calculation	113
	REFERENCES	121
	VITA	124

LIST OF TABLES

	page
1. The up, down, and strange quark quantum numbers.	7
2. The stable baryon SU(6) wavefunctions.	9
3. The stable baryon magnetic moments both measured and predicted.	11
4. The quark magnetic moments and masses in the broken SU(6) model.	11
5. A number of theoretical predictions for the Σ^- magnetic moment.	12
6. The drift chamber resolutions and efficiencies.	36
7. The polarization signals and biases for the two Σ^- categories in both data sets.	78
8. The X,Y and Z polarization signals and biases for all the data.	79
9. The polarization magnitudes for all the data.	87
10. The four lowest order precession configurations and their moments.	91
11. The "polarization" signals for the data when determining time dependent effects.	98

LIST OF FIGURES

	page
1. The M2 proton beam transport system.	21
2. Plan view of the M2 charged hyperon spectrometer and apparatus as configured for this experiment.	23
3. The hyperon production target area and associated detectors.	24
4. The plan and elevation views of the M2 charged hyperon beam channel.	26
5. The relative momentum acceptance of the M2 beam channel for $\int \vec{B} \cdot d\vec{l} = 1.8 \text{ GeV}/c$.	27
6. The neutron precalorimeter with associated detectors.	31
7. A typical drift chamber calibration curve.	34
8. The reconstruction efficiency as a function of decay vertex.	43
9. The geometric χ^2 distribution.	50
10. The Σ^- momentum distribution.	52
11. The decay π^- momentum distribution.	53
12. The reconstructed decay vertex distribution for Monte Carlo generated straight tracks.	54
13. The Σ^- decay vertex distribution.	56
14. The kinematic χ^2 distribution.	57
15. The Σ^- mass distribution.	58
16. The angle θ_y between the Σ^- momentum and the xz plane for events that satisfy all Σ^- cuts.	61
17. The spectrometer acceptance curves for the decays, $\Sigma^- \rightarrow n \pi^-$, $\Xi^- \rightarrow \Lambda^0 \pi^-$ and $K^- \rightarrow \pi^0 \pi^-$.	62

18. A missing mass distribution for the hypothesis $\Xi^- \rightarrow \Lambda^0 \pi^-$, before and after Σ^- cuts. 64
19. The missing mass distribution for the hypothesis $K^- \rightarrow \pi^0 \pi^-$ before cuts. Also shown is a MC calculation for simulated $K^- \rightarrow \pi^0 \pi^-$ events normalized to 0.5% of the real data. 66
20. A $\Sigma^- - \pi^-$ opening angle comparison plot between real and Monte Carlo data. 68
21. The pulse height distribution of the sum of neutron precalorimeter counters 3, 4 and 5 for events that satisfy all cuts. 69
22. An illustration of the Σ^- spin precession in the M2 field. 74
23. The values of αP_x determined for the several Σ^- categories. 76
24. The values of αP_z determined for the several Σ^- categories. 77
25. The x, y and z biases for all the data. 80
26. The neutron y distributions at the neutron precalorimeter for the two production angles. 83
27. The neutron x distributions at the neutron precalorimeter for the two production angles. 85
28. The magnitude of the polarization for all the data. 88
29. The four lowest order precession configurations. 90
30. The variation of the magnetic moment for different values of the cut on the kinematic χ^2 . 93
31. The variation of the magnetic moment for different values of the cut on the NC pulse height distribution. 94
32. The magnetic moment calculated for three different decay vertex bins. 95

33. The magnetic moment as a function of momentum. 96
34. The $\cos(\theta_x)$ distribution of neutrons in the Σ^- rest frame for $\Sigma^- \rightarrow n\pi^-$ decay. The distributions from both production angles are given. For comparison the distribution of the Internal Monte Carlo events is also shown. 110
35. The $\cos(\theta_y)$ distribution of neutrons in the Σ^- rest frame for $\Sigma^- \rightarrow n\pi^-$ decay. The distributions from both production angles are given. For comparison the distribution of the Internal Monte Carlo events is also shown. 111
36. The $\cos(\theta_z)$ distribution of neutrons in the Σ^- rest frame for $\Sigma^- \rightarrow n\pi^-$ decay. The distributions from both production angles are given. For comparison the distribution of the Internal Monte Carlo events is also shown. 112
37. The $\cos(\theta_x)$ distribution for the "neutrons" from MC $\Xi^- \rightarrow \Lambda^0 \pi^-$ events reconstructed as $\Sigma^- \rightarrow n\pi^-$. 114
38. The $\cos(\theta_z)$ distribution for the "neutrons" from MC $\Xi^- \rightarrow \Lambda^0 \pi^-$ events reconstructed as $\Sigma^- \rightarrow n\pi^-$. 115

CHAPTER 1

INTRODUCTION

The study of magnetic moments in elementary particle physics has been rich and rewarding. The determination of the electron and muon moments to very high precision has provided major evidence in support of Q.E.D. Moments have given us insight into the substructure of hadrons as shown by the remarkable success of the broken SU(6) quark model in predicting some of these moments to a few percent. Only greater precision in the experimental measurements can test further modifications to SU(6) or any other theory developed to understand these particles.

A magnetic moment is defined by:

$$\vec{\mu} = \frac{g}{2} \frac{e}{mc} \vec{S} \quad (1)$$

and for baryons is conventionally expressed in units of nuclear magnetons ($\mu_N = e\hbar/2m_p c = 3.1524515(53) \times 10^{-8}$ MeV/gauss) or intrinsic magnetons if the mass of the particle is used instead of the proton mass. Electron moments are expressed in Bohr magnetons ($\mu_B = e\hbar/2m_e c = 5.7883785(95) \times 10^{-15}$ MeV/gauss). (1)

Equation (1) implies that the quantity g , called the g -factor, is essentially a measure of the magnetic moment. In the Dirac theory of spin-1/2 particles the g -factor has special significance. Charged point-like fermions should have $g=2$, neutral ones $g=0$. Departure from those values indicate an underlying structure to the particle. This structure may take the form of bound subparticle states (quarks) or indicate the presence of internal forces or interactions. The electron and muon g -factors are very close to 2 indicating their point-like structure. The latest deep-inelastic scattering experiments show that all the charged leptons have no structure down to 10^{-16} cm. (2) On the other hand the proton and neutron g -factors differ appreciably from 2 and 0 and these particles are thus said

to have large "anomalous" moments.

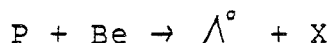
Magnetic moments of elementary particles are a purely quantum concept since they describe the interaction between a particle's spin and an external magnetic field. In particular if a particle with magnetic moment $\vec{\mu}$ and spin \vec{S} is in a magnetic field of strength \vec{B} , the spin vector precesses according to the equation,

$$\frac{d\vec{S}}{dt} = \vec{\mu} \times \vec{B}. \quad (2)$$

Equation (2) is pivotal to this experiment. It means that a polarized sample of Σ^- 's can be used to measure the Σ^- magnetic moment. If a particle is made up of many subparticles, much can be learned about the relative spin and angular momentum states of the subparticles by measuring the magnetic moment of the combined system. Historically this helped in determining the various angular momentum states of the deuteron. The procedure would be similar with elementary particles if the existence of quarks is assumed. The only difference is that free quarks have not been isolated and so their moments can not be found independently. Thus they must be inferred from the moments of the different particles they form - a very difficult proposition even when the moments

of the composite systems are well known.

In 1976 it was discovered at Fermilab that inclusively produced Λ^0 's in the reaction :



were polarized.⁽³⁾ Polarization of inclusively produced Λ^0 's has also been reported at both Brookhaven National Lab. and CERN.^(4,5) Since then polarization of inclusively produced Ξ^0 , Ξ^- and Σ^+ has been measured at Fermilab.^(6,7,8) Thus if Σ^- 's are also produced polarized, a direct approach to the problem of measuring the Σ^- magnetic moment would be found. This report constitutes the first observation of the polarization of inclusively produced Σ^- 's and a measure of the Σ^- magnetic moment by this technique.

1.1 THEORETICAL BACKGROUND

1.1.1 POLARIZATION

Before 1976, polarization of inclusively produced hyperons at high energy was a completely unexpected phenomena. It was originally thought that spin-dependent forces were negligible compared to the strong force between hadrons, and therefore some believed the observed polarization to be a nuclear effect. Subsequent experiments however showed that this is not the case.⁽⁹⁾ A number of models have been proposed to explain this polarization.

One model ascribes the polarization to a Thomas precession of the quark spins when they recombine to form the hyperon after the collision.⁽¹⁰⁾ This model predicts the Ξ^0 , Ξ^- and Σ^- polarizations to lie in the same direction as the Λ^0 .

Another model, based on the assumption that the carrier of the polarization is the s quark (the heavy quark), predicts the Σ^- and Σ^+ polarizations to be opposite the Λ^0 .⁽¹¹⁾ This experiment suggests that the Σ^- polarization is opposite to the Λ^0 , in agreement with the latter model.

1.1.2 MAGNETIC MOMENTS

One model of elementary particle structure that predicts the baryon magnetic moments in reasonable agreement with experiment is the SU(6) quark model. Other models, such as the bag model, give essentially the same results as SU(6), so SU(6) has been chosen as representative. In this model all baryons are formed from symmetric s-wave combinations of 3 quarks whose quantum numbers add up to those of the baryons. See Table 1 for a list of the quark quantum numbers (charge, isospin and strangeness) in the SU(6) model.⁽¹²⁾

	u	d	s
q/e	2/3	-1/3	-1/3
I	1/2	-1/2	0
S	0	0	-1

Table 1 The up, down, and strange quark quantum numbers.

As an example consider the Σ^- . In the quark model it is made up of 2 d quarks and 1 s quark in various spin and angular momentum states consistent with Fermi statistics and the observed spin of the Σ^- . The magnetic moments of these quantum systems are found via:

$$\mu_B = \langle B | \sum_i \mu_i | B \rangle \quad (3)$$

where $|B\rangle$ represents the baryon wavefunction, the μ_i are the quark magnetic moment operators and the sum runs over the three quark flavors. The baryon quark wavefunctions are given in Table 2. An application of equation (3) gives expressions for the baryon moments in terms of the quark moments. A few examples are:

$$\begin{aligned} \mu_p &= 4/3 \mu_u - 1/3 \mu_d \\ \mu_n &= 4/3 \mu_d - 1/3 \mu_u \\ \mu_{\Sigma^-} &= 4/3 \mu_d - 1/3 \mu_s \end{aligned} \quad (4)$$

If SU(6) were an exact symmetry then the quark moments would be proportional only to their charge. ie:

$$\mu_i = \mu_0 Q_i \sigma_i \quad (5)$$

where μ_0 is the intrinsic quark magnetic moment, Q_i is the charge operator and σ_i is the spin operator (the standard Pauli spin matrices). Equations (4) and (5) can now be used to calculate the baryon moments if the assumption that $g=2$ is made for quarks. These are given under the exact SU(6) column in Table 3. (1,7,13)

In 1977 a Rutgers, Michigan, Wisconsin collaboration at Fermilab measured the Λ^0 magnetic moment to high precision and confirmed a marked disagreement with the measured value and the exact SU(6) prediction. (14) An attempt to "clean up" this model can be made by relaxing the somewhat naive restriction that the symmetry be exact. This has the effect of giving the quarks different masses which in turn changes their moments. The results of this calculation are given in the broken SU(6) column in Table 3. Notice that the proton, neutron and Λ^0 moments form the three equations needed to determine the three quark masses found in Table 4. The quark moments can then be calculated using equation (1). The Σ^- moment is then

predicted to be -1.091 nuclear magnetons. This is about 1.4σ away from the result reported here.

BARYON	3 x SU(6) WAVEFUNCTION (perm. omitted)
p	$\frac{\sqrt{2/3}}{\sqrt{2}} (u\uparrow u\downarrow + u\downarrow u\uparrow) d\uparrow - \frac{\sqrt{1/3}}{\sqrt{2}} (u\uparrow u\downarrow + u\downarrow u\uparrow) d\uparrow / \sqrt{2}$
n	$\frac{\sqrt{2/3}}{\sqrt{2}} (d\uparrow d\downarrow + d\downarrow d\uparrow) u\uparrow - \frac{\sqrt{1/3}}{\sqrt{2}} (d\uparrow d\downarrow + d\downarrow d\uparrow) u\uparrow / \sqrt{2}$
Σ^+	$\frac{\sqrt{2/3}}{\sqrt{2}} (u\uparrow u\downarrow + u\downarrow u\uparrow) s\uparrow - \frac{\sqrt{1/3}}{\sqrt{2}} (u\uparrow u\downarrow + u\downarrow u\uparrow) s\uparrow / \sqrt{2}$
Σ^0	$\frac{\sqrt{2/3}}{\sqrt{2}} (u\uparrow d\downarrow + u\downarrow d\uparrow) s\uparrow - \frac{\sqrt{1/3}}{\sqrt{2}} (u\uparrow d\downarrow + u\downarrow d\uparrow) s\uparrow / \sqrt{2}$
Σ^-	$\frac{\sqrt{2/3}}{\sqrt{2}} (d\uparrow d\downarrow + d\downarrow d\uparrow) s\uparrow - \frac{\sqrt{1/3}}{\sqrt{2}} (d\uparrow d\downarrow + d\downarrow d\uparrow) s\uparrow / \sqrt{2}$
Ξ^0	$\frac{\sqrt{2/3}}{\sqrt{2}} (s\uparrow s\downarrow + s\downarrow s\uparrow) u\uparrow - \frac{\sqrt{1/3}}{\sqrt{2}} (s\uparrow s\downarrow + s\downarrow s\uparrow) u\uparrow / \sqrt{2}$
Ξ^-	$\frac{\sqrt{2/3}}{\sqrt{2}} (s\uparrow s\downarrow + s\downarrow s\uparrow) d\uparrow - \frac{\sqrt{1/3}}{\sqrt{2}} (s\uparrow s\downarrow + s\downarrow s\uparrow) d\uparrow / \sqrt{2}$
Λ^0	$(u\uparrow d\downarrow - u\downarrow d\uparrow) s\uparrow / \sqrt{2}$
Ω^-	$s\uparrow s\uparrow s\uparrow$

Table 2 The stable baryon SU(6) wavefunctions.

The basic SU(6) model has been discussed with symmetry breaking as a refinement. Further refinements to obtain better agreement with the data are possible. These include configuration mixing, anomalous quark moments, relativistic effects and the effect of pion clouds. (15,16) All have been tried alone and in various combinations but none give really satisfactory agreement with all the data

to the level of the experimental errors. The value of the Σ^- magnetic moment predicted from these corrections ranges from $-.69\mu_N$ to $-1.37\mu_N$, thus it is clear that a precise measurement of the Σ^- magnetic moment is necessary to choose amongst these models.

More recently a sum rule based on the flavor independence of the baryon-quark wavefunctions relating the Σ^- , Σ^+ , Ξ^- and Ξ^0 moments has been derived that predicts the Σ^- moment to be $-0.81 \pm 0.14\mu_N$.⁽¹⁷⁾ Also, a treatment of the hyperon magnetic moments using only the SU(6) group-theoretic properties predicts $-.82\mu_N$ for the Σ^- magnetic moment.⁽¹⁸⁾ Both of these predictions are in good agreement with the result reported here. A list of predictions for the Σ^- magnetic moment from several theories is given in Table 5.

MAGNETIC MOMENT (n.m.)

BARYON	EXPERIMENT	EXACT SU(6)	BROKEN SU(6)
p	2.793	input	input
n	-1.913	-1.86	input
Λ^0	-0.6138 ± 0.0047	-0.93	input
Σ^+	2.33 ± 0.13	2.79	2.67
$\Sigma^0 \rightarrow \Lambda^0 \gamma$	$-1.82^{+0.25}_{-0.18}$	-1.61	-1.63
Σ^-	-0.89 ± 0.14	-0.93	-1.09
Ξ^0	-1.253 ± 0.014	-1.86	-1.44
Ξ^-	-0.75 ± 0.04	-0.93	-0.49
Ω^-	-----	-2.79	-1.84

Table 3 The stable baryon magnetic moments both measured and predicted.

QUARK	MAGNETIC MOMENT (n.m.)	MASS (MeV/c)
u	1.852	338
d	-0.972	322
s	-0.614	509

Table 4 The quark magnetic moments used in the broken SU(6) column of Table 3. Also given are the corresponding quark masses under the assumption that $g=2$.

Prediction	Reference	Comments
-0.91	(19)	exact SU(6)
-1.09	(20)	simple broken SU(6)
-1.37	(21)	configuration mixing $u = -2d$
-1.00	(22)	configuration mixing
-1.21	(23)	configuration mixing
-0.92	(24)	symmetry breaking
-0.69	(25)	symmetry breaking
-0.64	(16)	π cloud contribution
-0.81 ± 0.14	(17)	flavor symmetry
-0.82	(18)	decouplet contribution
-0.83	(26)	symmetry breaking
-0.78	(27)	symmetry breaking

Table 5 A number of theoretical predictions for the Σ^- magnetic moment. The predictions are in nuclear magnetons.

1.2 EXPERIMENTAL BACKGROUND

Historically there have been 3 techniques used to measure magnetic moments;

- 1) Magnetic Resonance
- 2) Fine structure analysis
- 3) Polarization precession analysis

Magnetic resonance techniques make use of the fact that the spin vector of a particle precesses in an external homogeneous magnetic field with a frequency ω_0 dependent on the value of the magnetic moment and the field. If a varying magnetic field is also applied parallel or perpendicular to the homogeneous field with frequency ω_B , transitions between spin states will occur when the resonance condition ($\omega_0 = \omega_B$) is fulfilled. It is then simply a matter of measuring ω_B at resonance, which in principle can be done very precisely. Unfortunately, because the effect is small, the technique requires a large number of long-lived particles and the hyperons do not fulfill these requirements.

Before this experiment the Σ^- magnetic moment was measured by performing a fine structure analysis of sigma-hyperonic atoms. (28,29) Incident K^- beams produced Σ^- 's in targets via the reaction:



Some of these produced Σ^- 's stopped in the target and formed sigma-hyperonic atoms. These are atoms where one of the orbital electrons is replaced by a Σ^- . The interaction of the Σ^- magnetic moment with the nuclear coulomb field produces a fine structure splitting of the atomic energy levels. Subsequent transitions made by the atom as the Σ^- cascades through the orbital electronic shells emit photons whose energy corresponds to the energy level difference of the transition. A measurement of the energy of these photons predicts a value of the moment. In practice the effect is so small that the level splitting is not discernible, instead the levels appear broadened. A measure of this broadening is very difficult and various complicated atomic effects had to be correctly included which made the resulting analysis model dependent. Some of the models used, such as for electron screening, are quite accurate, but an independent measurement of the moment by a different technique would

be of great value.

The discovery of inclusive polarization coupled with the high lab energies available at Fermilab makes the third technique also viable. A source of high energy polarized Σ^- 's with a long (6.5 m) average flight paths allows conventional magnets to be used to precess the polarization vector many degrees. The only difficulty with this technique as related to a Σ^- moment measurement is the small value of the Σ^- asymmetry parameter α_{Σ^-} ($\alpha_{\Sigma^-} = -0.068 \pm 0.008$).⁽¹⁾ Since the signal this experiment measures is the product αP (where P is the value of the polarization) the fact that the average hyperon polarization is about 14% means that the expected signal size is only 1%. This difficulty is offset by the high inclusive production cross-section which allows a large sample of Σ^- 's to be obtained in a short time and the use of analysis techniques proven to be very effective in polarization measurements of this type.

The magnetic moment of the Σ^- was measured by precessing the polarization vector of a Σ^- sample through a known magnetic field. The spin of a CHARGED system precesses according to the equation,⁽³⁰⁾

$$\frac{d\vec{S}}{dt} = \vec{S} \times \vec{\Omega} \quad (6)$$

where :

$$\vec{\Omega} = \frac{q}{Mc\gamma} \left\{ \left[1 + \gamma \left(\frac{g}{2} - 1 \right) \right] \vec{B} + (1 - \gamma) \left(\frac{g}{2} - 1 \right) \frac{\vec{v}(\vec{v} \cdot \vec{B})}{v^2} + \gamma \left(\frac{g}{2} - 1 + \frac{1}{\gamma + 1} \right) \frac{\vec{E} \times \vec{v}}{c^2} \right\} \quad (7)$$

where all the fields are lab fields, $\gamma^2 = 1/(1 - \beta^2)$, $\beta = P/E$ and $E^2 = P^2 c^2 + M^2 c^4$. M is the mass of the Σ^- , and q is its charge (magnitude and sign). The Σ^- momenta were between 120 and 290 GeV for which $\beta = 1$ to better than 0.01%. In this experiment there is no electric field and the magnetic field was perpendicular to the Σ^- momentum vector. Hence $\vec{\Omega}$ becomes,

$$\vec{\Omega} = \frac{q}{Mc\gamma} \left[1 + \gamma \left(\frac{g}{2} - 1 \right) \right] \vec{B} \quad (8)$$

and,

$$\frac{d\hat{S}}{dt} = \frac{q}{Mc\gamma} \left[1 + \gamma \left(\frac{g}{2} - 1 \right) \right] \hat{S} \times \vec{B} \quad (9)$$

Integrating this over the path of the Σ^- in the magnetic field, the total angle through which the spin precesses is,

$$\theta_t = \frac{q}{Mc^2 \beta \gamma} \left[1 + \gamma \left(\frac{g}{2} - 1 \right) \right] \int \vec{B} d\vec{l} \quad (10)$$

Now θ_t is the total precessional angle as measured with respect to the coordinate system used to describe the fields. But the Σ^- momentum vector rotates with angular frequency,

$$\Omega_c = \frac{g}{Mc\gamma} \vec{P} \times \vec{B} \quad (11)$$

which is just the cyclotron frequency. The total angle of rotation due to this effect is,

$$\theta_c = \frac{g}{Mc^2\beta\gamma} \int \vec{B} d\vec{l} \quad (12)$$

and this effect must be subtracted from equation (10) to obtain the angle measured in this experiment. This is,

$$\theta_e = \frac{g}{Mc^2\beta} \left(\frac{g}{2} - 1\right) \int \vec{B} d\vec{l} \quad (13)$$

The quantity $g/2$ can be obtained from equation (13) and the definition of the Σ^- magnetic moment. This is:

$$\mu_{\Sigma^-} = \frac{g}{2} \frac{g}{Mc} \vec{S} = -\frac{g}{2} \frac{M_P}{M} \mu_N \quad (14)$$

after a little algebra we obtain the convenient form:

$$\theta_e = -\frac{2\mu_N}{\beta\hbar c} \left(\frac{\mu_{\Sigma^-}}{\mu_N} + \frac{M_P}{M}\right) \int \vec{B} d\vec{l} \quad (15)$$

One must remember that θ_e is measured with respect to the Σ^- momentum vector and hence its sign is important. Specifically θ_e is positive when the precession angle leads the Σ^- momentum vector and negative when it lags it.

CHAPTER 2

THE SPECTROMETER AND APPARATUS

2.1 THE BEAM DELIVERY SYSTEM

This experiment was performed in the M2 beam line of the Meson Laboratory at Fermilab. During the experiment the Fermilab synchrotron operated at 400 GeV with intensities of approximately 2×10^{13} protons per pulse. Each pulse was one second long with nominally 10 seconds between pulses.

For the following discussion all distances will be referenced relative to the Meson Lab. production target. The main ring beam was delivered to the meson target and there produced six secondary beams. The various secondary beams were fed to different experimental areas. A conventional beam transport system guided the diffractively scattered protons at 400 GeV down the M2 line to our area while two sets of collimators and two sets of quadrupoles shaped and focused the beam. The beam transport system was set up in two stages. The first stage produced a preliminary focus at 201 m where a segmented wire ion chamber (SWIC) was positioned for monitoring the beam position and shape on a spill-by-spill basis. The second stage produced a focus at 451 m where the hyperon production target was located. A vernier magnet located at 335 m could deflect the beam in the vertical plane and a set of three 3-meter long dipole bending magnets at 442 m restored the beam to the experimental target. In this way production angles up to 10 milliradians could be achieved. The intensity of the diffracted proton beam could be varied by the collimators and the bulk of the data-taking was done with 5×10^8 protons per pulse on the experimental target. A schematic of the beam delivery system is shown in Fig. 1.

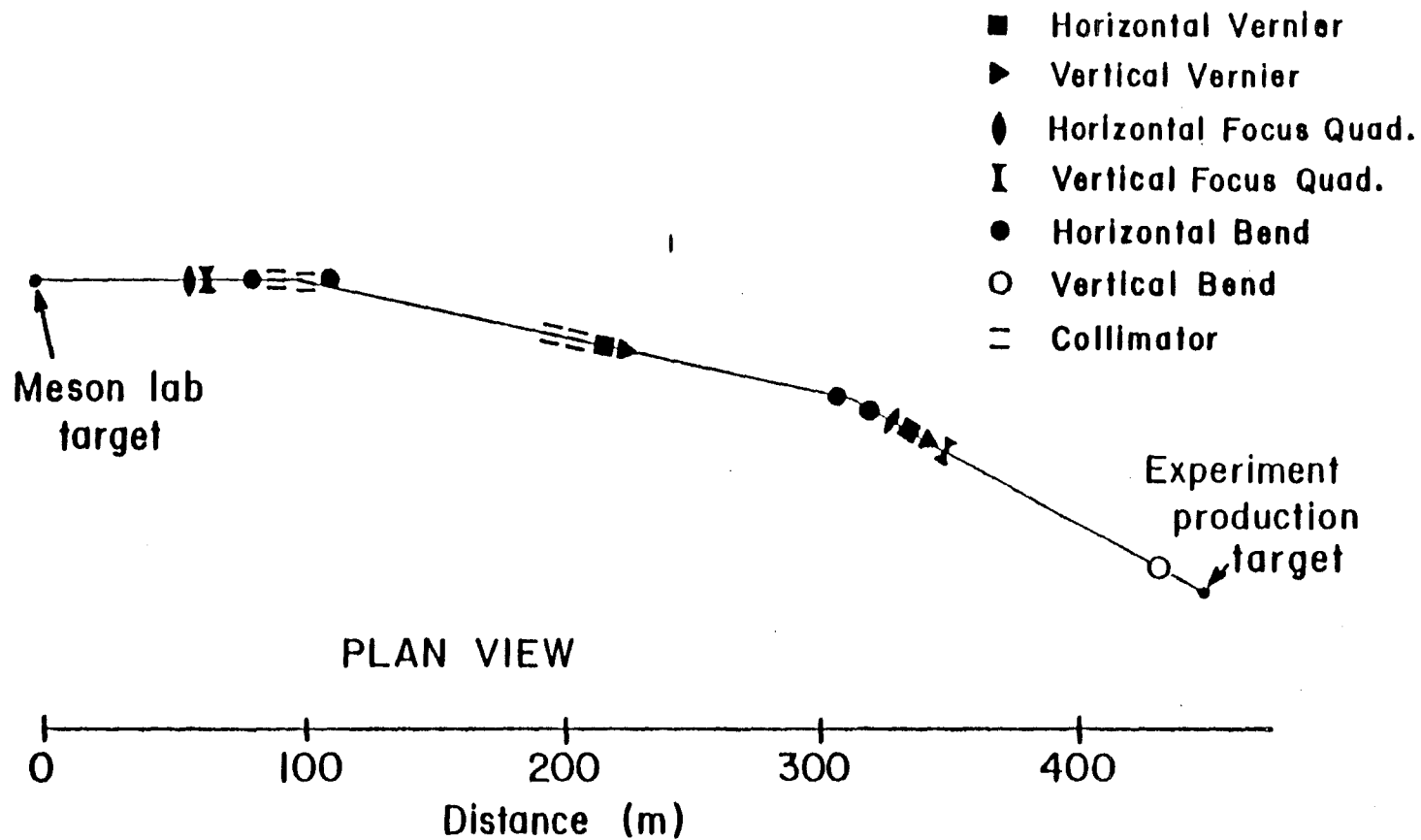


Fig. 1 The M2 proton beam transport system.

2.2 The APPARATUS

An plan view of the experimental area and the associated apparatus is shown in Fig. 2. A detailed discussion of the experimental apparatus will now be given.

2.2.1 THE TARGET AREA

Fig. 3 shows the layout of the target area during the experiment. The target was located at 451 m. It was a $1/2$ interaction length 6 mm diameter beryllium cylinder. Ninety cm upstream of the target was a SWIC which was used to monitor the position and shape of the focused beam at the target. Twenty cm further upstream was a regular ion chamber (IC) which measured beam intensity. Finally, 155 cm upstream of the target were placed 3 small scintillator counters used for preliminary beam focusing and for detection of the beam when, during some calibration runs, the intensity was too low for the SWIC to register. The scintillators were also used to calibrate the IC but were

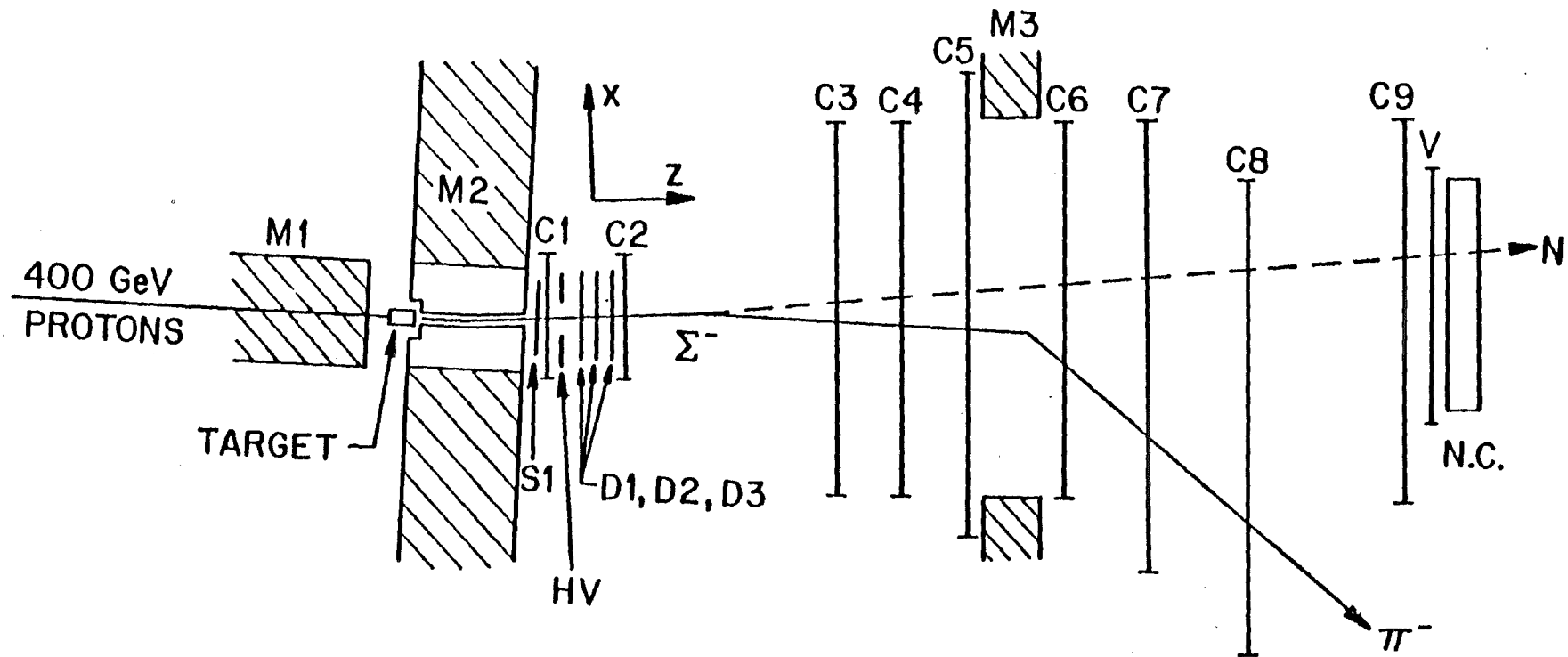


Fig. 2 A plan view of the M2 charged hyperon apparatus as configured to detect $\Sigma^- \rightarrow n \pi^-$. Magnet M1 was used to vary the angle in the vertical plane at which the proton beam struck the Σ^- production target. M2 served to define the Σ^- beam and precessed the Σ^- spin vector in the x-z plane. A conventional wire chamber spectrometer array, C1-C9, D1-D3 and M3 determined the Σ^- and π^- tracks. A calorimeter (NC) was used to signal the presence of a neutron.

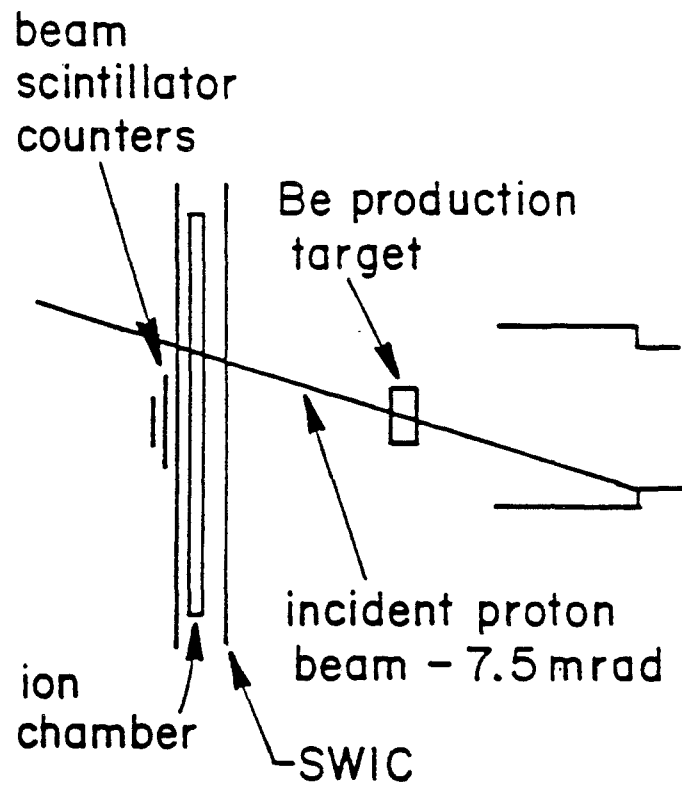


Fig. 3 The hyperon production target area and associated detectors.

removed in normal operation. All of these instruments were surveyed in from a point 15 meters upstream of the target.

2.2.2 THE CHARGED BEAM COLLIMATOR

Within the precessing magnet, M2, a collimator system was installed so that neutrals and positively charged particles were stopped short of the spectrometer. This beam channel was 5.3 m long with a total bend angle of 10 mr for a central ray. It had 2 circular limiting apertures which defined the charged beam, one at -250 cm with a 4 mm diameter hole, and the other at the exit of M2 with a 10 mm diameter hole. Fig. 4 shows the channel construction in detail. Both limiting apertures had tungsten inserts to enhance their beam stopping quality. This arrangement gave a 1.4 microsteradian angular acceptance. The relative momentum acceptance of the channel, as determined by a Monte Carlo simulation, is shown in Fig. 5 for an M2 field integral of 1.8 GeV. Note the extremely sharp cutoff at low momentum. This effect is crucial for some sources of background discussed later.

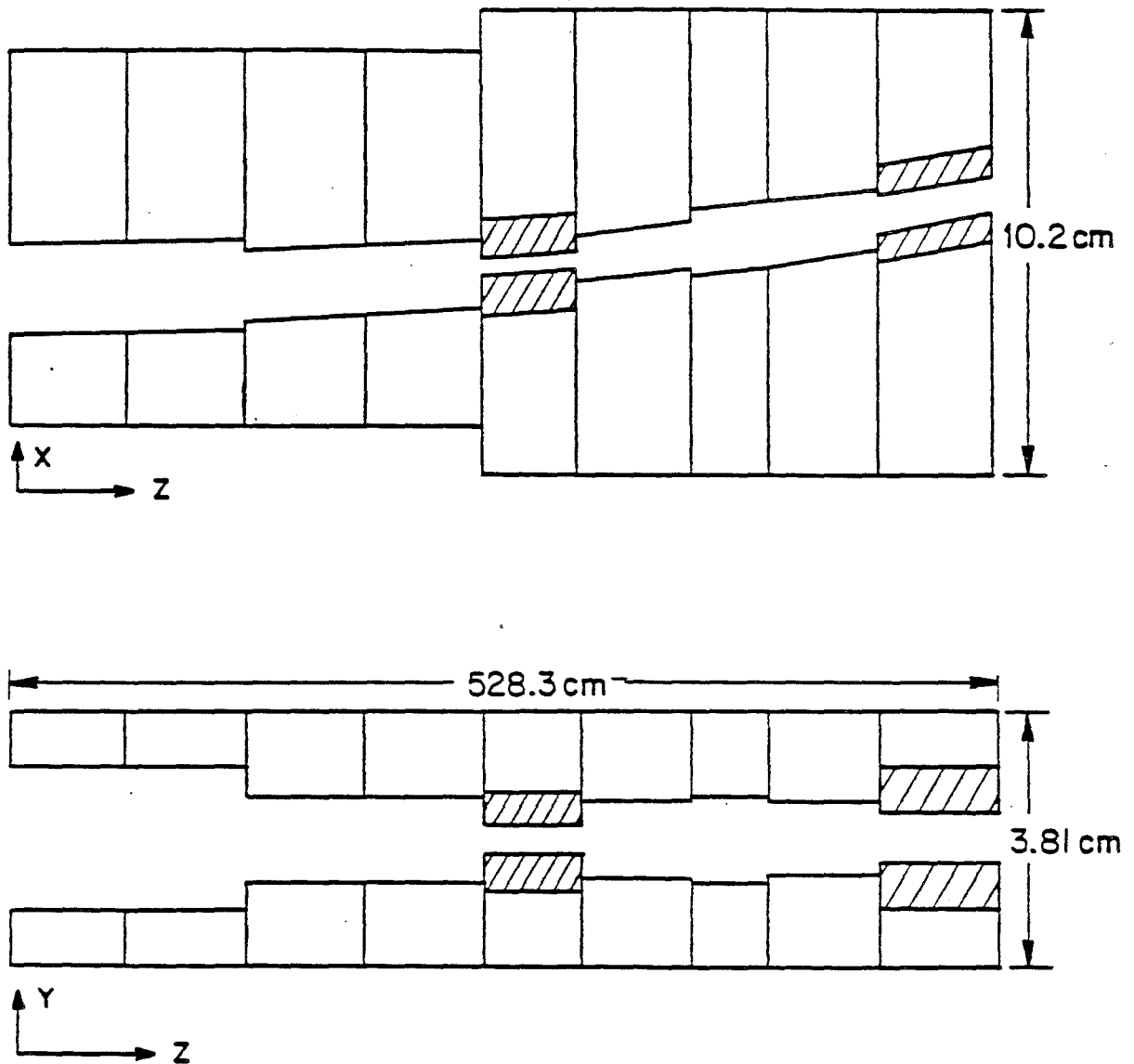


Fig. 4 The plan and elevation views of the M2 charged hyperon beam channel.

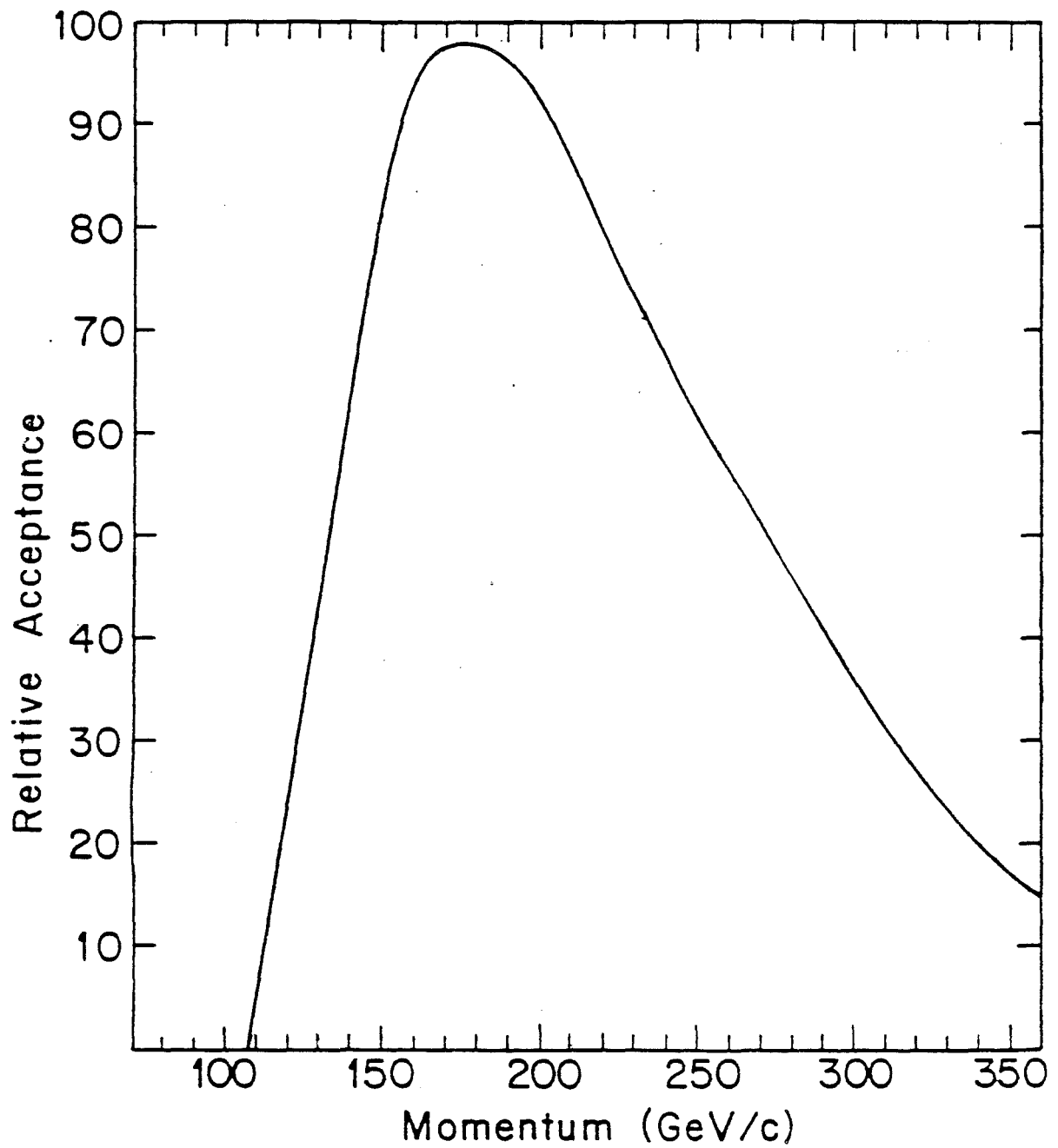


Fig. 5 The relative momentum acceptance of the M2 beam channel for $\int \vec{B} \cdot d\vec{l} = 1.8$ GeV/c.

2.2.3 THE SPECTROMETER

The downstream face of the hyperon beam channel defined the origin of the coordinate system used for the spectrometer and analysis. The direction of a central ray emanating from the beam channel defined the z axis, the y axis was vertical, and the x axis was in the direction $\hat{y} \times \hat{z}$. All quoted measurements will be relative to this coordinate system from now on.

The spectrometer was designed to optimize the acceptance of the $\Sigma^- \rightarrow n + \pi^-$ decay mode. It consisted of multiwire proportional chambers (MWPC), drift chambers (DC) and two analyzing magnets M2 and M3 (see Fig. 2).

The M2 magnet served three purposes, it swept away positively charged particles, it was used to determine the Σ^- momentum, and it produced the field that precessed the Σ^- spin vector. Its field integral was 5.94 ± 0.01 T-m and was monitored precisely with a proton-resonance probe imbedded in the collimator channel which measured a standard field against which the field integral was calibrated. Run-to-run fluctuations in the standard

field setting were at most 0.1%.

MWPC's C1 and C2 and the DC's D1, D2 and D3 were used to measure the Σ^- track before decay to determine its momentum and aid in finding the decay vertex. The momentum of the decay pion track was determined from hits in C3 to C8 before and after the analysing magnet M3. The neutron was detected in the iron-scintillator sandwich precalorimeter "NC".

The proportional chambers had 2 mm signal wire spacing and contained both horizontal and vertical wires for measuring the y and x coordinates respectively. Chamber 4 was rotated by 45 giving a set of "U" and "V" planes for ambiguity resolution. C5 had also 1 additional signal plane mounted at 45 degrees which had 2.828 mm wire spacing. A detailed description of the MWPC's can be found elsewhere. (31)

The gas used in the proportional chambers was a mixture of argon and freon bubbled through methylal at 0°C. The percentages of the various components were kept constant at 90% Ar, 0.1% Freon and 10% Methylal by volume. This mix has been found to provide reasonable gain at moderate

voltages, and makes the system relatively immune to electrostatic and electronic instabilities. A typical operating voltage was 2.8 kv. The efficiencies of the MWPC's were all in excess of 99% except for C1. The space charge buildup due to the high charged particle fluxes at the M2 exit aperture lowered its gain below the plateau region. Its efficiency was typically 95%.

The analysing magnet "M3" was a ferric superconductor with an aperture 20.3 cm vertically by 61 cm horizontally and 250 cm long. Its main function was to measure the decay π^- momentum. Its field integral was approximately 3.17 T-m and was determined precisely on a run-to-run basis in a manner described later.

The NC was a 5 layer iron-scintillator sandwich (see Fig. 6). The anode signals from the scintillators were attenuated by 20 db and fed to a Lecroy 2249 12 channel analog to digital converter (ADC) which was read and cleared for every event. The whole array was 3.7 interaction lengths long.

Finally, there were the various scintillation counters essential to this experiment. These are the S1, HV and V

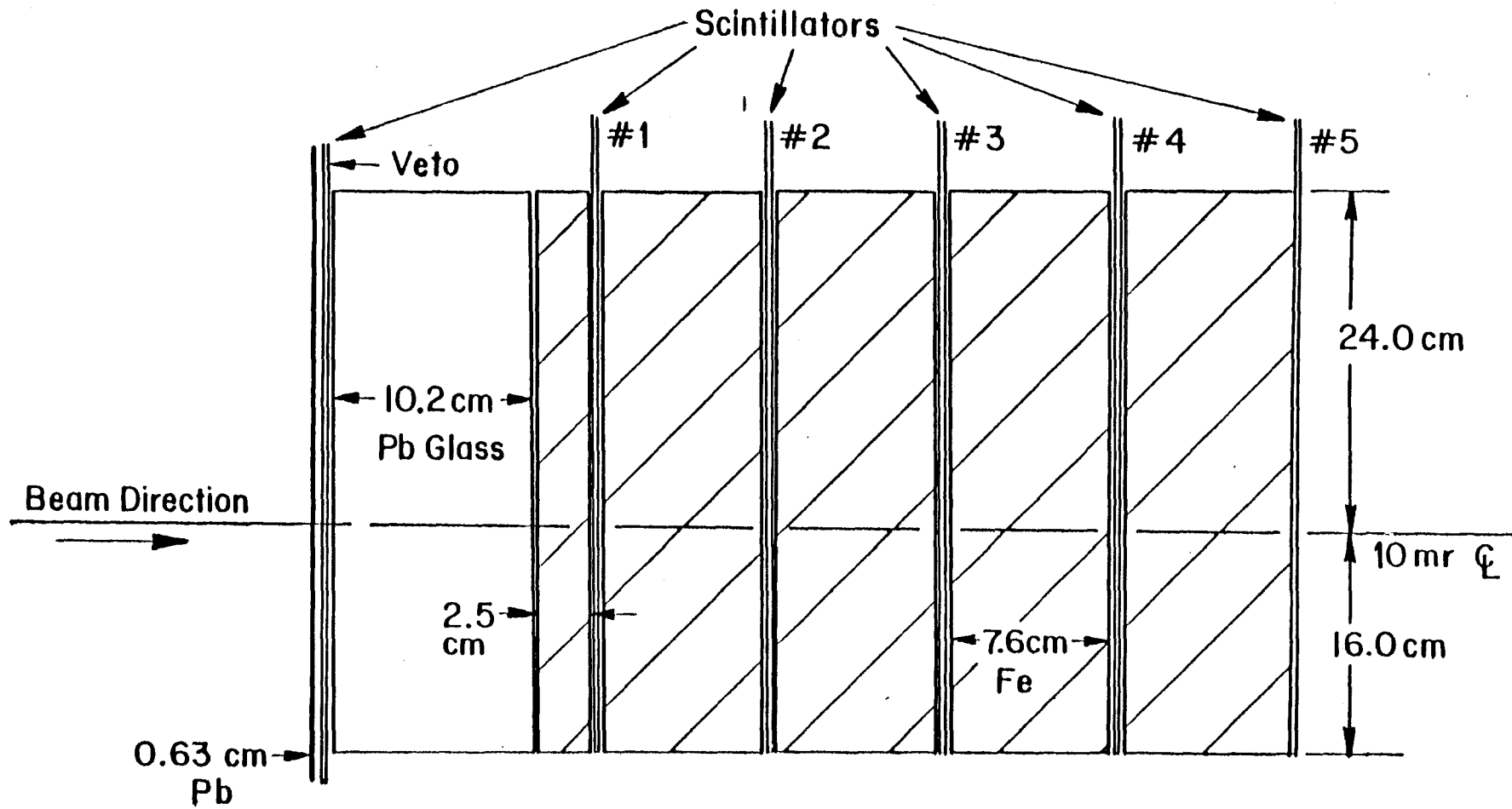


Fig. 6 The neutron precalorimeter with associated detectors.

counters also shown in Fig. 2. S1 served as the timing counter and assured that a charged particle coincided with the neutral in the NC. The "HV" stands for Halo-Veto, a scintillator designed to eliminate the background from the charged beam by defining an aperture through which all charged particles must pass. The veto "V" assured that a neutral triggered the NC. It also had a 1 radiation length piece of lead covering its upstream face so that stray gammas would convert and veto the event.

In the region between most of the chambers were placed helium filled polyethylene bags to reduce multiple scattering and interactions in air.

2.2.3.1 THE DRIFT CHAMBERS

The DC's were of conventional design and are described in detail elsewhere.⁽³²⁾ The DC's were extremely important chambers in the experiment because they measured the Σ^- track. It was imperative that the Σ^- track have as many points on it with as high a spatial resolution as possible to determine the decay vertex and Σ^- momentum. Beam

loading due to high charged particle fluxes on small DC areas limited their efficiency and resolution. Therefore careful attention was paid to the calibration and performance from run-to-run.

2.2.3.1.1 CALIBRATION

Each of the three DC's were calibrated cell by cell where possible. The procedure consisted of obtaining a large sample of straight track events and using the MWPC's to extrapolate each of these tracks to the cell being calibrated. (Beam π^- triggers were prescaled and latched for just this purpose. Typically about 10,000 usable Beam π^- 's were obtained per tape, giving a running calibration throughout the experiment). The tracks were binned according to where they intersected the cell being calibrated. A bin size of 0.5mm was selected. Histograms of time to digital converter counts (TDC) counts for each bin showed sharp peaks and the mean of each peak was found and plotted as a function of that coordinate. The resulting graphs looked typically like Fig. 7. The slope and intercept yield the desired calibration constants.

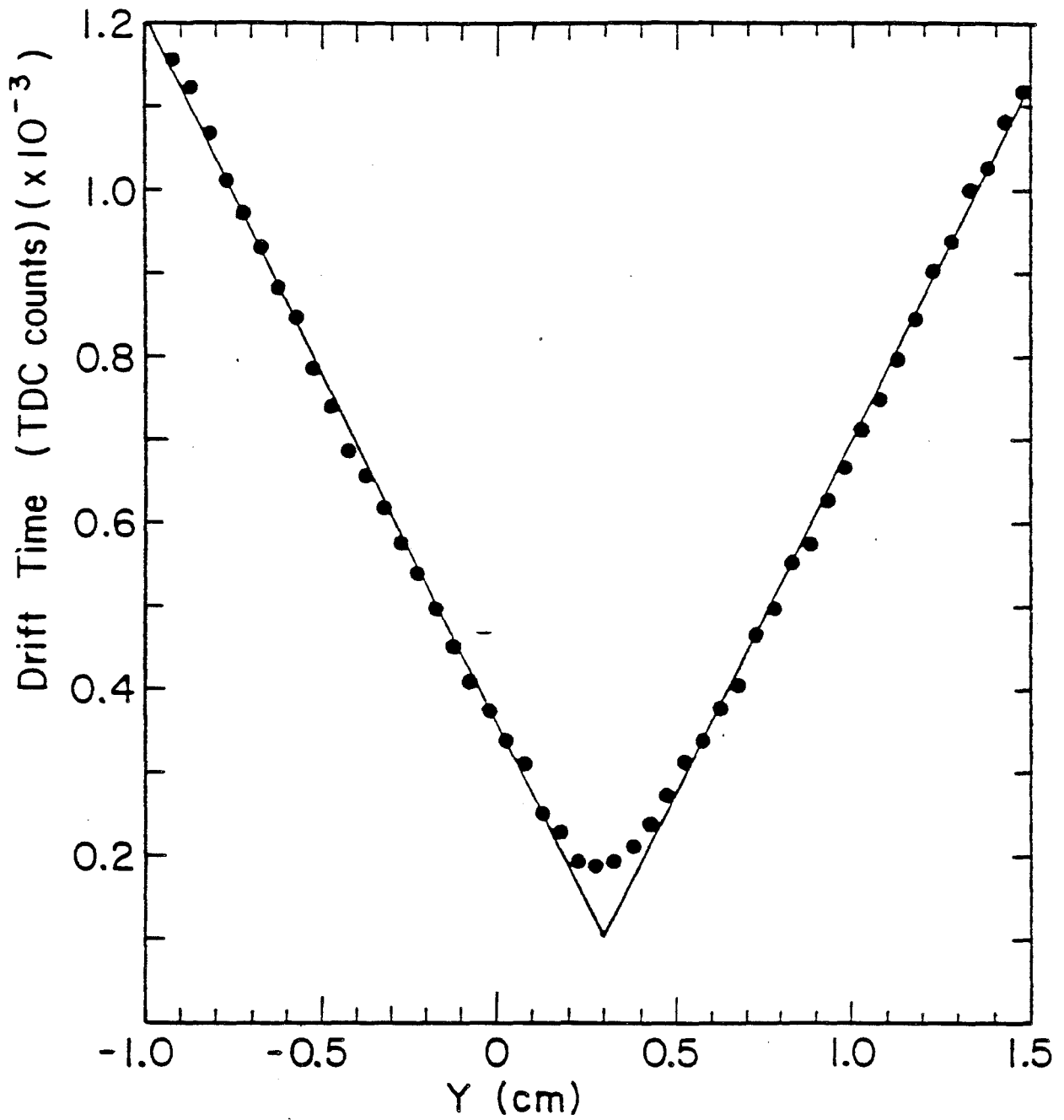


Fig. 7 A typical drift chamber calibration curve.

Though tedious, the procedure proved to give an accurate portrayal of each cell as long as enough straight tracks existed. One advantage to this method is that it does not require a uniform distribution of events across the cell face, a condition that was not satisfied in this experiment. For those cells which were outside the straight track cone, a slope was used that was the average of the slopes of the determined cells in that plane and the intercepts were determined from the known wire spacing. Residuals were then used for the final calibration. A typical drift velocity was 5 cm per microsecond.

2.2.3.1.2 PERFORMANCE

The DC's used an 80/20 mixture of argon/CO₂ which was guaranteed to .001% in the minor component. They typically ran at about +3000 volts. Various recalibrations throughout the experiment showed that the calibration constants did not change within errors. Run-to-run variations were negligible. The DC's were however the limiting factor in deciding the beam intensity

for running conditions. It proved necessary to keep the singles rate on proportional chamber C1 less than 200,000/pulse to achieve 80% DC efficiency. This efficiency was acceptable due to the large redundancy in DC planes. At 80% efficiency, the fact that each DC had 2 planes for each coordinate meant a better than 95% chance that an event would have hits in either DC 1 or 2. This was chosen as the minimum requirement for Σ^- track information.

The resolutions of the DC's were independent of the cell size. Three different cell sizes were used, 2, 3, and 6 cm. Their average resolutions and efficiencies integrated over the experiment are tabulated in Table 6.

DC PLANE	CELL SIZE (cm)	RESOLUTION (mm)	% EFFICIENCY
1x	2.04	0.22	81
1y	3.04	0.22	60
2x	2.04	0.27	83
2y	3.04	0.27	76
3x	2.04	0.24	84
3y	6.10	0.24	85

Table 6 The DC resolutions and efficiencies.

2.3 THE TRIGGER LOGIC

The existence of a neutral and a negatively charged particle downstream of M3 in coincidence with a charged particle emerging from M2 was an effective signature for the $\Sigma^- \rightarrow n + \pi^-$ decay. Fast logic signals from the MWPC chambers as well as signals from scintillators were used in the trigger.

First the signal from S1 was used as a time base. All other counters and chambers were timed into the logic relative to it. To assure that both the parent and at least one of the daughters were charged, a coincidence between S1 and C3 was required. Only half of C7 (in the negative x direction) was included in the trigger to require a negatively charged daughter. Finally, no charged particle in V and a signal from NC was used to trigger on the neutron while the HV was used to eliminate spurious charged background.

Written out in logical notation the Σ^- trigger was:

$$\text{trigger} = S1 \cdot \overline{HV} \cdot C3 \cdot C7R \cdot \overline{V} \cdot NC$$

Prescaled at a low level (1/512) were a sample of straight tracks (π 's produced from the target) with the signature:

$$S = S1 \cdot HV \cdot C3 \cdot V$$

which were used for various calibrations.

2.4 THE DATA ACQUISITION SYSTEM

The computer system used for data acquisition was a PDP 11/45 with a CAMAC interface. When the trigger was satisfied, an enable pulse from the fast electronics set latches in the MWPC's for those wires that were hit and started the clock in the TDC's. The latches stored the wire hit information for that event while the pulse from the hit in the DC's served as the stop pulse for the TDC clock. The chambers were then read out serially while the computer set a "busy" logic level so that no new data would be accepted while reading. The DC's and ADC's were read out after the MWPC's. This process took typically 1 msec. After all data was read the computer reset logic levels for the "ready" mode.

The beam spills were 1 second long and at the end of each spill, the computer read scalers that monitored rates and beam characteristics.

Data for each spill were written to memory until an event buffer was filled. Subsequent events were recorded in another of the twelve buffers and the filled buffer put into a queue for recording on disk. After data from a given buffer were recorded, the buffer was again available for input. At the end of each spill the data on disk was transferred to tape at 800 bpi, and events remaining in the computer memory were analysed and histograms generated for on-line diagnostics.

CHAPTER 3

DATA ANALYSIS I : EVENT RECONSTRUCTION

3.1 RECONSTRUCTION PROGRAM AND DATA SUMMARY TAPES

The primary purpose of the reconstruction program was to use the wire chamber information from each trigger to search for events of the $\Sigma^- \rightarrow n + \pi^-$ topology. These events were then subjected to various fits to improve the quality of the reconstruction and aid in rejecting background triggers. The reconstruction program was divided into five major sections:

- 1) Pattern Recognition - using chamber data to search for kinked tracks.
- 2) Monitoring Section - using the data to monitor calibration fluctuations and target position changes.
- 3) Geometric Fit - using wire hit information and vertex positions from the pattern recognition to determine the best spatial fit to the data.
- 4) Kinematic Fit - One-constraint fit to the kinematic variables on the assumption that the parent was a Σ^- which decayed to a neutron and a π^- .
- 5) Analysis Section - this section applied cuts to the data, determined the quality category of each event, wrote the events in certain categories to data summary tapes (DST) and filled histograms to look at various particle distributions.

Also written was a Monte Carlo (MC) program that was designed to determine the reconstruction program's

efficiency in detecting Σ^- decay and its ability to reject various sources of background. Its important features are outlined in Appendix 1.

MC analysis showed that the reconstruction program's efficiency was greater than 98% for Σ^- 's decaying after 600 cm, but fell sharply for earlier decays. See Fig. 8 for a graph of reconstruction efficiency versus decay vertex. The primary reason for this falloff was due to DC inefficiencies. For decays between 1300 and 1600 cm. only 2 chambers, C4 and C5 were able to determine the pion track in x after decay. After 1600 cm. only C5. This made the vertex resolution slightly poorer for later decays with a corresponding small loss in reconstruction efficiency. The track and vertex finding efficiencies were both found not to be functions of production angle, a feature which is important in bias cancellation discussed in section 4.2.

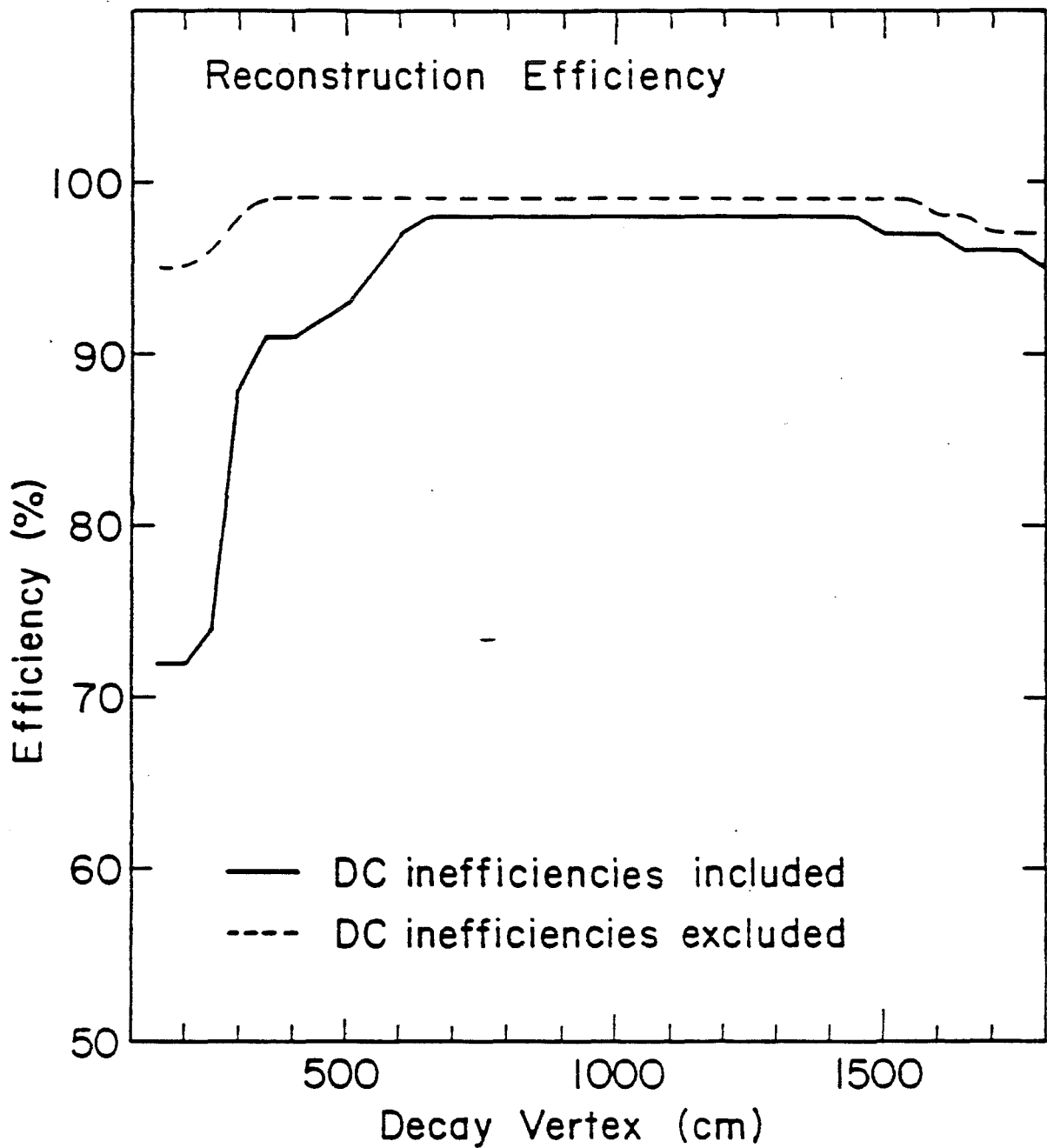


Fig. 8 Reconstruction efficiency as a function of decay vertex for perfect drift chamber efficiency and imperfect drift chamber efficiency. (note suppressed zero)

3.2 THE DATA SET

Data for this experiment were taken in 2 separate time periods. One period took place in December, 1979 and the other in January, 1980. Some changes in the apparatus took place between the two runs.

The December data run took a total of 22 data tapes separated into equal parts of +7.5 and -7.5 mr production angle. Each December data tape contained about 50,000 raw triggers, which were collected in about 1.5 hours. On the average 25,000 triggers were unreconstructable due to either very high multiplicities in the chambers, or insufficient hit information. Fifteen thousand were reconstructed as straight tracks and 10,000 as kinked tracks. The kink track was the single most important topological requirement. Of these 10,000 kinked tracks about 4,900 survived all software cuts for Σ^- quality. This gave a total of 108,377 Σ^- events split into 2 categories depending on the number of DC points used to determine the Σ^- track. These 2 categories were:

(1) at least 3 DC points on the Σ^- track per view

(2) 2 DC points on the Σ^- track per view

Category (1) was by far the largest with 89,730 events and category (2) had 18,647 events. Each of these categories were analysed separately to see if they contained any special problems or biases.

The January yield was much improved because running intensities were kept lower. Thirty data tapes were taken with 95,000 triggers per tape. Each tape took about 2 hours and contained about 50,000 unreconstructable triggers, 25,000 straight tracks and 20,000 kinked tracks. Finally of the 20,000 kinked tracks, 13,600 passed all software cuts. Thus 14.3% of the January triggers were reconstructable Σ^- 's compared to 9.8% in the December data. This gave a total of 407,852 Σ^- events in the categories described above.

It must be remembered that category (1) implies a vertex cut since it is impossible to have greater than 2 DC points on the Σ^- track unless it decayed downstream of DC 2. Hence category (2) does not necessarily imply

inferior quality, usually it means an early decay.

All pertinent information for kinked and straight tracks was written on DST's so that many runs could be combined for analysis. The full December data was written onto 2 DST's, one for each production angle. The January data was also written to 2 tapes separated into production angles. Each Σ^- event contained the 3 coordinates of the vertex point, Σ^- and π^- momentum components and various quality flags.

3.3 EVENT ANALYSIS

The decay $\Sigma^- \rightarrow n + \pi^-$ was considerably different from the decays of other hyperons studied in similar experiments done previously by this group. With only 3.7 interaction lengths, no precise energy information could be obtained from the NC. This introduces many difficulties in the analysis and calibration, specifically that all reconstruction and kinematical information had to come from the Σ^- and π^- tracks alone. This constitutes a one-constraint fit if the parent is assumed to be a Σ^- .

The π^- presented no problem outside of the M3 nonuniformity (see Appendix 2) and its momentum was measured to 1% - 2% precision.

However the Σ^- momentum could not be measured precisely. Three things were needed for its momentum measurement:

- 1) The production point (the target position)
- 2) The position and slope of the Σ^- track downstream of M2
- 3) The M2 field integral

Requirement (3) was well measured from preceding experiments and known in this experiment to better than 0.1%. Requirement (2) had to be calculated separately for the 2 Σ^- categories. For category (1) a point on the Σ^- track was known to about 250 microns on the average, while its slope was known to better than 100 microradians. This contributed an expected average fractional error of less than 2% in the Σ^- momentum. For category (2) a

point on the Σ^- track was known to about 400 microns and the slope to about 200 microradians. This implies an average contribution of about 3% to the fractional error in the Σ^- momentum. Requirement (1) was a spectrometer-independent variable. It was essentially the width of the target. As stated earlier a 6 mm diameter Be target was used. Since the average bend angle was 10 mr with the bend center of M2 270 cm away from the target this gave an expected average fractional error in the momentum determination of 6.2%. Hence requirement (1) was the single most important cause of uncertainty.

The target position and the M3 field integral had to be determined from the data. This was done in the following manner.

The straight track triggers for each run were used to determine the variation of the target and defining collimator positions as a function of M3 field integral. A field integral was then chosen that gave the same value for the mean of the Σ^- mass plot as the external MC. The target and defining collimator positions corresponding to this value of the M3 field integral were then used in the reconstruction program. This method proved to be very

convenient and consistent with the expected target position and M3 field integral as determined by previous experiments. It was used for all the data.

3.4 EVENT SELECTION

The compacted tapes described in section 3.2 were then processed by a program which made several cuts to the data. Fig. 9 shows the geometric χ^2 distribution for a kink track fit. The final cut was made at 55. A similar cut for MC events showed that less than 1.4% of the Σ^- events were lost due to this cut, and that π^- decay was the principal reason for large geometric χ^2 's.

Inspection of the M2 channel momentum acceptance curve (Fig. 5), clearly shows that momentum below 105 GeV have zero acceptance. So any Σ^- reconstructed with momentum less than 105 GeV are either produced or scattered by the collimator. These were easily cut by requiring the Σ^- to have greater than 120 GeV momentum. It was found from external MC data that straight tracks are sometimes reconstructed as kinked tracks but that the corresponding

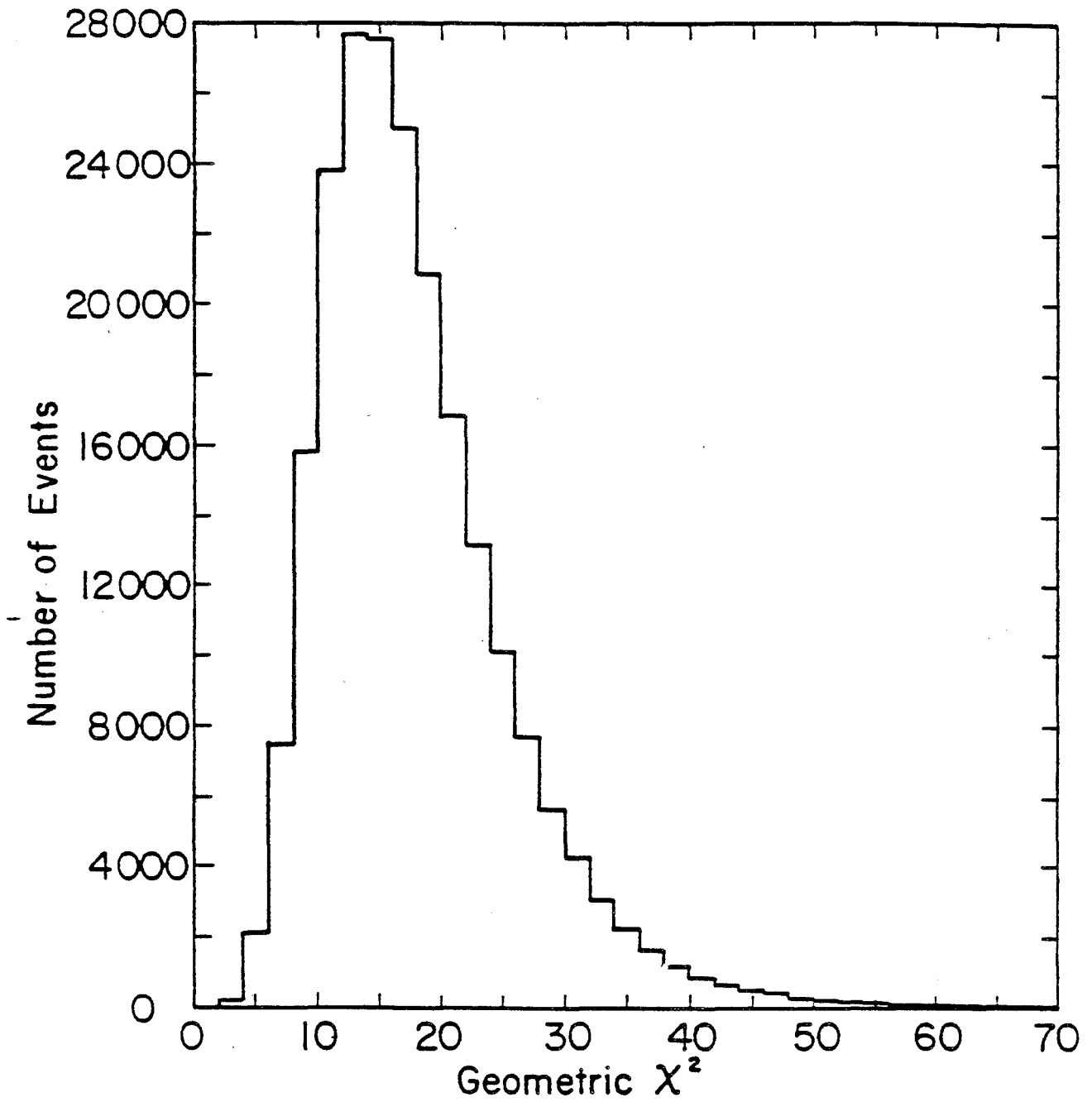


Fig. 9 The geometric χ^2 distribution for events that satisfy all other cuts described in the text.

" Σ^- " momenta then have high values, usually above 300 Gev. So a Σ^- momentum cut at 290 was also used. The effect of these two momentum cuts on the Σ^- momentum spectrum can be seen in Fig. 10. Over 98% of the reconstructed Σ^- 's fall into the accepted range.

A Σ^- momentum of 290 GeV implies a maximum π^- momentum of about 93.5 GeV. Therefore a 95 GeV π^- momentum cut was included. This cut assured that π^- 's produced at the target could not be misidentified as Σ^- 's because the momentum acceptance of the M2 channel precluded momenta less than 105 GeV. Again, inspection of the daughter π^- momentum spectrum (Fig. 11) shows this cut to be very soft against the true Σ^- events.

External MC analysis on straight tracks produces a "decay vertex" distribution shown in Fig. 12. About 95.0% of the "vertices" found by the reconstruction program were either less than 120 cm or greater than 1850 cm in z. Hence 2 vertex cuts were implemented to eliminate this possible source of background. One at 170 cm and the other at 1800 cm in z. These together immediately eliminated 96.0% of any straight track contamination. These cuts also assured that the Σ^- events contained

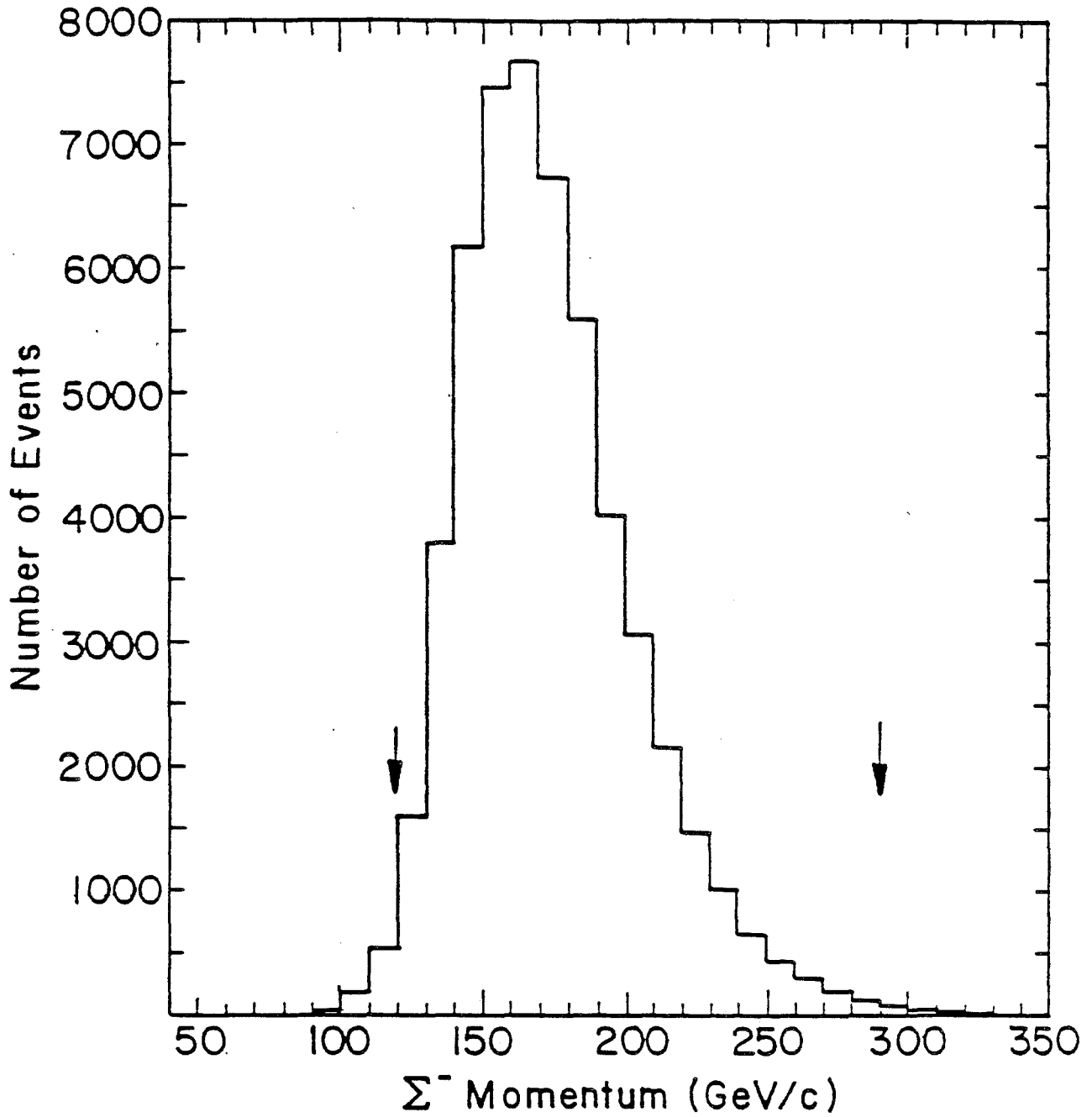


Fig. 10 The Σ^- momentum distribution with all cuts except the Σ^- momentum cut (indicated by arrows).

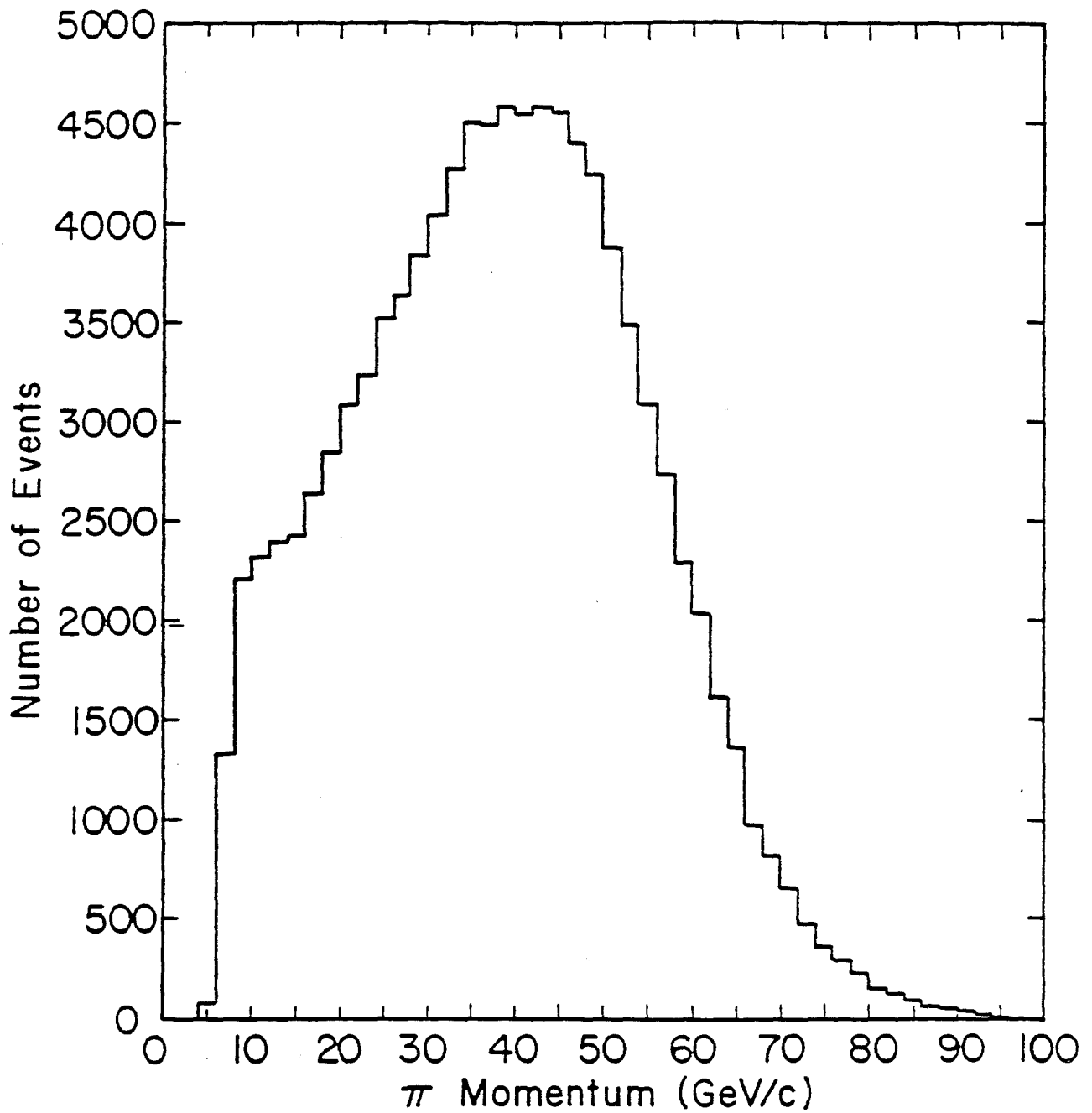


Fig. 11 The momentum distribution of π^- 's from $\Sigma^- \rightarrow n \pi^-$. All cuts have been made except the π^- momentum cut at 95 GeV/c.

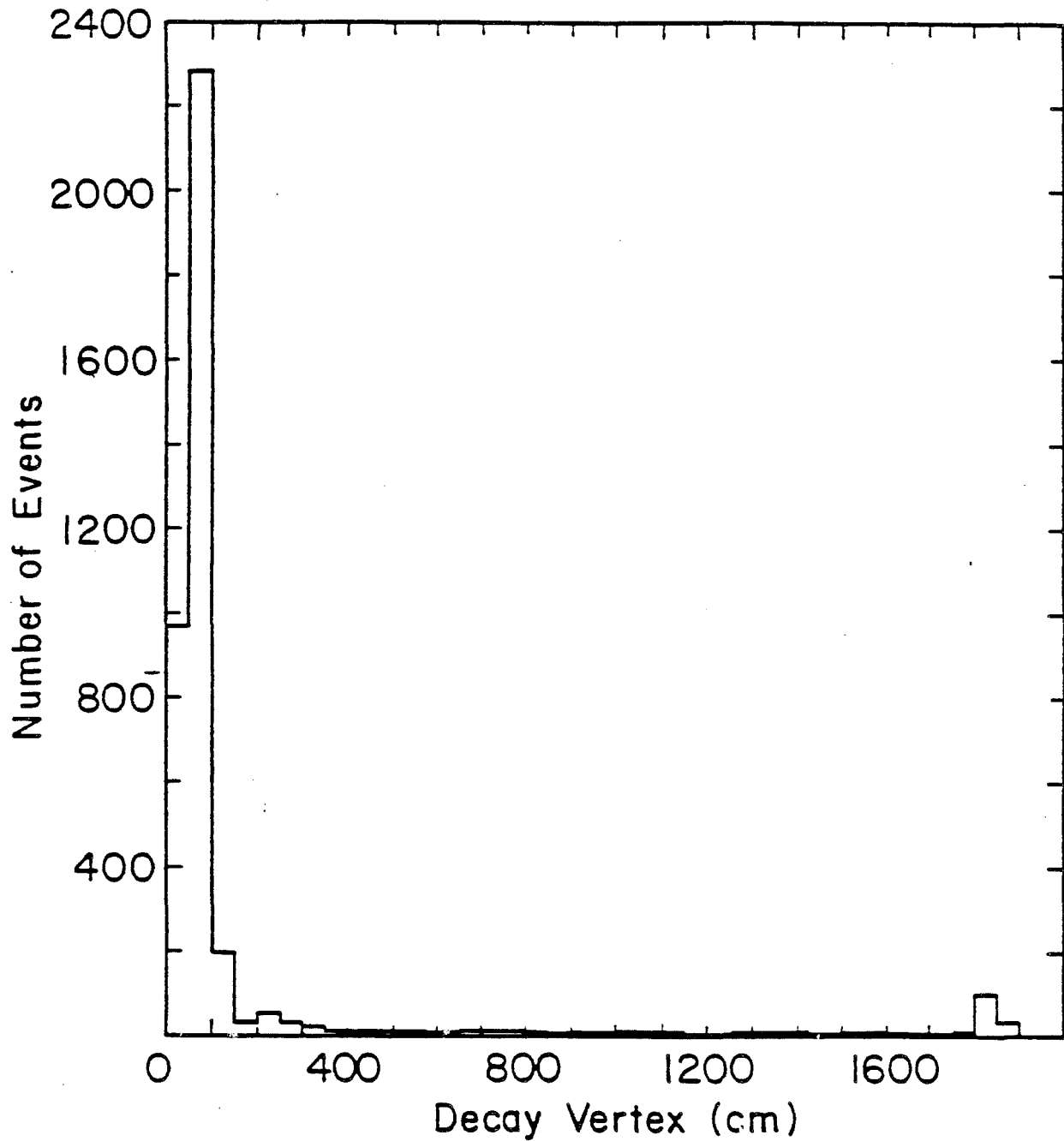


Fig. 12 The "decay vertex" distribution for straight tracks as determined from the Monte Carlo. For most straight track events the reconstruction program cannot form a "kink" with reasonable χ^2 anywhere except at the ends of the region covered by the wire chambers.

enough information on both tracks to assure confidence in the fits. Fig. 13 shows the resulting decay vertex distributions for Σ^- events in the final sample.

The data that passed the above cuts were subjected to a full kinematic fit which adjusted the momenta for each event subject to the constraint that the Σ^- mass was equal to the known value of 1.19735 Gev. If the increase to the total χ^2 due to this fit exceeded 7.5 the event was discarded (see Fig. 14). The number 7.5 was chosen after careful external MC analysis designed to simulate the spectrometer.

Finally, to eliminate Σ^- 's produced from the various counters in the target region that would still pass the kinematic constraints, a cut on the angle between the Σ^- momentum and the xz plane (θ_y) was made. This cut is explained in more detail in the next section.

The purity of the Σ^- sample produced by the above mentioned cuts can be seen from the shape of the Σ^- mass distribution (Fig. 15). A skewness to the shape or a tail on either or both sides would indicate a possible contaminant. None is seen in Fig. 15.

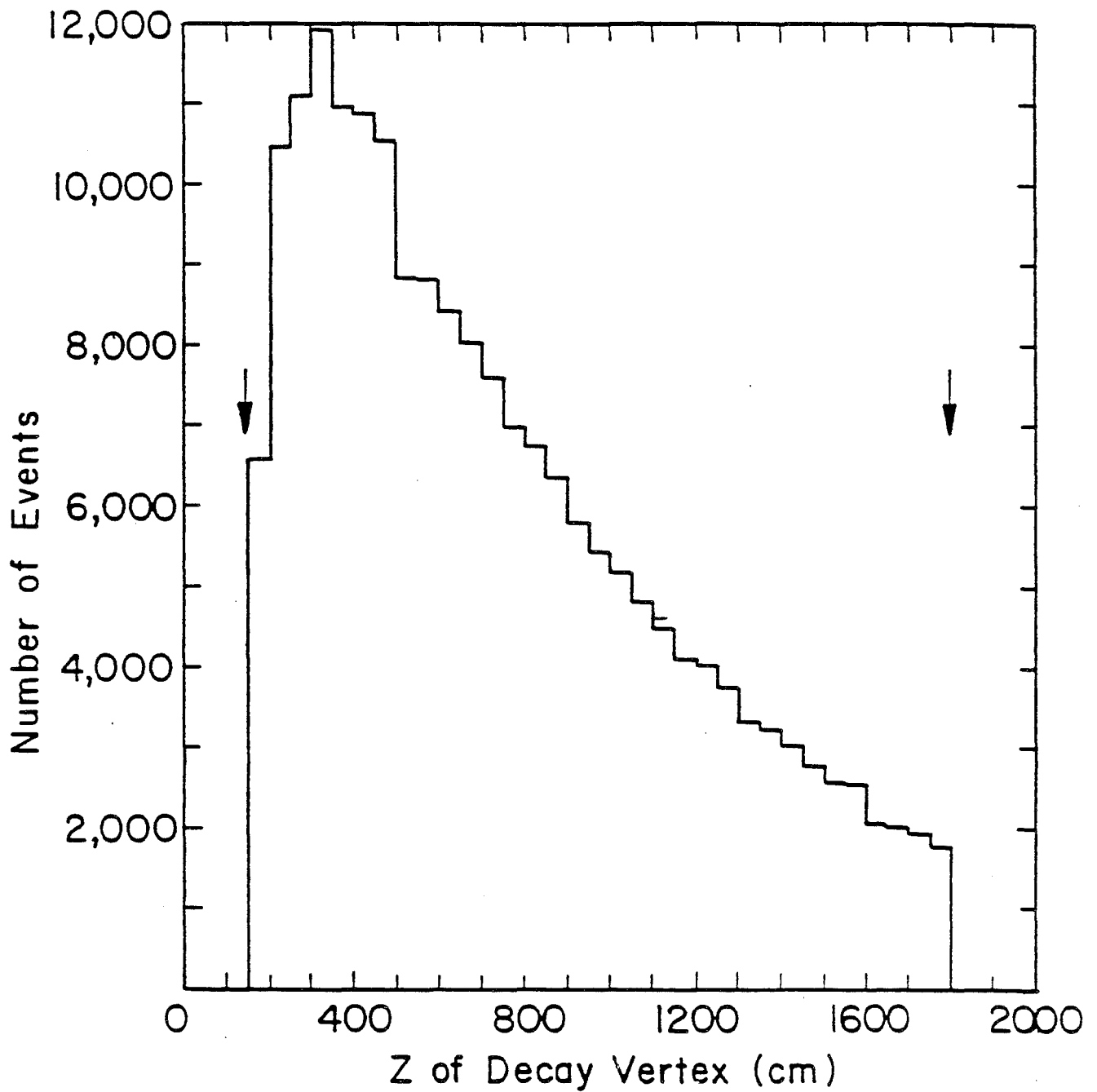


Fig. 13 The distribution of decay vertices for $\Sigma^- \rightarrow n\pi^-$ for events in which all cuts have been applied. The z cuts are shown by arrows. These eliminate straight track background. Compare with Fig. 12.

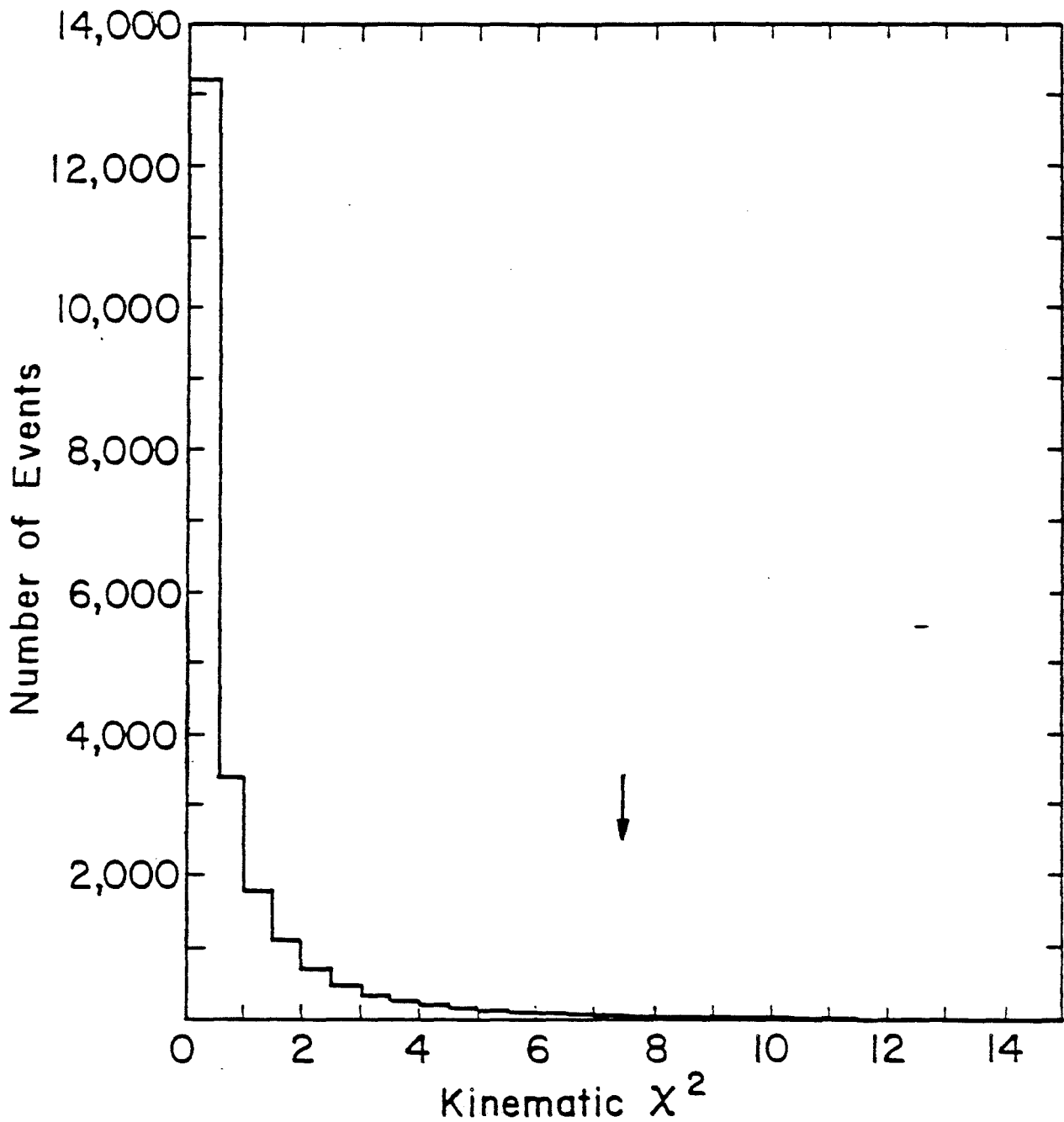


Fig. 14 The distribution of kinematic χ^2 (1-C fit) for events which satisfy all other cuts described in the text. A cut at 7.5 (arrow) was chosen for the final sample and eliminated 4.6% of the events in this distribution.

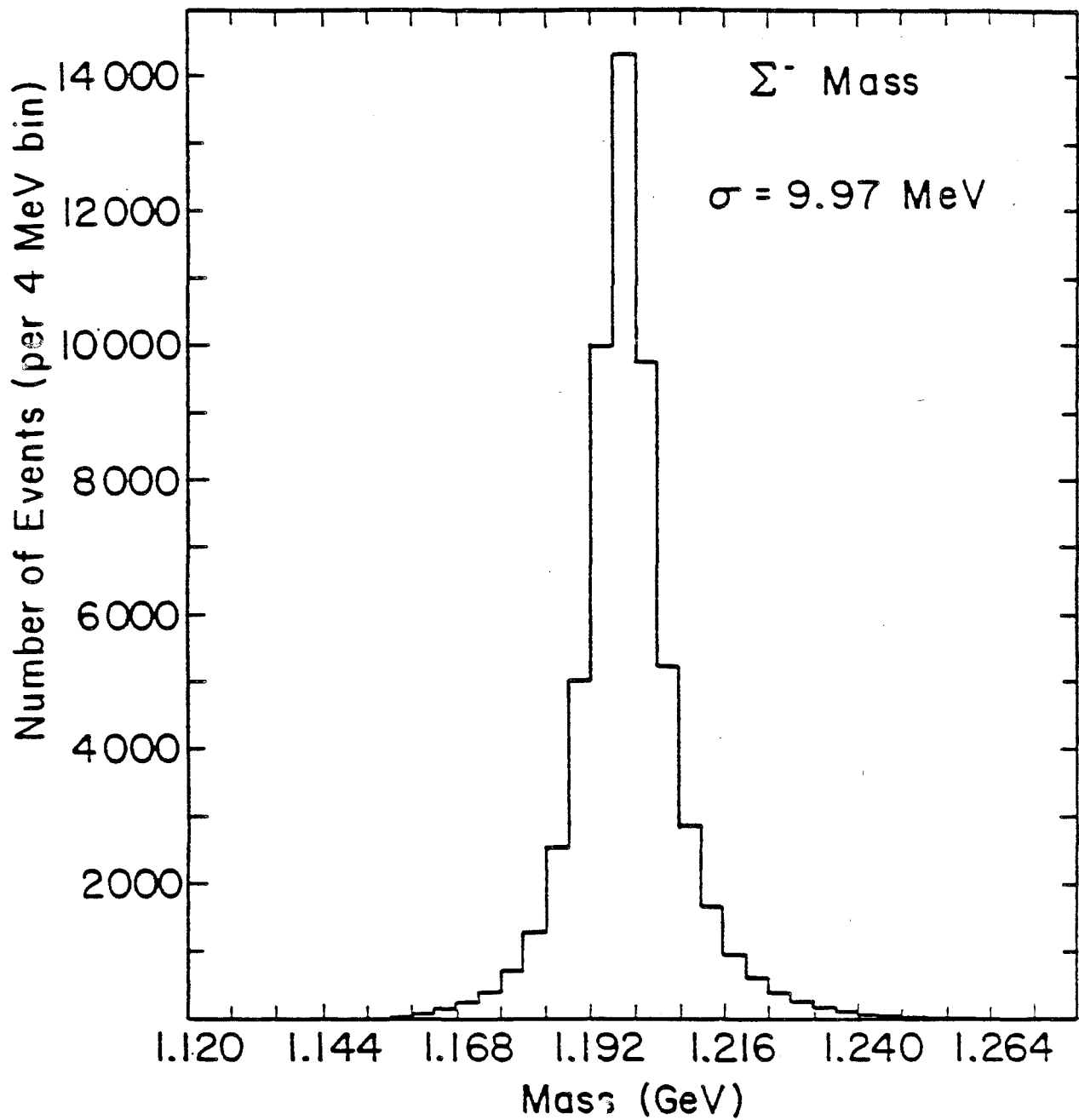


Fig. 15 The Σ^- invariant mass distribution obtained from the measured values of \vec{p}_Σ and \vec{p}_π :

$$M_\Sigma^2 = ((p_\pi^2 + m_\pi^2)^{1/2} + ((\vec{p}_\Sigma - \vec{p}_\pi)^2 + m_n^2)^{1/2})^2 - p_\Sigma^2.$$

Only those events that satisfied all cuts are shown.

Other cuts were considered, a $\Sigma^- - \pi^-$ opening angle cut, harder vertex cuts and cuts on the pulse height shape of the NC to eliminate possible sources of background but these proved unnecessary, as will be explained in the next section.

3.5 BACKGROUNDS

As stated earlier a number of tapes were written with the target not in the beam so that some measure of background sources not associated with the target could be obtained. Analysis of the target out tapes gave a background rate of 2.562×10^{-10} "Good Events" per proton on target (GE/p), while the average data tape yielded 5.117×10^{-8} GE/p. This gave an expected "target out" background of 0.50%. Calculations showed that approximately 65% of this background was due to Σ^- 's produced via beam protons interacting with air molecules in the target region, which are completely acceptable. The rest were Σ^- 's produced in the collimator or produced from interactions with the counters upstream of the target (the SWIC or the IC) which happen to fill the kinematic

requirements. If we define P_{xz} as the Σ^- momentum in the xz plane, then a plot of the angle $\theta_y = \tan^{-1}(P_y/P_{xz})$ for the 2 production angles would yield secondary peaks at ± 2 mr about the central peak if production in the upstream counters were appreciable. Fig. 16 shows clearly that such production is not large and was estimated to be less than 0.4% from the figure. To eliminate this source, both production angles were cut in θ_y by 2.7σ about their respective central peak. This cut about 1.5% from the final sample and changed the moment and polarization by less than 0.1σ but markedly improved the χ^2 for comparisons between real and IMC distributions. Therefore it was included in the final sample.

Sources of background would also include contamination from topologically similar decays. For example the 2 decays,

$$K^- \rightarrow \pi^- + \pi^0, \text{ and}$$

$$\Xi^- \rightarrow \Lambda^0 + \pi^- \quad \text{with} \quad \Lambda^0 \rightarrow n + \pi^0$$

could satisfy the trigger requirements outlined in section 2.5, and the spectrometer has good acceptance for both decays (Fig. 17). The lack of available production

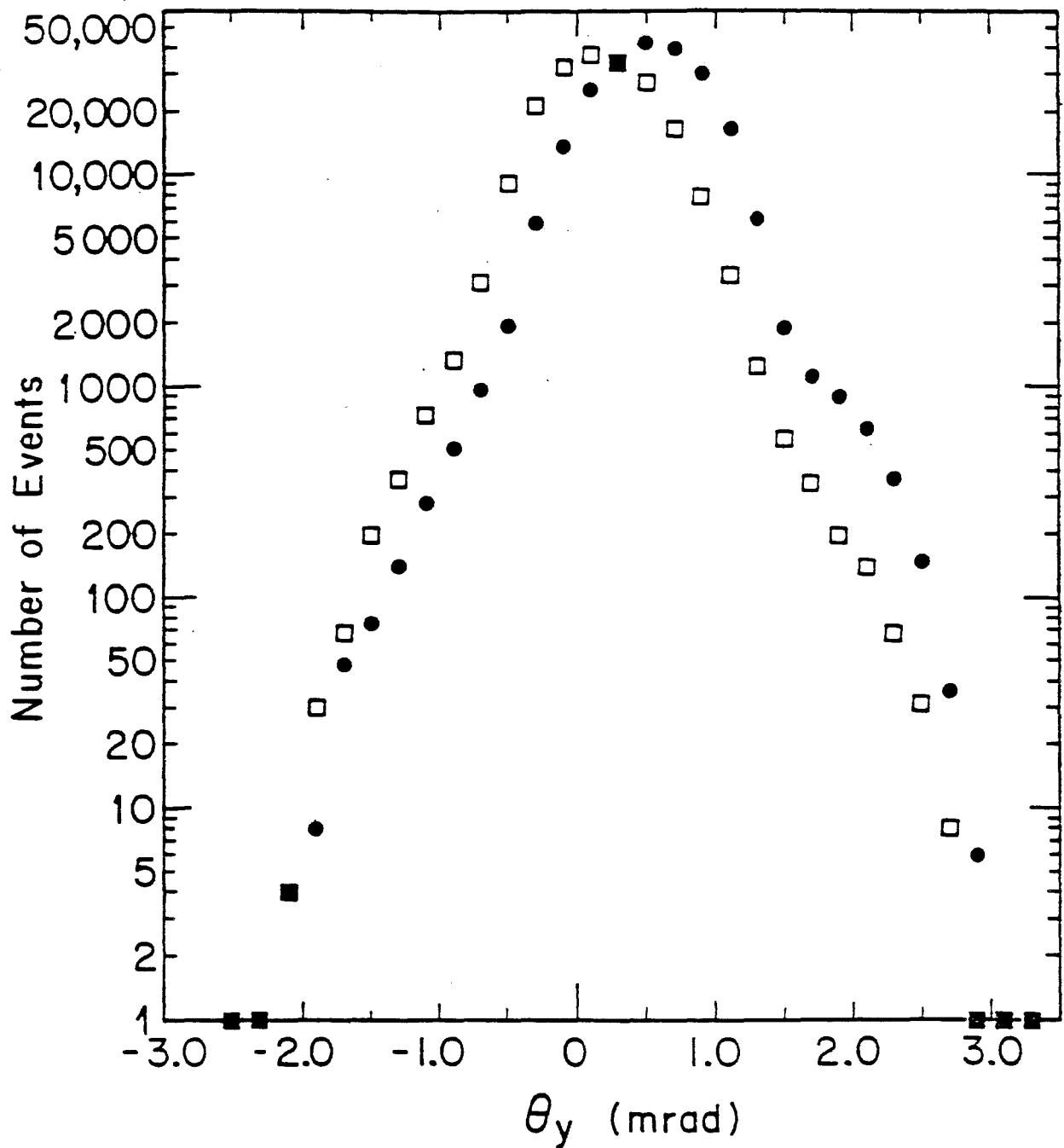


Fig. 16 The angle θ_y between the Σ^- momentum and the xz plane for events that satisfy all Σ^- cuts.

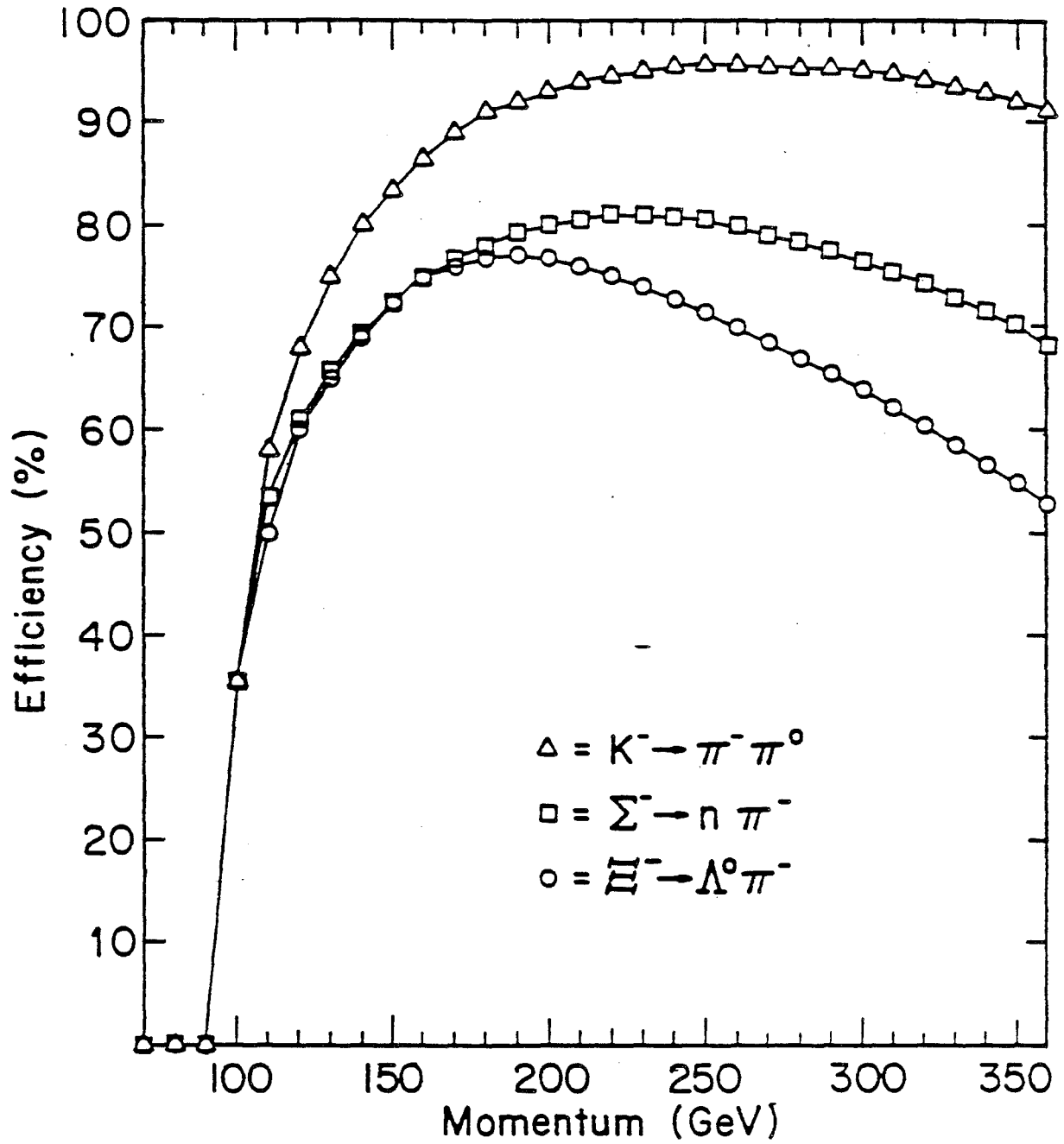


Fig. 17 The spectrometer acceptance curves for the decays, $\Sigma^- \rightarrow n \pi^-$, $\Xi^- \rightarrow \Lambda^0 \pi^-$ and $K^- \rightarrow \pi^- \pi^0$.

cross-section data at our kinematic region does not allow an explicit calculation of the expected relative background percentages for these decays. However they can be determined well from the data itself.

Figure 18 is a missing mass distribution of all kinked tracks in the raw data, fit to a cascade hypothesis. For comparison, the figure includes a sample of kinked tracks that satisfy all Σ^- identification cuts fitted to the same hypothesis. The peak represents a missing mass consistent with the Λ^0 mass. Fitting the raw event mass plot with a smooth curve and a gaussian function and then eliminating the events under the curve gives a good estimate of the number of Ξ^- 's in the sample. This procedure yielded 10,138 Ξ^- events in the full January sample which contained 407,852 Σ^- events, or 2.49% contamination. We may now use MC results on Ξ^- rejection to determine the percentage of Ξ^- 's remaining after the cuts mentioned in section 3.4 are implemented. The Ξ^- rejection was determined to be 90% so the relative Ξ^- background in the final sample is expected to be 0.25%.

The long lifetime of the K^- coupled with its large Lorentz γ -factor means that we expect only 1-2% to decay.

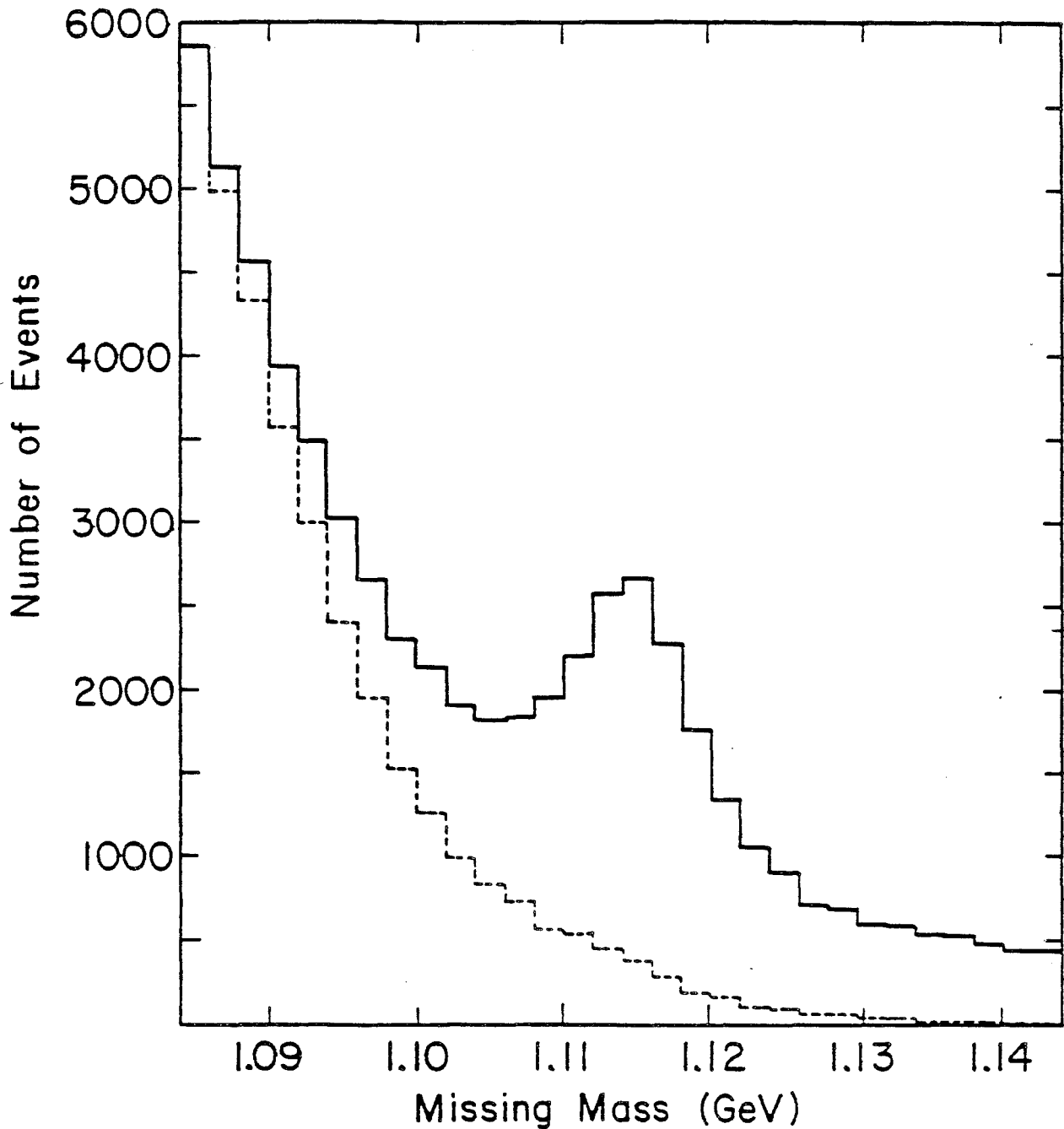


Fig. 18 A missing mass distribution for the hypothesis $\Xi^- \rightarrow \Lambda^0 \pi^-$, before and after cuts. The $\Sigma^- \rightarrow n \pi^-$ events fall into a very large peak off scale to the left. The kinematic χ^2 cut had the most effect on Ξ^- rejection.

in the fiducial region. For the Σ^- 's this percentage is close to 40.0% at 180 GeV. Only the $K^- \rightarrow \pi^- + \pi^0$ decay mode can fake the trigger and only if the gamma that is to trigger the NC does not convert in the lead in front of the veto. The branching fraction for this decay mode is 21%. These factors combine to make the expected K^- contamination in the raw event sample extremely small. Absolutely no π^0 peak was seen when raw kinked tracks were fitted to a $K^- \rightarrow \pi^- + \pi^0$ hypothesis (Fig. 19). Also shown for comparison is the peak a 0.5% contamination of K^- 's would make. This represents about the limit of the sensitivity of the graph and would be a 3 standard deviation effect. Finally only 10% pass the kinematical requirements, leaving an expected K^- contamination in the final sample of order 0.05%. So it is clear that K^- background will not be a problem in the data.

Another possible contaminant is π^- straight tracks with an accidental neutral. An external MC was run which produced straight tracks originating from the M2 exit with a flat momentum spectrum between 10 and 90 GeV and an assumed accidental neutral that triggered the NC. These events were then processed by the reconstruction program to determine how many were misidentified as Σ^- 's. As

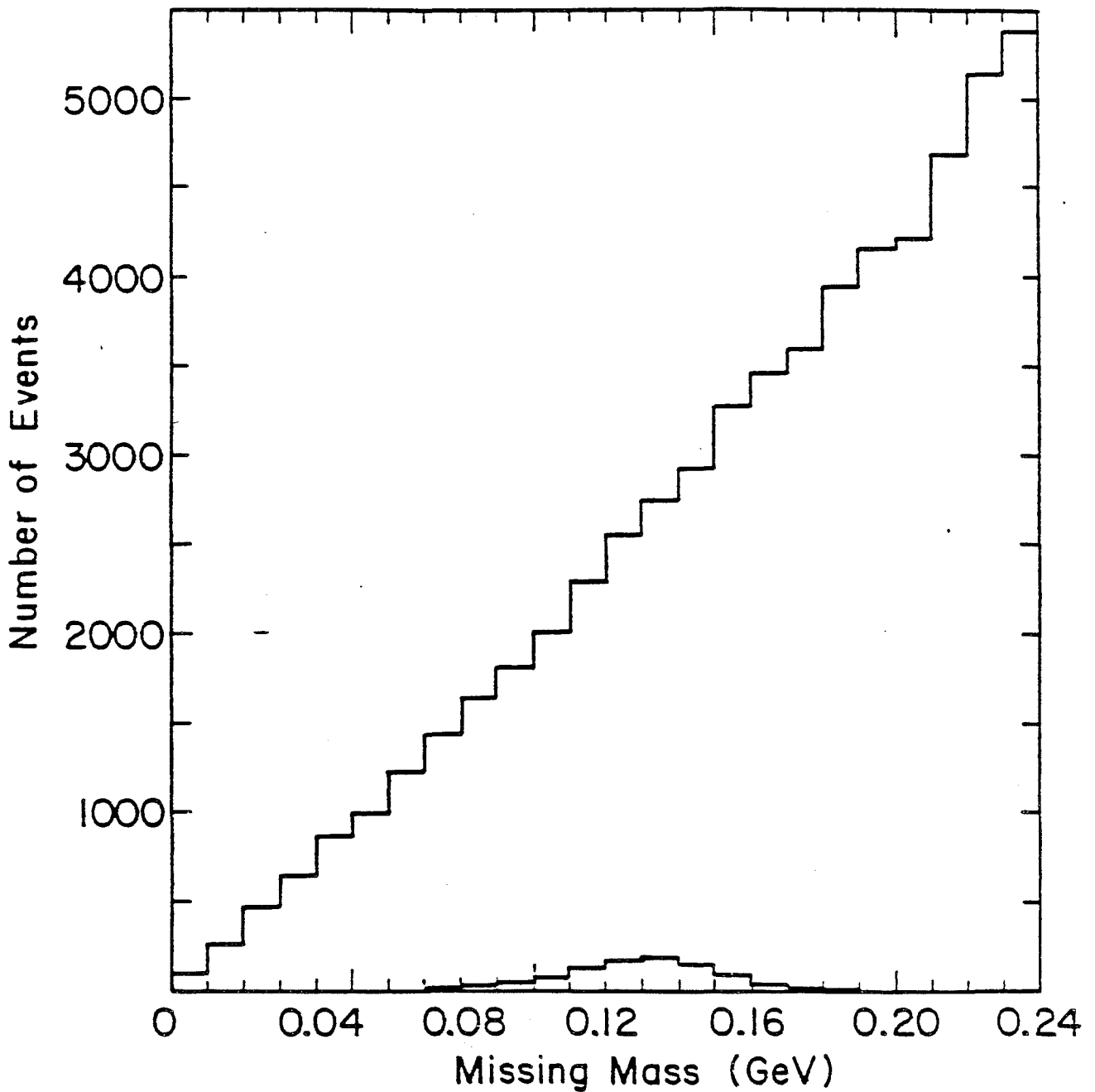


Fig. 19 A missing mass distribution for the hypothesis $K^- \rightarrow \pi^- \pi^0$ applied to the real data before cuts. Most of the events are off scale to the right. Also shown is a Monte Carlo calculation for simulated $K^- \rightarrow \pi^- \pi^0$ events normalized to 0.5% of the real data.

stated in the preceding section 96.0% were cut by vertex requirements and other cuts eliminated another 2%. Thus about 2.0% of these events were identified as Σ^- 's and all of these events had decay opening angles less than 1 mr. It is expected that the data have a much smaller straight track contamination than 2.0% due to the extra neutral triggering constraint, and inspection of Fig. 20 which is a decay opening angle comparison plot between real and MC data confirms this. There is no evidence of straight track contamination. However the data were processed with a 1 mr decay opening angle cut to observe its effect on the moment and polarization. The moment and polarization changed by less than 0.2 standard deviations, indicating that the effect of any straight track background was negligible. This cut was not made in the final calculation.

Fig. 21 is a histogram of the sum of the pulse heights in NC counters 3, 4 and 5. Pedestals have not been subtracted. NC counters 1 and 2 have been deliberately omitted so that gammas would not contribute to the sum. About 5.2% of the sample have pulse heights less than 200 counts which correspond to an energy deposition of less than 5 GeV. While this effect is expected since the NC is

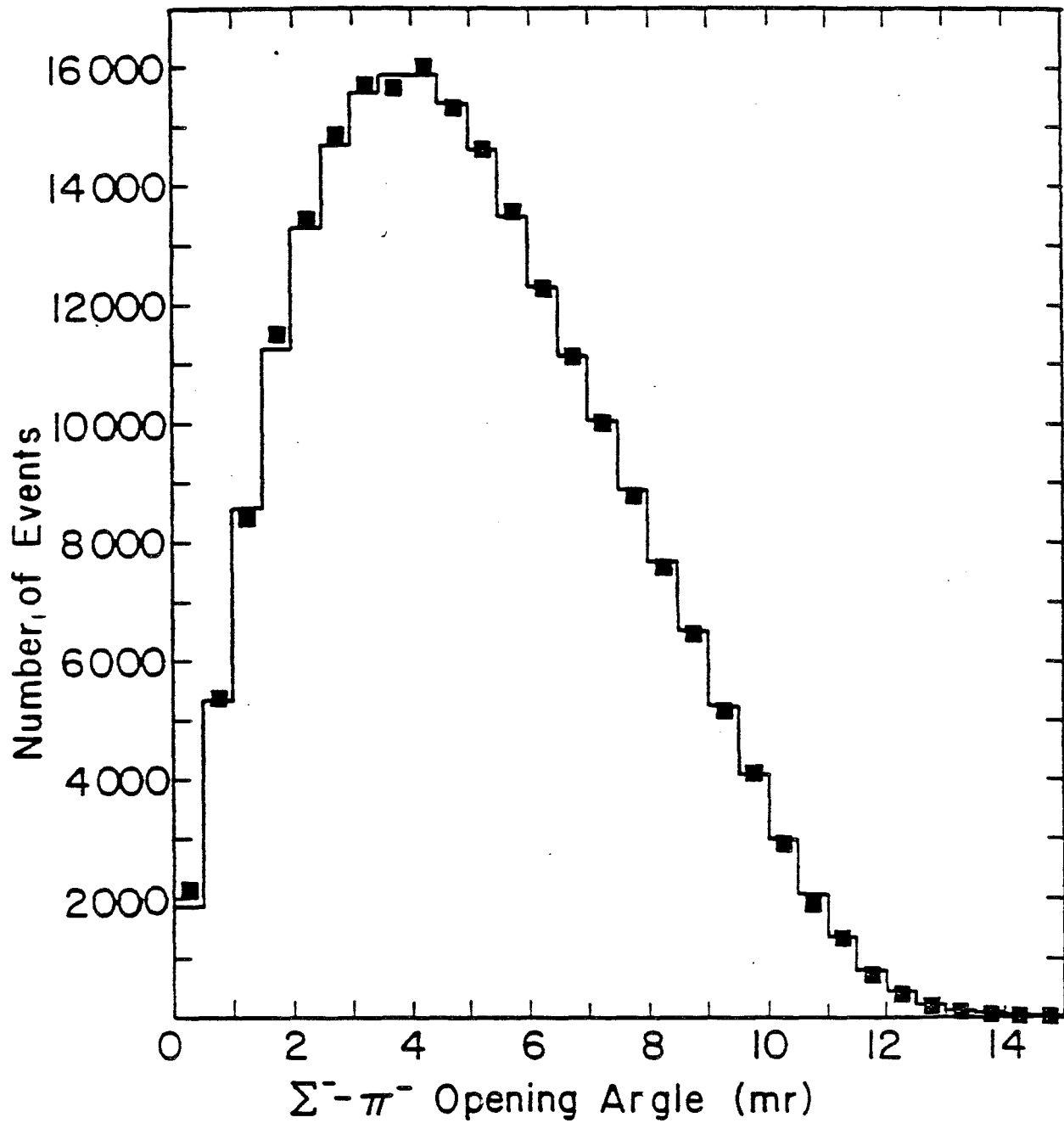


Fig. 20 A $\Sigma^- - \pi^-$ opening angle comparison plot between real and Monte Carlo events. The squares represent real data.

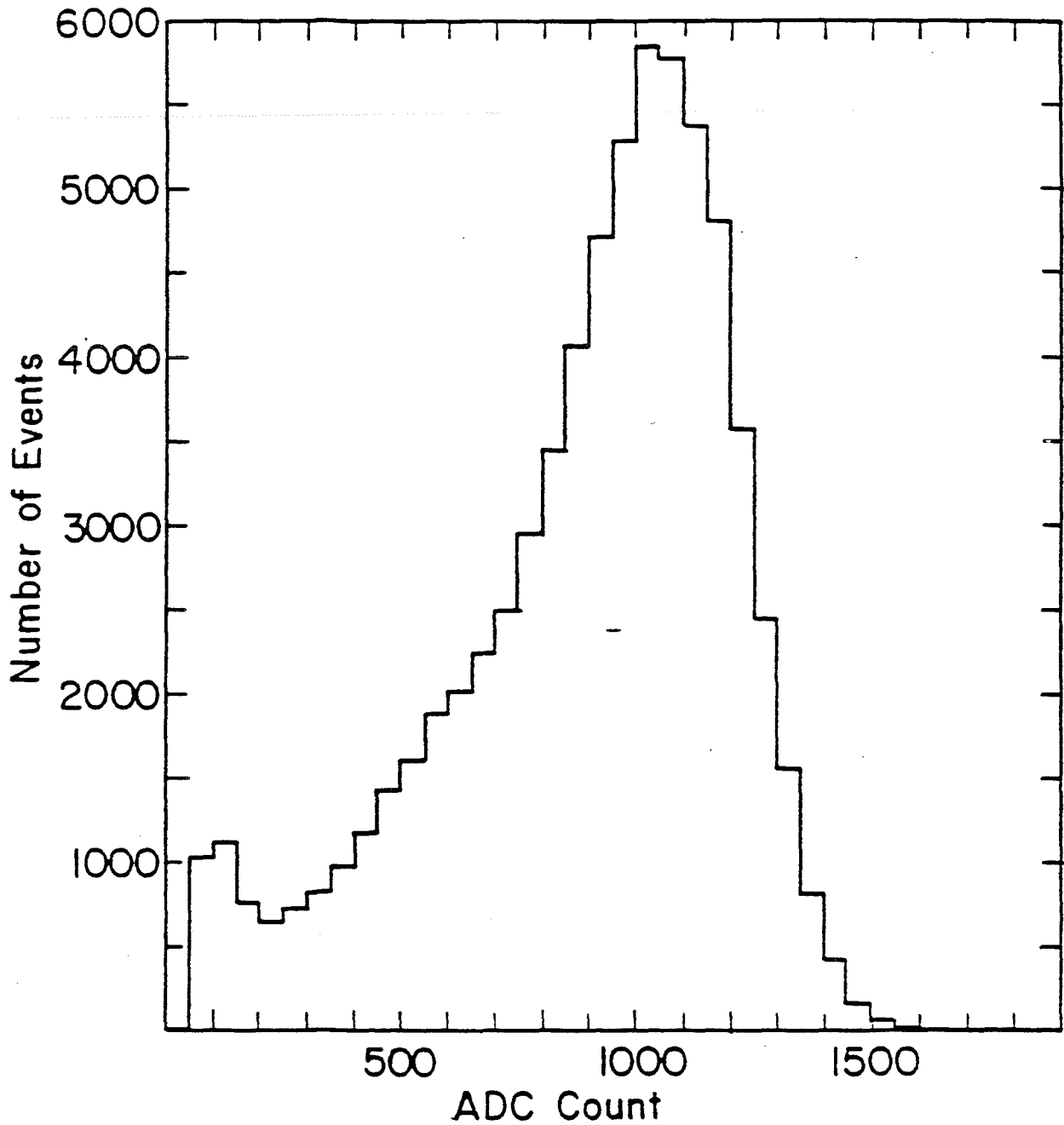


Fig. 21 The pulse height distribution of the sum of the neutron calorimeter counters 3, 4 and 5 for events that satisfy all cuts.

only 3.7 interaction lengths long, it would be of interest to cut this distribution and observe its effect on the results. Since we ignore the energy deposition in the front 2 scintillator sections where gammas will deposit all their energy a large fraction of the time, this cut will tend to eliminate any gamma contamination (from π^0 decay or stray gammas in the beam). The magnetic moment and polarization changed by less than 0.1 standard-deviations after this cut, which implies that the Pb in front of the veto, kinematic cuts and the small solid angle the NC subtended were very effective in eliminating gamma contamination. This cut was not made in the final analysis.

The background in the final sample from all sources was estimated by fitting the Σ^- mass peak in a Σ^- mass histogram where all cuts except the kinematic χ^2 cut were applied. A total background of 1.8% was obtained from this analysis. The backgrounds discussed in detail so far accounts for approximately 0.4% so the rest must be to a large extent poorly reconstructed Σ^- 's since other non- Σ^- sources have been clearly demonstrated to be negligible.

CHAPTER 4

DATA ANALYSIS II : POLARIZATION ANALYSIS

4.1 THE POLARIZATION ANALYSIS

The polarization of the Σ^- was determined from the asymmetry of the neutron distribution in the rest frame. The neutron distribution can be written:

$$dN(n) = (1 + \alpha_{\Sigma} \vec{P} \cdot \hat{p}_n) d\cos(\theta) \quad (16)$$

where $\alpha_{\Sigma} = -0.068 \pm 0.008$, \hat{p}_n is the neutron direction in the Σ^- rest frame, \vec{P} is the Σ^- polarization and $\cos(\theta) = \hat{P} \cdot \hat{p}_n$. The rest frame coordinate system chosen for this analysis was parallel to the LAB system defined earlier.

The distribution represented by equation (16) will describe the real event distribution only for perfect spectrometer acceptance and reconstruction program efficiency. Deviations from perfect acceptance will alter the shape of the $\cos(\beta)$ distributions. Thus the polarization analysis becomes that of measuring the acceptance as accurately as possible. The method used to determine the acceptance of the 3 components of the asymmetry was a Hybrid Monte Carlo technique described in more detail in Appendix 3.

For the January data this analysis was performed for two momentum bins chosen so that each had approximately the same number of events, as well as for the full sample. More subdivisions would, due to the small alpha parameter, only dilute the analysing power of each to too great an extent. The data were also split into positive and negative production angle. Momentum subdivisions in the December sample were not possible due to the small number of events. These data could then be combined in several ways to calculate the polarization and magnetic moment.

4.2 POLARIZATION AND BIASES

The Σ^- polarization at production was not determined directly in this experiment. However we expect Σ^- production to be a strong interaction process and hence conserve parity. So the polarization is expected to lie in the parity allowed direction $(\vec{k}_p \times \vec{k}_s)$ where \vec{k}_p (\vec{k}_s) is the incident proton (Σ^-) momentum direction. The collimator constrained \vec{k}_s to lie along the z-axis to within ± 1 mr, and \vec{k}_p was in the y-z plane, so the polarization at production was along either $+\hat{x}$ or $-\hat{x}$ (see Fig. 22). The precession field was in the $+\hat{y}$ direction throughout the experiment so the polarization precessed about the y axis in the horizontal plane. When the production angle was reversed the initial polarization direction reversed which allowed cancellation of acceptance asymmetries not accounted for by the MC.

The two Σ^- categories defined in section 3.2 have behaved similarly throughout the analysis and we will now give reasons for the categories to be combined. Table 7 lists the polarization signals for the two Σ^- categories in the January data and category 1 for the December data.

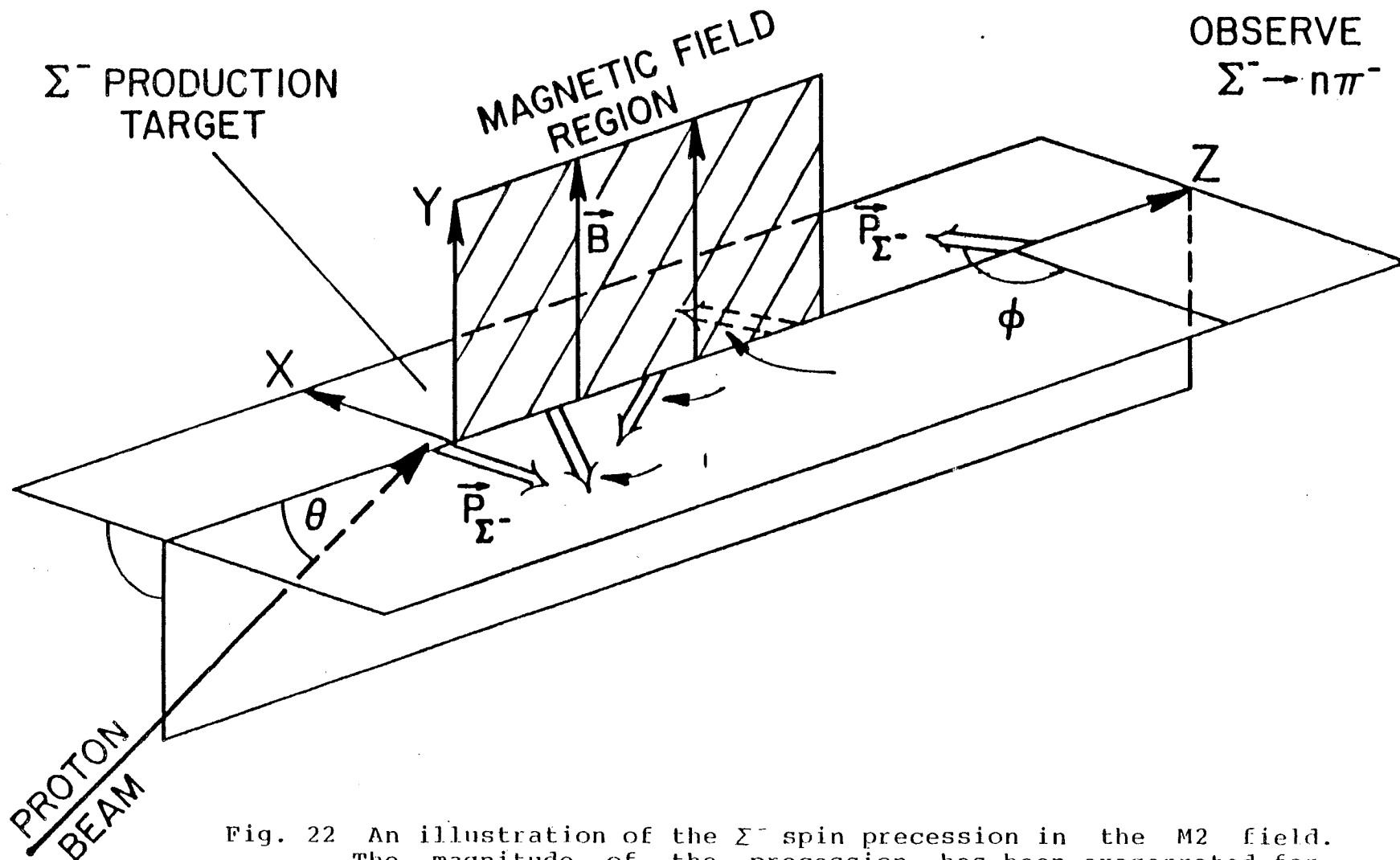


Fig. 22 An illustration of the Σ^- spin precession in the M2 field. The magnitude of the precession has been exaggerated for clarity. Not shown is the 10 mr bend in the orbit of the Σ^- .

A meaningful December category 2 polarization was not possible due to the small number of events. The results for the x and z polarizations also appear graphically in Figs. 23 and 24 along with their weighted averages and χ^2 of fit. Both x and z signals are nicely consistent. The spurious signal in the December y data can not effect our result since the polarization must lie in the xz plane. Its possible cause will be discussed later. Therefore the subsequent analysis uses the combined sample with no attempt to treat the two categories differently.

Table 8 shows the polarization signals and biases for each polarization component and the biases are graphically displayed in Fig. 25. The January y components are all consistent with zero, which gives support for the bias-cancelling abilities of our approach. The origin of the y signal in the December sample has been vigorously explored but the search has not been entirely successful. A possible cause will be discussed later in this section.

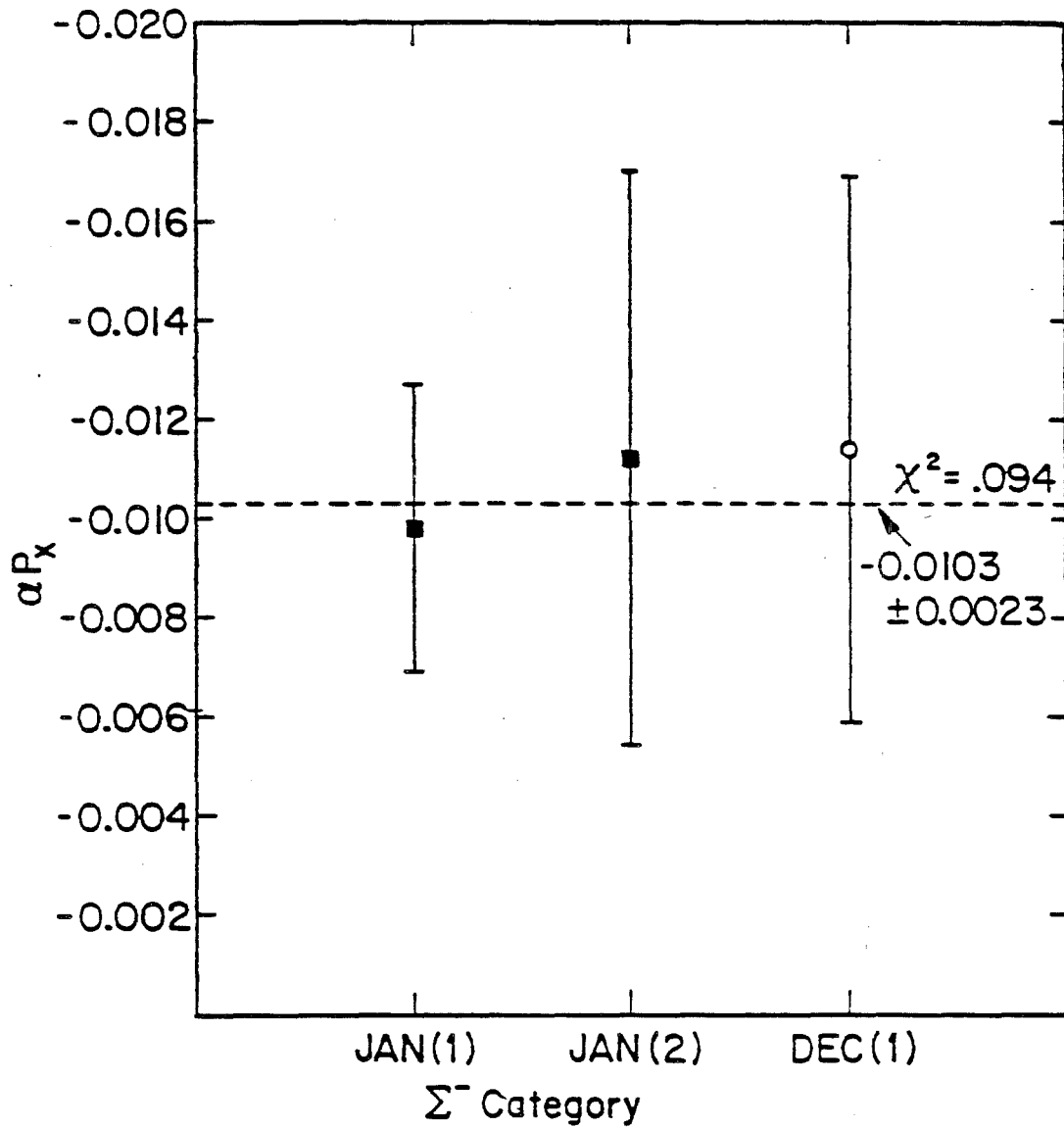


Fig. 23 The values of αP_x determined for the several Σ^- categories. The χ^2 categories are explained in the text.

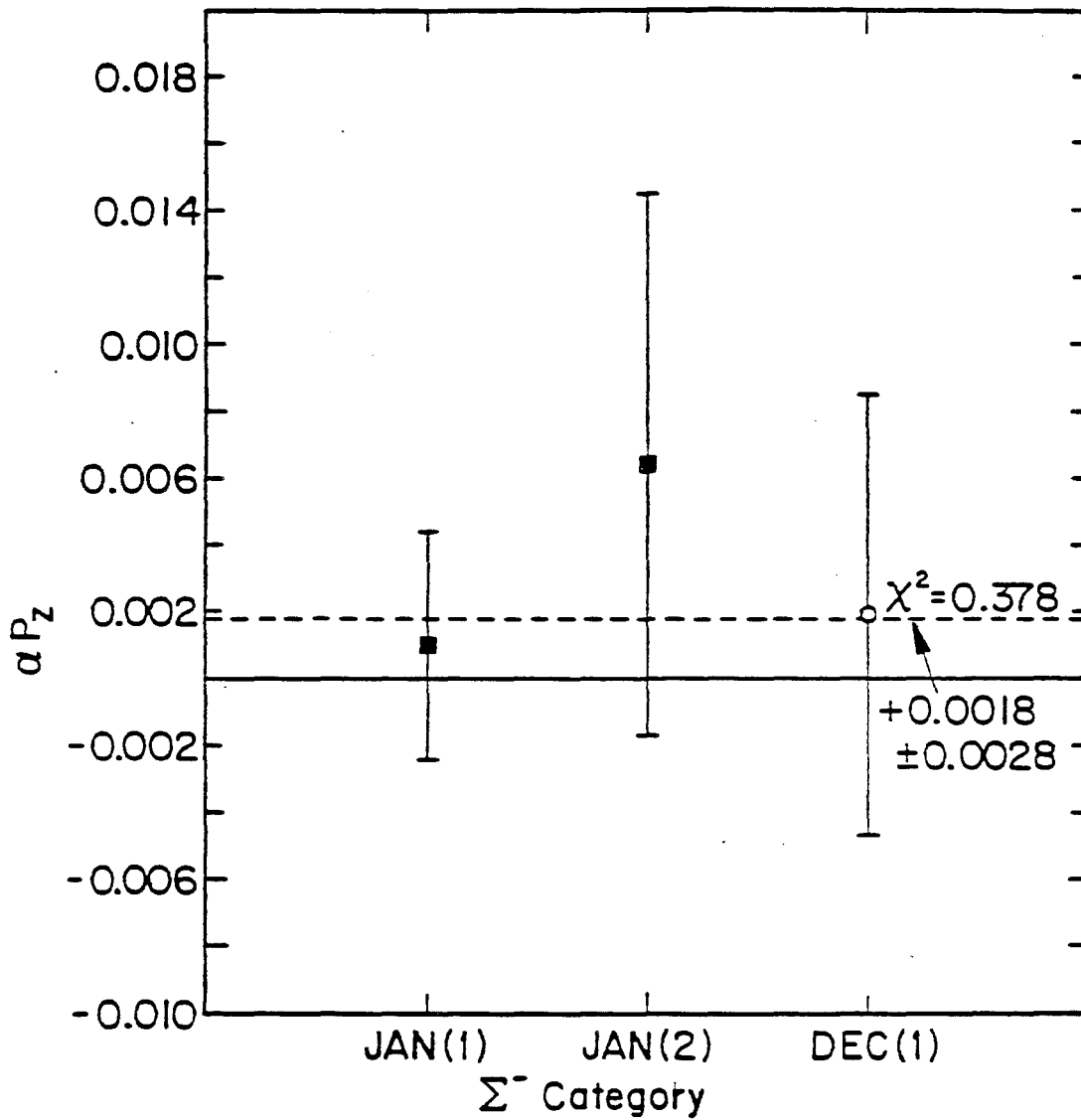


Fig. 24 The values of αP_z determined for the several Σ^- categories. The Σ^- categories are explained in the text.

Data (category)	αP_x	BIAS
JAN (1)	-0.0098 ± 0.0029	-0.0279 ± 0.0029
JAN (2)	-0.0112 ± 0.0058	$+0.0298 \pm 0.0058$
DEC (1)	-0.0114 ± 0.0055	$+0.0512 \pm 0.0055$

Data (category)	αP_y	BIAS
JAN (1)	$+0.0014 \pm 0.0032$	-0.0506 ± 0.0032
JAN (2)	-0.0021 ± 0.0070	-0.0301 ± 0.0070
DEC (1)	-0.0128 ± 0.0061	-0.0880 ± 0.0061

Data (category)	αP_z	BIAS
JAN (1)	$+0.0010 \pm 0.0034$	-0.0480 ± 0.0034
JAN (2)	$+0.0064 \pm 0.0081$	-0.0631 ± 0.0081
DEC (1)	$+0.0019 \pm 0.0066$	-0.0680 ± 0.0066

Table 7 The Polarization signals and Biases for the $2 \Sigma^-$ categories in both data sets. The mean momentum of each category was 176 GeV.

The hybrid MC determined the apparatus acceptance as a function of the different $\cos(\theta)$ components through the use of a program that attempted to simulate the apparatus apertures and trigger requirements as closely as possible. Unfortunately in practice the apparatus and apertures can not be perfectly understood and simulated. This is

X Polarization Signals and Biases

Data (bin)	P	P_t	x_F	P_x	Bias
Jan (partial)	154	1.16	0.38	-0.0092±0.0034	-0.0171±0.0034
Jan (partial)	202	1.52	0.50	-0.0112±0.0038	-0.0159±0.0038
Jan (full)	176	1.32	0.44	-0.0100±0.0025	-0.0166±0.0025
Dec (full)	175	1.31	0.44	-0.0116±0.0050	+0.0581±0.0050

Y Polarization Signals and Biases

Data (bin)	P	P_t	x_F	P_y	Bias
Jan (partial)	154	1.16	0.38	+0.0006±0.0040	-0.0493±0.0040
Jan (partial)	202	1.52	0.50	+0.0010±0.0041	-0.0447±0.0041
Jan (full)	176	1.32	0.44	+0.0009±0.0029	-0.0471±0.0029
Dec (full)	175	1.31	0.44	-0.0083±0.0055	-0.0865±0.0055

Z Polarization Signals and Biases

Data (bin)	P	P_t	x_F	P_z	Bias
Jan (partial)	154	1.16	0.38	+0.0027±0.0046	-0.0883±0.0046
Jan (partial)	202	1.52	0.50	+0.0004±0.0043	-0.0157±0.0043
Jan (full)	176	1.32	0.44	+0.0020±0.0031	-0.0505±0.0031
Dec (full)	175	1.31	0.44	+0.0024±0.0061	-0.0625±0.0061

Table 8 The X, Y and Z polarization signals and biases for all the data. All momenta are in units of GeV/c.

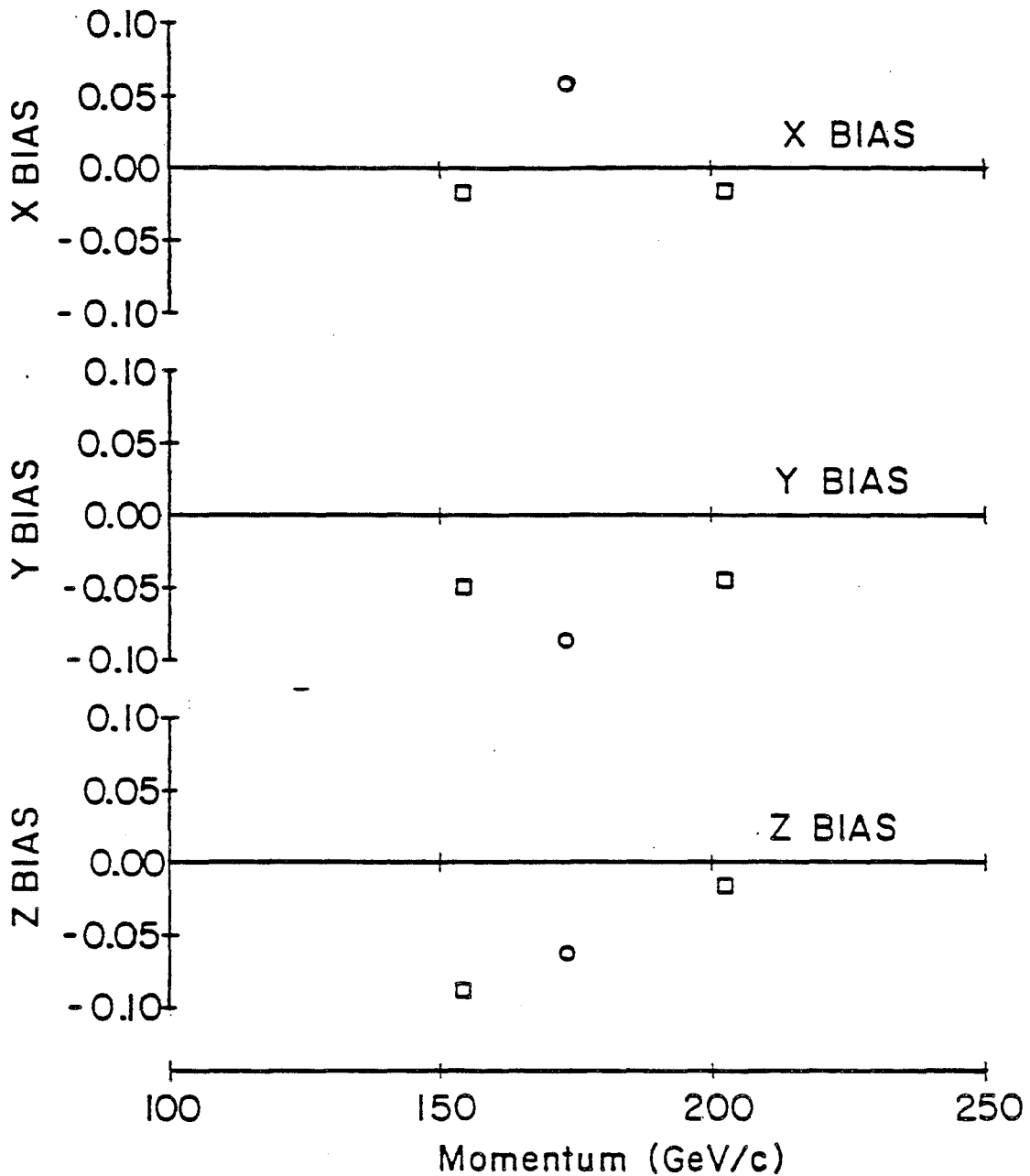


Fig. 25 The x, y and z biases for several statistically independent samples of data. The squares are the high and low momentum January data bins. The circle is all the December data. The difference in the biases is the result of changes in the experimental configuration.

because of edge effects, magnet field imperfections, small chamber and scintillator inefficiencies, resolution and reconstruction problems and backgrounds. These problems cause the hybrid MC to calculate the wrong apparatus acceptance which give rise to spurious asymmetries called biases. These biases however are easily cancelled if equal amounts of positive and negative production angle events are analysed and the resulting asymmetry signals subtracted. Since the polarization changes sign for opposite production angles while the bias does not, a simple subtraction of the form:

$$\alpha P_+ - \alpha P_- = \alpha P + B - (-\alpha P + B) = 2\alpha P$$

removes the biases completely to the extent that the biases are time and production angle independent.

The first requirement, that the biases be time independent, means that the time scale for changes in the apparatus acceptance be small with respect to the time it takes to take an equal amount of data at plus and minus production angle. This took a little over six hours in the December data and 8 hours in the January data since production angles were changed every other tape. The consistency of the data in regards to bias cancellation

gives reasonable assurance that time dependent effects are small. See section 4.6.

The requirement that the biases be independent of production angle is more open to question. Previous experiments using this apparatus have demonstrated that the x and z biases are indeed production angle independent,^(6,13) and it is obvious that since the incident proton's momentum phase space is only changed in y for different production angles, a production angle change should change only the Σ^- y momentum phase space. This means that the Σ^- beam centroid is higher for positive production angle than negative and the chamber active areas covered by the events are on the average different for different angles. Fig. 26 is a comparison of the neutron y distributions at the NC for different production angles and clearly shows this effect. Thus, for example, small y dependent chamber inefficiencies will create biases that will not cancel. Another more serious problem is that since the NC is a limiting aperture, parts of the neutron distribution will be lost due to this effect. These losses will involve different parts of $\cos(\theta_y)$ for different production angles and due to resolution one can not be sure that one has accounted for

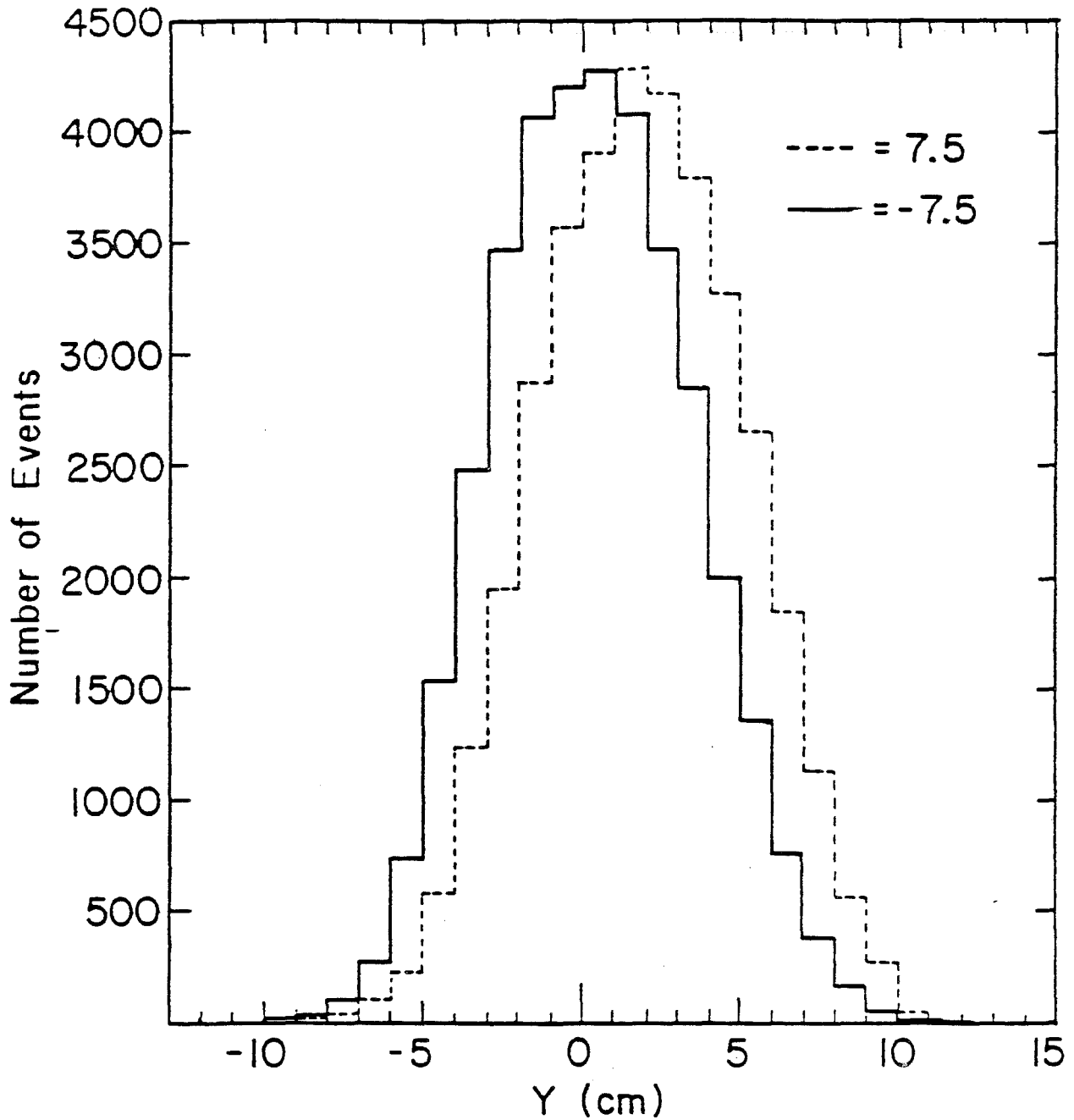


Fig. 26 The neutron y distributions at the neutron calorimeter for the two production angles. This effect is the most probable cause of the small y component of polarization in the December data.

this aperture correctly in the IMC programs.

This is probably the cause of the y signal in the December data. The major spectrometer differences in the two data runs were the DC efficiencies and the position and depth of the NC. The fact that the December y signal is independent of decay vertex cuts suggests that the DC efficiencies are not the cause. However in January the NC center was raised slightly to center it on the beam determined by the December data and the NC itself was modified from 3.0 to 3.7 interaction lengths with the addition of another scintillator section. These two changes improved the uniformity and symmetry of the NC so that bias cancellation was more complete.

It is useful to note that a comparison of the neutron x distributions (Fig. 27) for the two different production angles shows almost perfect agreement. This coupled with the fact that the NC was less of a limiting aperture in x than y means that potential bias cancellation problems similar to those in y for the December data should be considerably reduced.

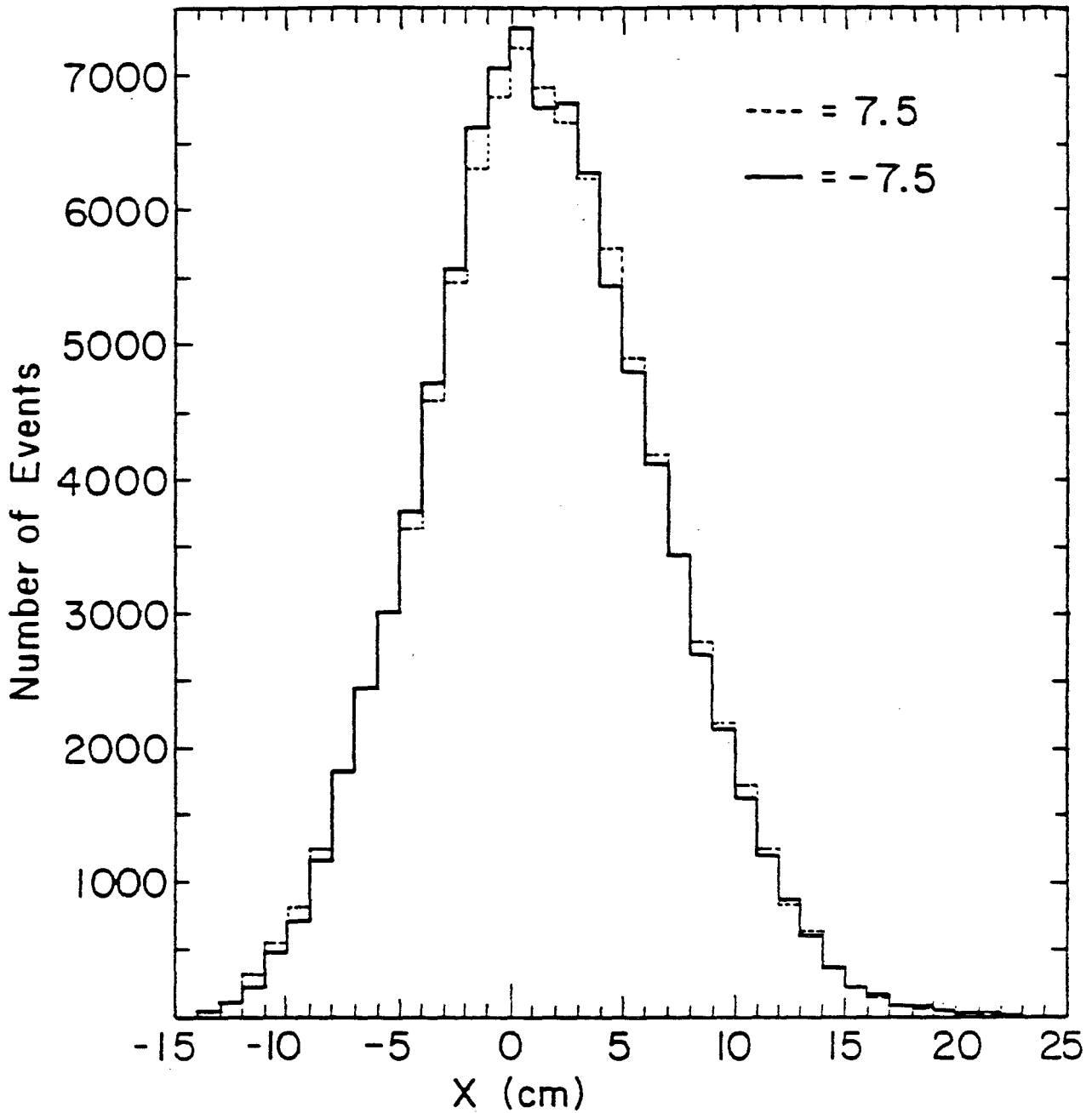


Fig. 27 The neutron x distributions at the neutron calorimeter for the two production angles. The systematic shift seen in y (Fig. 26) is absent here where our strongest polarization component is observed.

Other effects related to backgrounds must be considered. Biases produced by backgrounds might not cancel completely if the spectrometer acceptance for that background's particular decay mode changes appreciably for different production angles. To test this possibility, the relative percentages of Ξ^- 's was determined for the two production angles to see if they differed. A small difference was discovered, positive production angle percentages being larger by $6.7 \pm 1.4\%$ over negative, but this effect can at most change the $\cos(\theta_z)$ polarization signal by 0.0001, and would effect the other components even less.

Also considered was the effect of a polarized sample of Ξ^- background. Here the effect was largest in x where it at most could influence the $\cos(\theta_x)$ polarization signal by 0.00014. These signals are well within our statistical uncertainties and are therefore negligible. See Appendix 4 for a detailed discussion of how these two effects influence the asymmetry calculation.

4.3 POLARIZATION RESULTS

Using the values of the components of the polarization signals given in Table 8, we obtain the magnitude of the polarization as a function of momentum. The results are shown in Table 9 and in Fig. 28. The polarizations are in very good agreement with other hyperons in this Feynman x and transverse momentum range. (6,7,13)

Data (bin)	Momentum (GeV/c)	P_t	x	% Polarization
Jan (partial)	154	1.16	0.38	14.1 ± 5.4
Jan (partial)	202	1.52	0.50	16.5 ± 5.9
Jan (full)	176	1.32	0.44	15.0 ± 4.1
Dec (full)	175	1.31	0.44	17.4 ± 7.8
combined	176	1.32	0.44	15.5 ± 3.6

Table 9 The Polarization Magnitudes for all the Data.

4.4 PRECESSION ANALYSIS AND MAGNETIC MOMENT

The polarization in x is a 4.5 standard-deviation effect and we believe that we understand systematics and

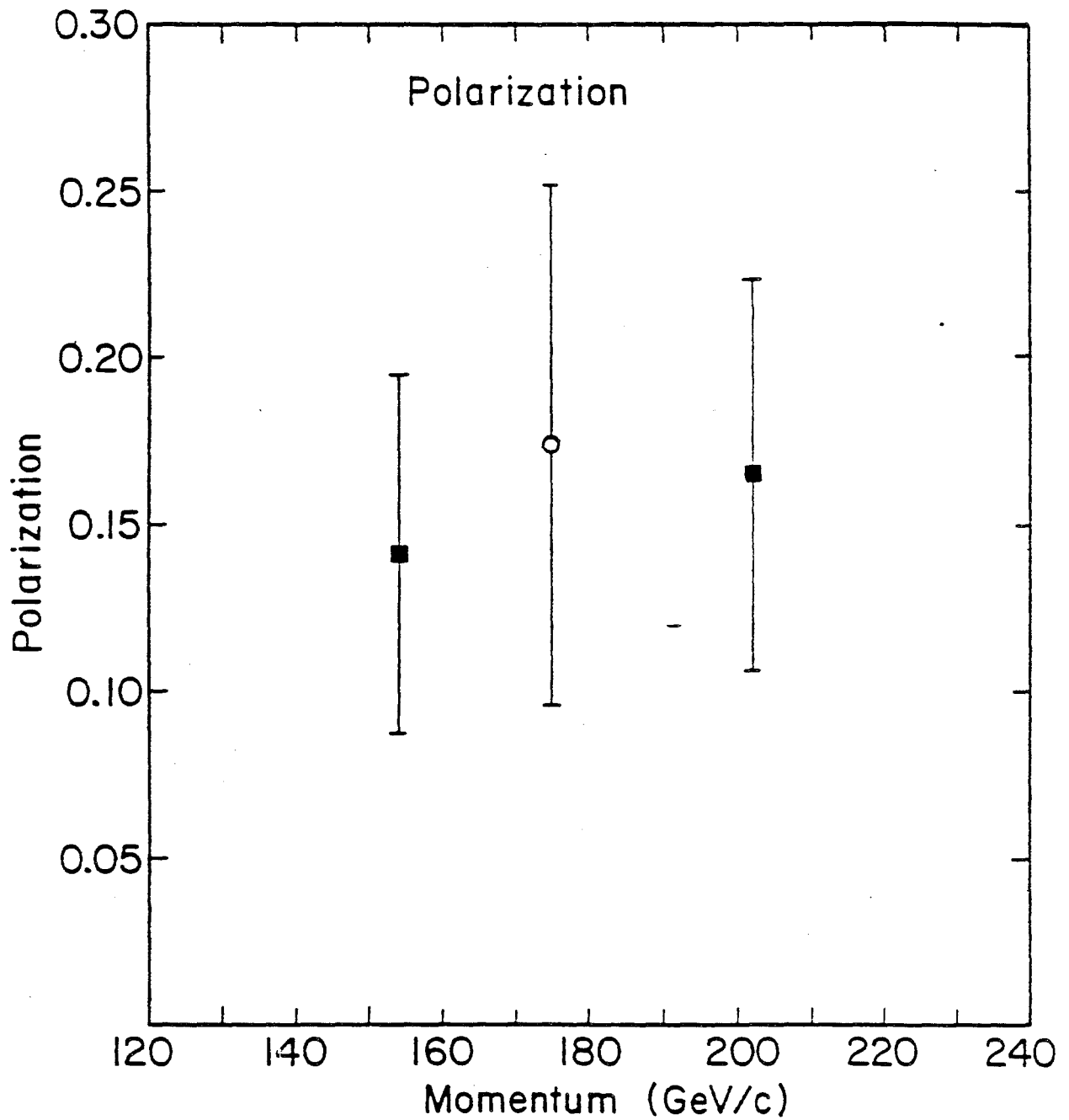


Fig. 28 The magnitude of the polarization for the three data samples.

backgrounds to a level that makes this polarization significant. Therefore the direction of the polarization is also significant and can be used to calculate the magnetic moment.

Since the polarization at production could have been in the $+\hat{x}$ or $-\hat{x}$ direction and precession could have been in the clockwise or counterclockwise sense, there are four separate precession configurations if we rule out higher order solutions (precession angles greater than 27°). These four basic precession configurations are shown in Fig. 29 and the moments obtained from each are listed in Table 10. Use has been made of equation (15) in section 1.2 with $\int \vec{B} d\vec{l} = 5.94 \text{ T}\cdot\text{m}$. The precession sense is defined as positive for positive rotations about the y axis.

If one is confident that the sign of the Σ^- magnetic moment has been sufficiently well determined by preceding experiments, the number of possible precession configurations reduces to the two that give the correct precession sense. These two surviving solutions are numbered 1 and 2 in Table 10. Only solution 1 is consistent with previous experiments and the broken SU(6) model and it implies a polarization in the positive \hat{x}

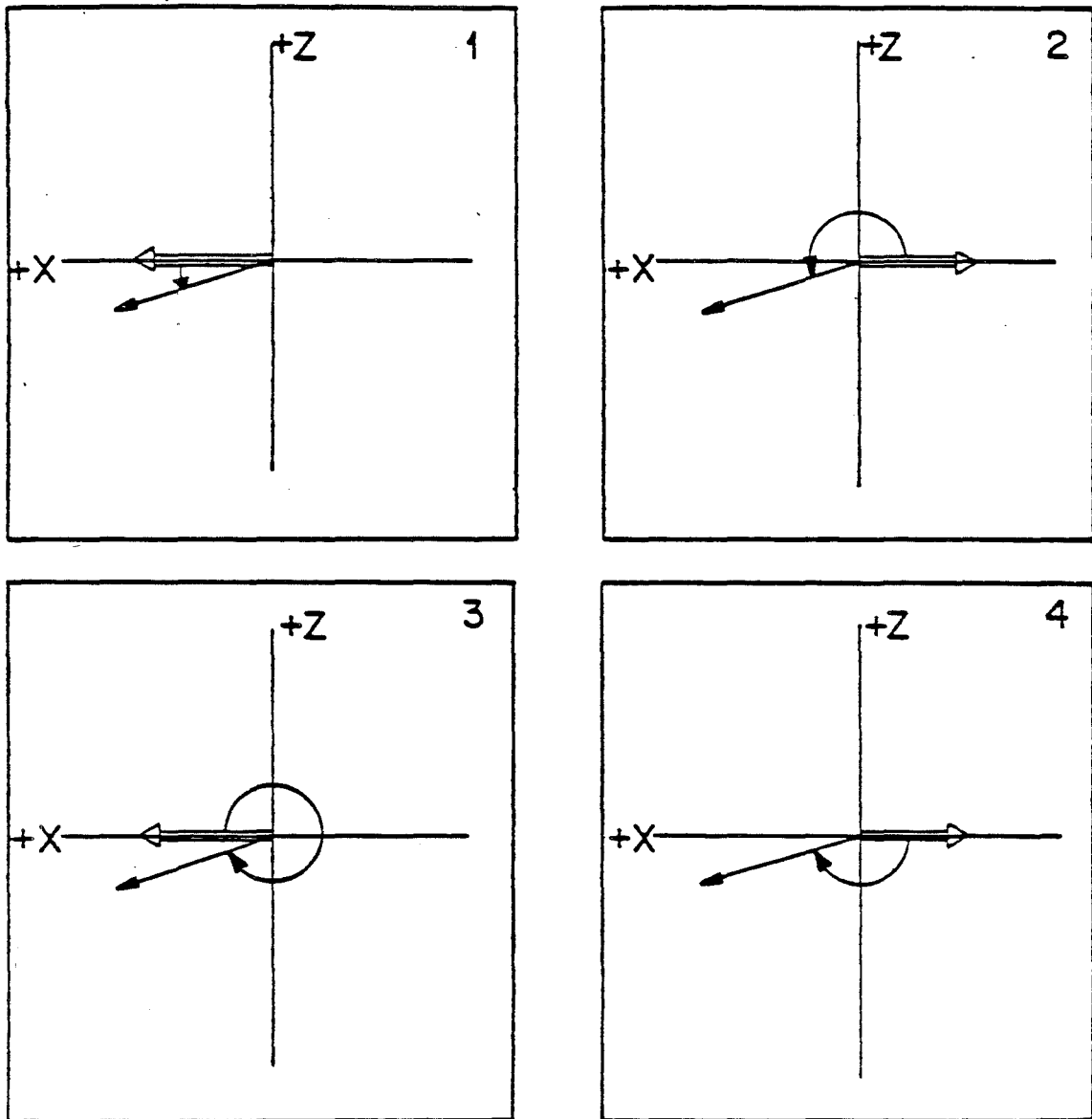


Fig. 29 The four lowest order precession configurations. Each represents a different way to interpret the data.

direction at production.

	PRECESSION ANGLE	POL. AT TGT.	MAGNETIC MOMENT
(1)	$+11^\circ \pm 15^\circ$	$+(k_p \times k_s)$	$-0.89 \pm 0.14 \mu_N$
(2)	$+191^\circ \pm 15^\circ$	$-(k_p \times k_s)$	$-2.54 \pm 0.14 \mu_N$
(3)	$-349^\circ \pm 15^\circ$	$+(k_p \times k_s)$	$+2.42 \pm 0.14 \mu_N$
(4)	$-169^\circ \pm 15^\circ$	$-(k_p \times k_s)$	$+0.77 \pm 0.14 \mu_N$

Table 10 The four lowest order precession configurations and their moments.

4.5 SYSTEMATICS

The asymmetries are in general very sensitive to changes in the apparatus acceptance. However the magnetic moment formed from these asymmetries should be independent of all acceptance changes whether they occur in the apparatus itself or are generated artificially through cuts. The stability of the magnetic moment to various cuts is therefore our only check on possible systematic errors in the acceptance calculation.

Figures 30 through 32 show the variation of the magnetic moment to different cuts used to determine the Σ^- sample. The precession assumed for these graphs was counterclockwise and measured from $+\hat{x}$. These figures show that the magnetic moment is insensitive to these cuts as it should be.

Fig. 33 shows the magnetic moment as a function of momentum for both the January and December data samples. The magnetic moment is clearly consistent with no momentum dependence. Since the acceptance and biases are momentum dependent (Fig. 19 and Fig. 25), the momentum independence of the moment as well as its independence to different data taking conditions is strong evidence that biases have been cancelled correctly.

4.6 TIME DEPENDENT SYSTEMATICS

Time dependent changes in the apparatus acceptance can give rise to systematic errors in the polarization analysis. This effect can be present but hidden because it is mistakenly associated as a part of the polarization

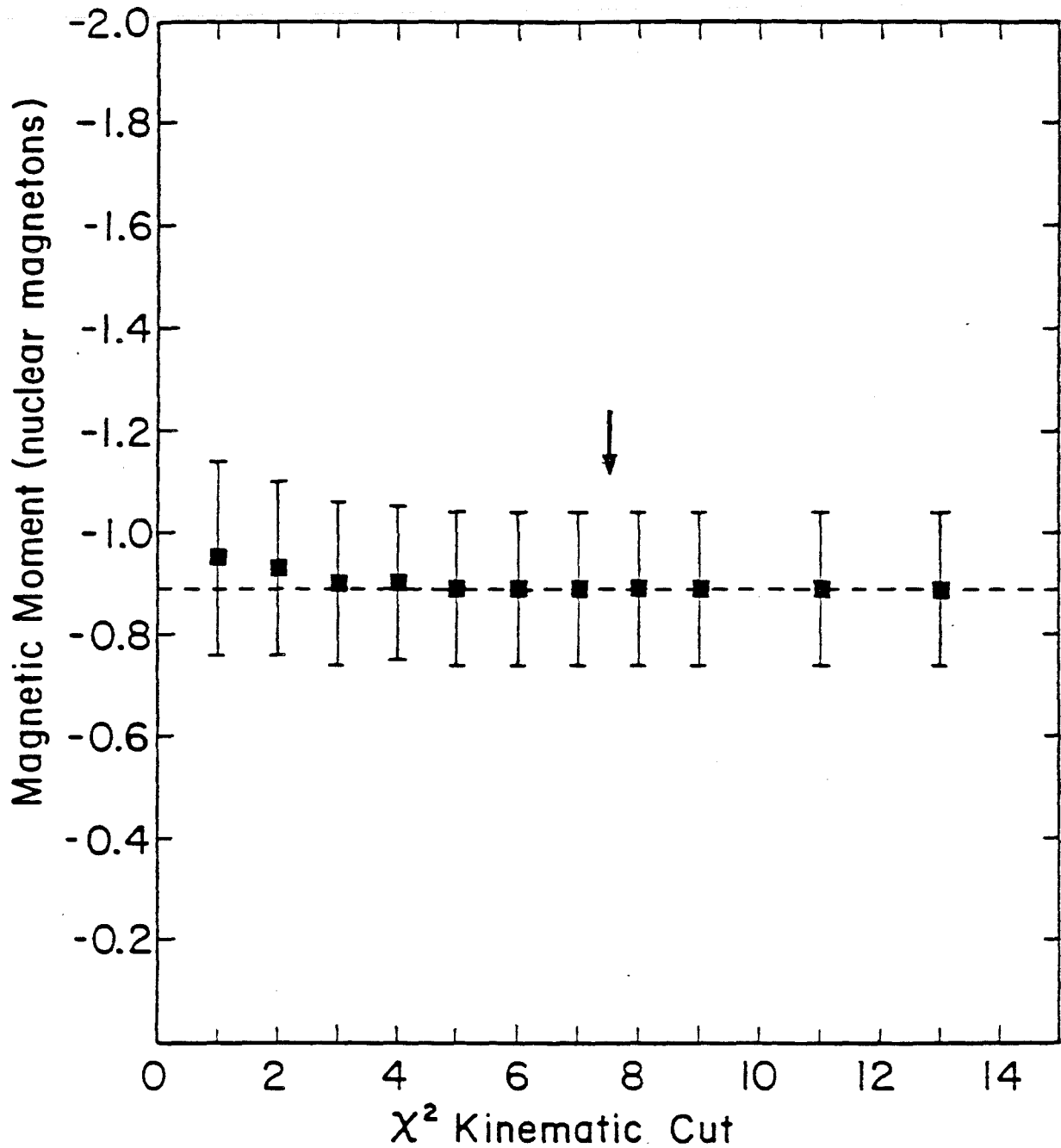


Fig. 30 The variation of the magnetic moment for different values of the cut on the kinematic χ^2 . The arrow indicates the value used in the final analysis.

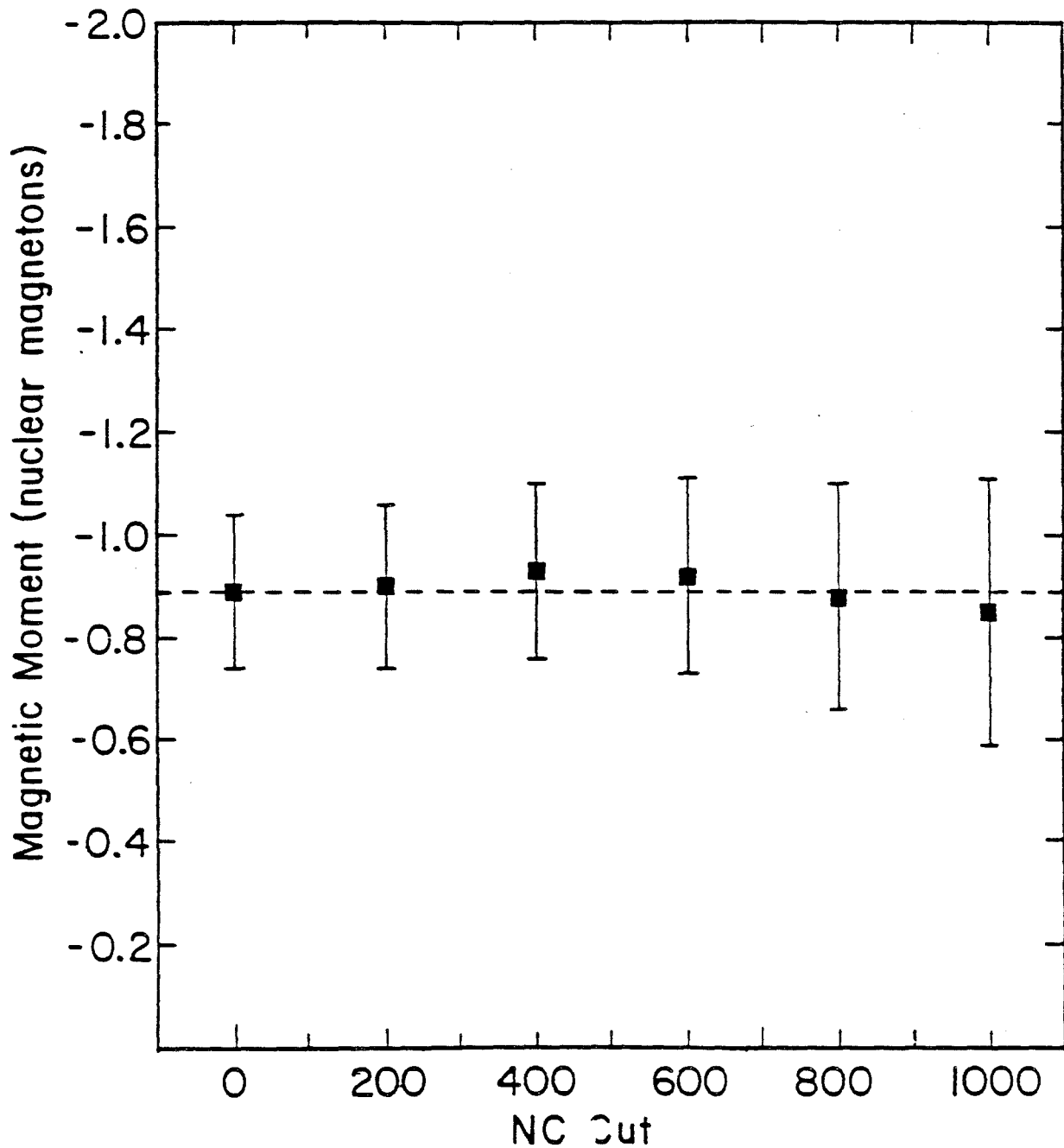


Fig. 31 The variation of the magnetic moment for different values of a cut on the neutron calorimeter pulse height distribution (Fig. 21).

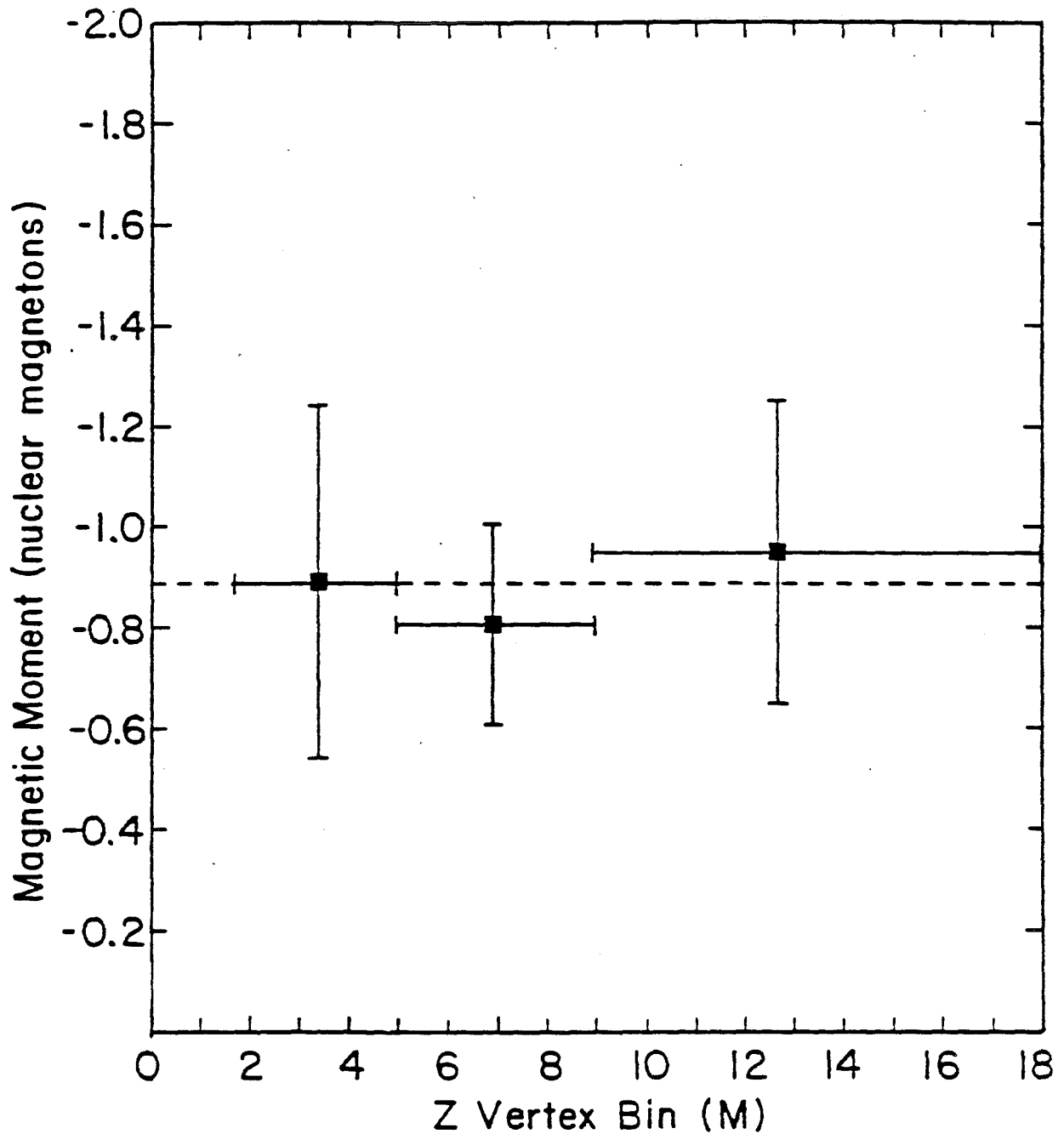


Fig. 32 The magnetic moment calculated for three different decay vertex bins. The extent of the bins is shown by the horizontal error bars.

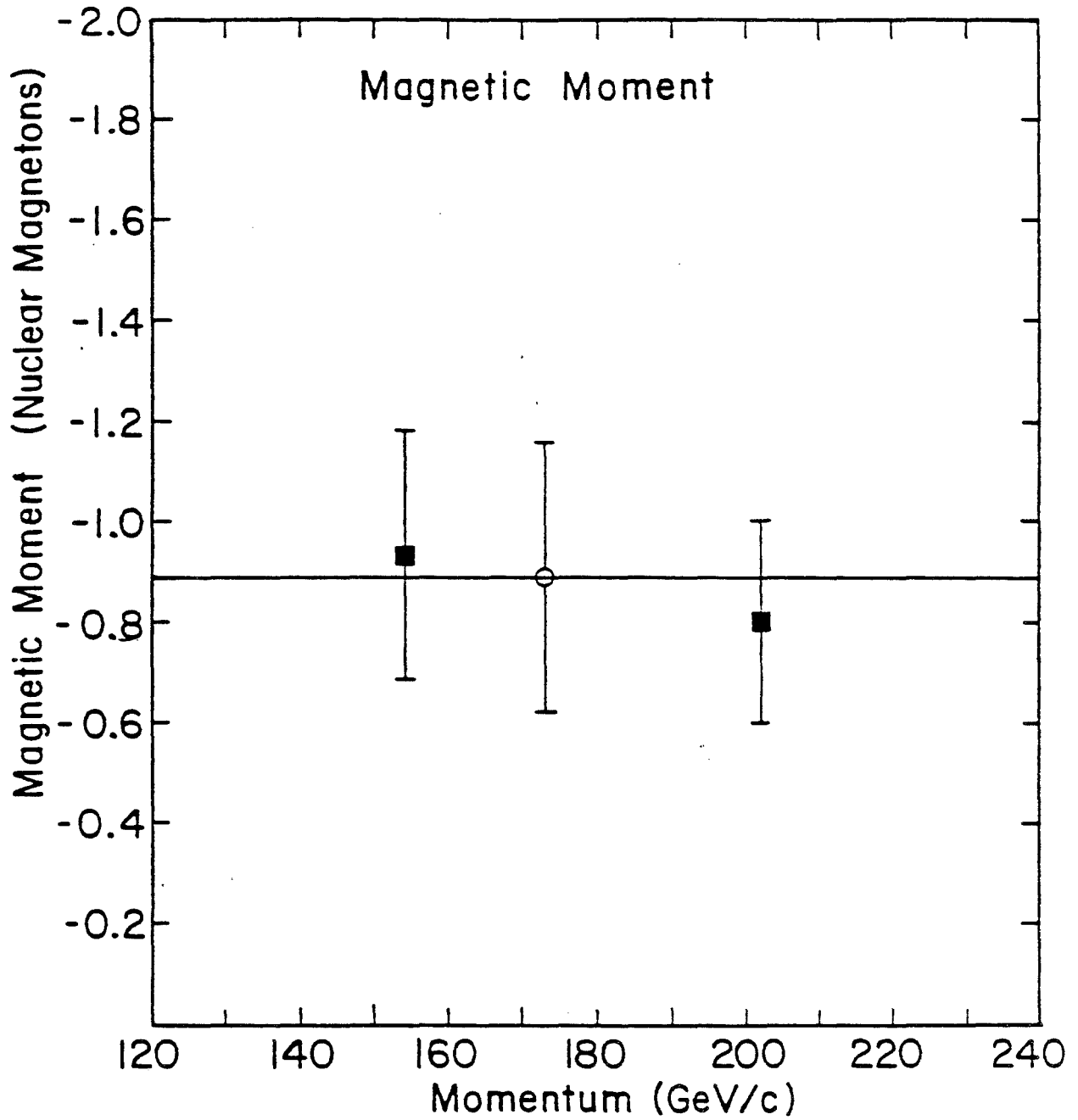


Fig. 33 The magnetic moment for the three data samples as a function of momentum.

signal. A measure of this effect can be obtained by combining data in such a way as to eliminate the polarization but retaining the chronological ordering. In the data set used to obtain the polarization result, the runs were separated by production angle. If the data runs are numbered chronologically, then in this set one tape contained runs (1,2), (5,6), (9,10),..., while the other tape contained runs (3,4), (7,8), (11,12),... If a data set is made where one tape contains runs (2,3), (6,7), (10,11),..., while the other contains (4,5), (8,9), (12,13),..., then the net polarization in either tape would be zero since they contain equal amounts of opposite production angle data, but the time ordering and natural periodicity are retained. A polarization analysis on this set should yield zero "polarization" for all components if time dependent systematic errors are absent. This analysis was performed and the results are shown in Table 11. All the polarization components are consistent with zero to within 0.5σ . This result strongly supports our belief that time dependent effects are negligible and that the biases cancel to at least the level of our statistical uncertainty.

αP_x	αP_y	αP_z
0.0010 ± 0.0026	0.0010 ± 0.0029	0.0016 ± 0.0032

Table 11 The "polarization" signals for the data when determining time dependent effects.

CHAPTER 5

RESULTS

The polarization of inclusively produced Σ^- 's on Be at 7.5 mrad lab angle is shown in Fig. 30 and Table 9. For the entire data set it is $(15.5 \pm 3.6)\%$. Its direction at production was not measured, but only the solution along $+\hat{x}$ yields a value of the magnetic moment consistent with the fine structure measurement and all theoretical models of baryon structure.

A value for the Σ^- magnetic moment was also measured and found to be,

$$\mu_{\Sigma^-} = -0.89 \pm 0.14 \mu_N$$

The quoted uncertainty is statistical. Backgrounds from all sources are estimated to be less than 1.8%. Systematic uncertainties are estimated to be less than and of the order of the statistical uncertainty. Other solutions consistent with the data are possible, but none is consistent with the fine structure result or current theoretical models.

APPENDIX 1

THE EXTERNAL MONTE CARLO

A Monte Carlo program is an essential tool for all high energy physics experiments. This experiment was no exception. However to distinguish the standard Monte Carlo from the one used in the polarization analysis, the standard Monte Carlo will be called an "external Monte Carlo" (MC), while we will reserve the term "internal Monte Carlo" (IMC) for the other.

The MC written for this experiment had the following characteristics.

- 1) It simulated the M2 beam channel as completely as possible to understand the momentum-position correlations in the spectrometer.

- 2) The Σ^- momentum spectrum was reproduced as closely as possible so that momentum dependent acceptances could be studied.
- 3) All chamber, counter and magnet positions were as in the actual experiment.
- 4) The efficiencies and resolutions of the MWPC's and DC's were as in the actual experiment.
- 5) A number of types of particles and their decay modes expected to be in the real beam were built into the MC to study their effect on various distributions as well as to determine the efficiency of the reconstruction and analysis programs. Those included were,

$$\Sigma^- \rightarrow n + \pi^-$$

$$\Xi^- \rightarrow \Lambda^0 + \pi^- \quad , \quad \Lambda^0 \rightarrow n + \pi^0$$

$$K^- \rightarrow \pi^- + \pi^0$$

$$\pi^- + N \rightarrow N + \pi^-$$

$$\pi^- \rightarrow \mu^- + \nu$$

straight tracks

- 6) The Σ^- 's could be polarized along any direction to study the effect on various distributions as well as debug the polarization analysis programs.

APPENDIX 2

THE NONUNIFORMITY OF THE M3 FIELD INTEGRAL

Early in the analysis the data suffered from a loss of low momentum π^- events and poor y residuals downstream of the analyzing magnet M3. It was discovered that a nonuniform field in M3 was responsible. The field was nonuniform at the 1% level and as such did not appreciably affect the other hyperon magnetic moment measurements since they enjoyed much more constrained fits. Also the effect was larger in this data due to the z position of chamber 8. Its longer lever arm made the effect more significant.

A field map for M3, measured in an earlier experiment, was analyzed for nonuniformity. Specifically the y component of the field integral " B_y " was parametrized as a function of the average x and y position at the center of

M3. Maxwell's equations then yielded the x component " B_x " as a fraction of the total field integral " B_0 ". This fraction was found to be:

$$\frac{B_x}{B_0} = A + Bx + Cyx^2 + Dx^3 \text{ with,}$$

$$A = 2.819 \times 10^{-3}$$

$$B = 4.197 \times 10^{-4} \text{ cm}^{-1}$$

$$C = -9.907 \times 10^{-7} \text{ cm}^{-3}$$

$$D = 3.302 \times 10^{-7} \text{ cm}^{-3}$$

Using this correction the residual problem was solved and more low momentum π^- events were recovered. Finally the B_x field was measured by the data itself using the deviations of straight tracks downstream of M3 from their line of flight as determined from the upstream chambers. The parametrization was identical to B_x given above and the measured values of the coefficients were:

$$A = 1.601 \times 10^{-3}$$

$$B = 5.152 \times 10^{-4} \text{ cm}^{-1}$$

$$C = -15.06 \times 10^{-7} \text{ cm}^{-3}$$

$$D = 1.607 \times 10^{-7} \text{ cm}^{-3}$$

The difference in A could easily arise from a difference in the definition of the centers of M3. The field map used the geometric center while the data fit used the center defined from the straight-through. The coefficient B, a quadrupole moment, agrees well. The higher terms are less important and are not well determined by the track analysis since they do not sample large values of x.

The strong similarity between these values and the values obtained directly from the field map gave confidence that the problem was solved. This correction was used for all the data.

APPENDIX 3

THE HYBRID MONTE CARLO METHOD

The polarization analysis in this experiment was performed using a hybrid Monte Carlo method.⁽³³⁾ This is essentially a least squares fit of the data to the function:

$$F=A(p,r)(1+\alpha P\cos(\theta))$$

where $A(p,r)$ is a momentum and production-angle dependent acceptance function which is determined in the following way.

For each real event, Monte Carlo events, called internal Monte Carlo events (IMC), were generated isotropically and tested for acceptance in a program designed to reproduce the experimental apertures and trigger requirements until 30 IMC passed the acceptance

criteria. In this way the IMC event distributions had the apparatus acceptance folded in. All variables that have nothing to do with the physics of the polarization, called spectator variables, are taken from the real event. These variables include the Σ^- momentum components and the decay vertex. The IMC $\cos(\theta)$ distributions were then "polarized" (i.e. the shapes of the $\cos(\theta)$ plots were changed in a normalized way in accordance with the equation, $(1 + \alpha P \cos(\theta))$ until the χ^2 for the deviation from the real event $\cos(\theta)$ distributions was minimized.

There are two complications in the above approach. First, some way must be found to "polarize" the MC distributions AFTER the acceptance is found. This means that an analytic function which describes the shape of the $\cos(\theta)$ distribution as a function of polarization and acceptance is needed. Second is the effect of the real polarization on the IMC acceptance calculation. The acceptance calculation depends on the the values of the spectator variables and these values are on the average different in a polarized sample than in an unpolarized one. An elegant solution for these two problems is to attach to each real event a weight W which is proportional to its occurrence probability for a specific polarization.

Hence the real event sample is "unpolarized" by dividing each event by its occurrence probability. To this end we define for each IMC event a weight:

$$W = (1 + \alpha P_{mc} \cos(\theta_{mc})) / (1 + \alpha P_r \cos(\theta_r))$$

where in effect the denominator divides out the effect of the real polarization and the numerator polarizes the IMC distributions. Since $\alpha P_{mc} = \alpha P_r$ after the fit, the weight was expanded in terms of αP :

$$W = 1 + \sum_i (-\alpha P)^i (\cos(\theta_r))^{i-1} (\cos(\theta_r) - \cos(\theta_{mc}))$$

and only the first four terms were kept. This results in an analytic function of the shape of the $\cos(\theta)$ distributions with respect to the polarization and conventional minimization techniques were employed to obtain the polarization components.

Figs. 34 through 36 illustrate this procedure with comparison plots of real and MC $\cos(\theta)$ distributions after the minimization process was completed for both production angles.

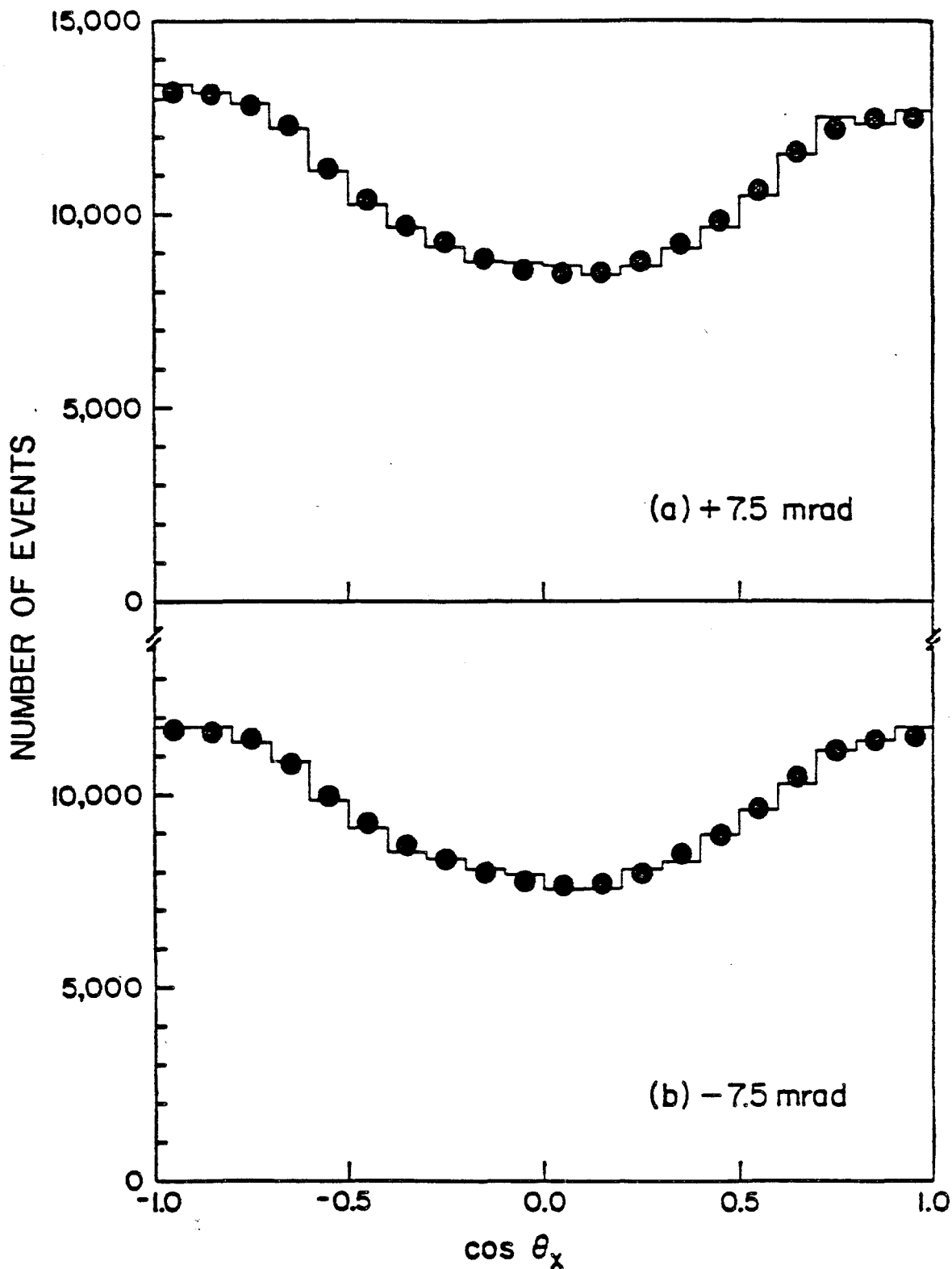


Fig. 34 The $\cos(\theta_x)$ distribution of neutrons in the Σ^- rest frame for $\Sigma^- \rightarrow n\pi^-$ decay. The distributions from both production angles, +7.5 (a) and -7.5 (b) are given. For comparison the distribution of the Internal Monte Carlo events (dots) is also shown.

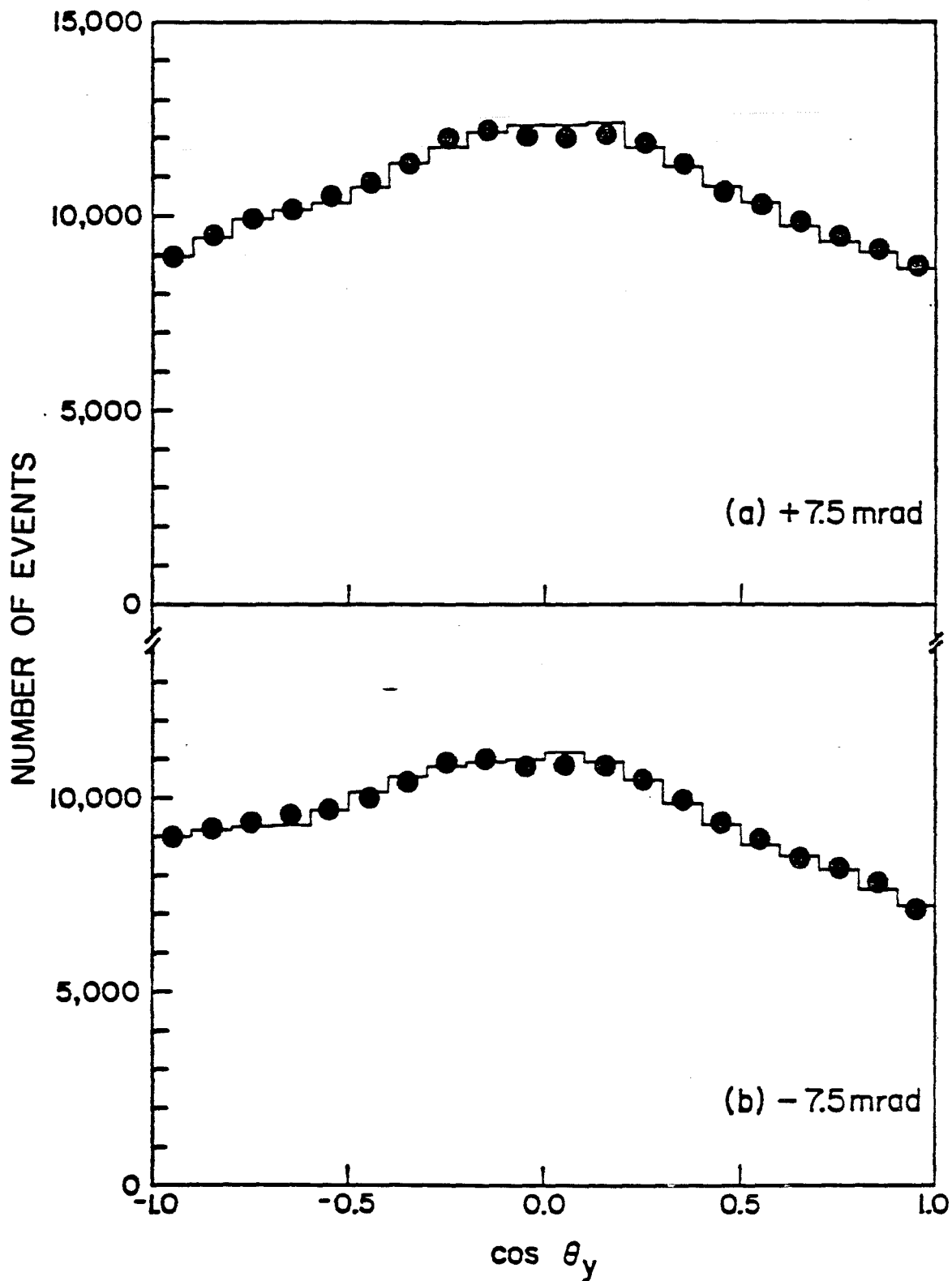


Fig. 35 The $\cos(\theta_y)$ distribution of neutrons in the Σ^- rest frame for $\Sigma^- \rightarrow n\pi^-$ decay. The distributions from both production angles, +7.5 (a) and -7.5 (b) are given. For comparison the distribution of the Internal Monte Carlo events (dots) is also shown.

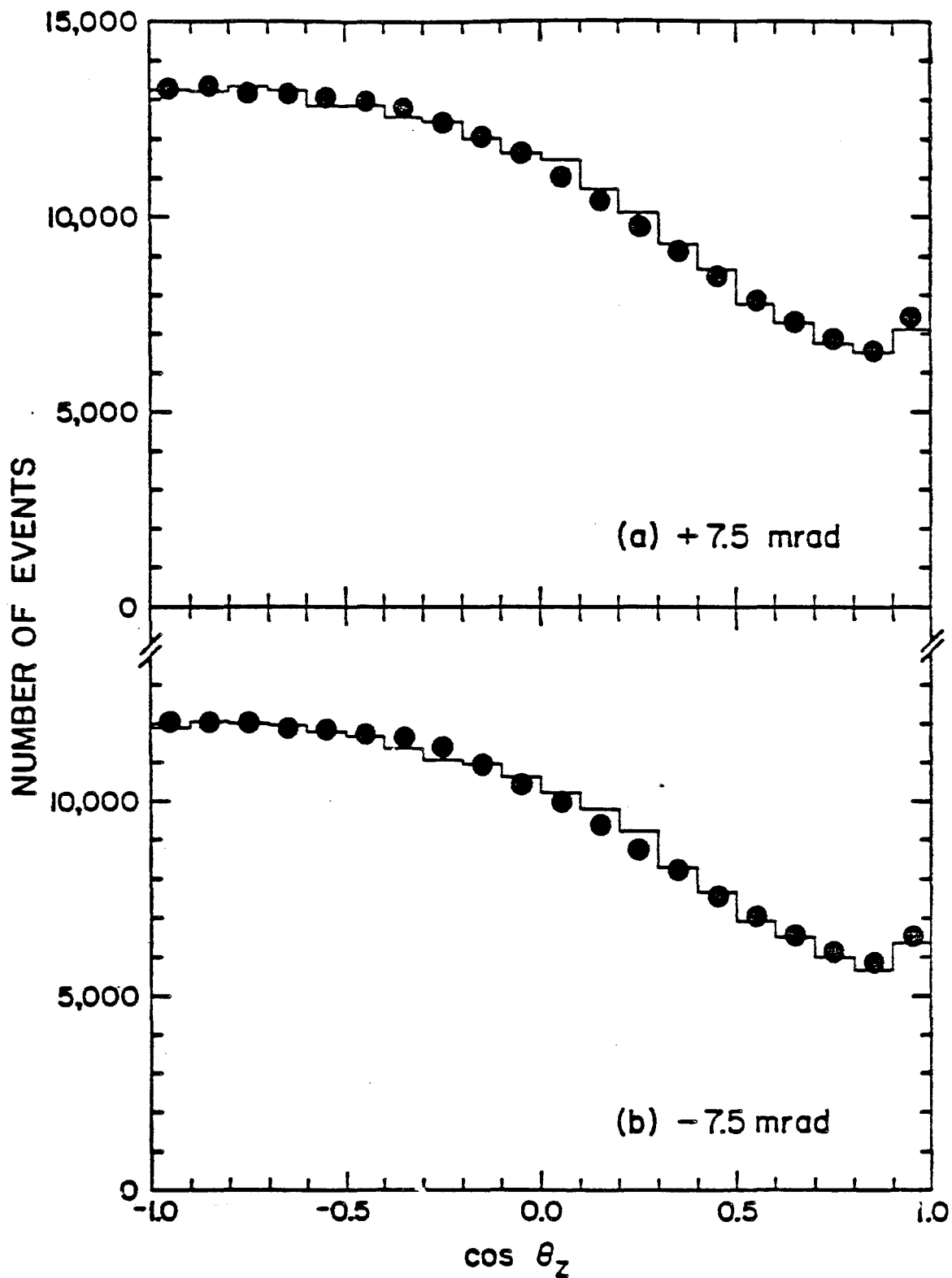


Fig. 36 The $\cos(\theta_z)$ distribution of neutrons in the Σ^- rest frame for $\Sigma^- \rightarrow n\pi^-$ decay. The distributions from both production angles, +7.5 (a) and -7.5 (b) are given. For comparison the distribution of the Internal Monte Carlo events (dots) is also shown.

APPENDIX 4

THE EFFECT OF BACKGROUNDS ON THE ASYMMETRY CALCULATION

We are interested in the way the presence of background influences the calculation of the asymmetry signals. Since the Ξ^- background is the largest source we will confine this appendix to its effect on our result. All other sources will have an effect less than the one described here.

Figures 37 and 38 show the "neutron" $\cos(\theta_x)$ and $\cos(\theta_z)$ plots of unpolarized Ξ^- events when reconstructed as Σ^- 's. Only those events that pass Σ^- identification cuts are plotted. For comparison with real data, see Figures 34 and 36. Two things are immediately obvious:

- 1) The $\cos(\theta_z)$ plot is extremely distorted due to the false kinematics and is not symmetric about zero.

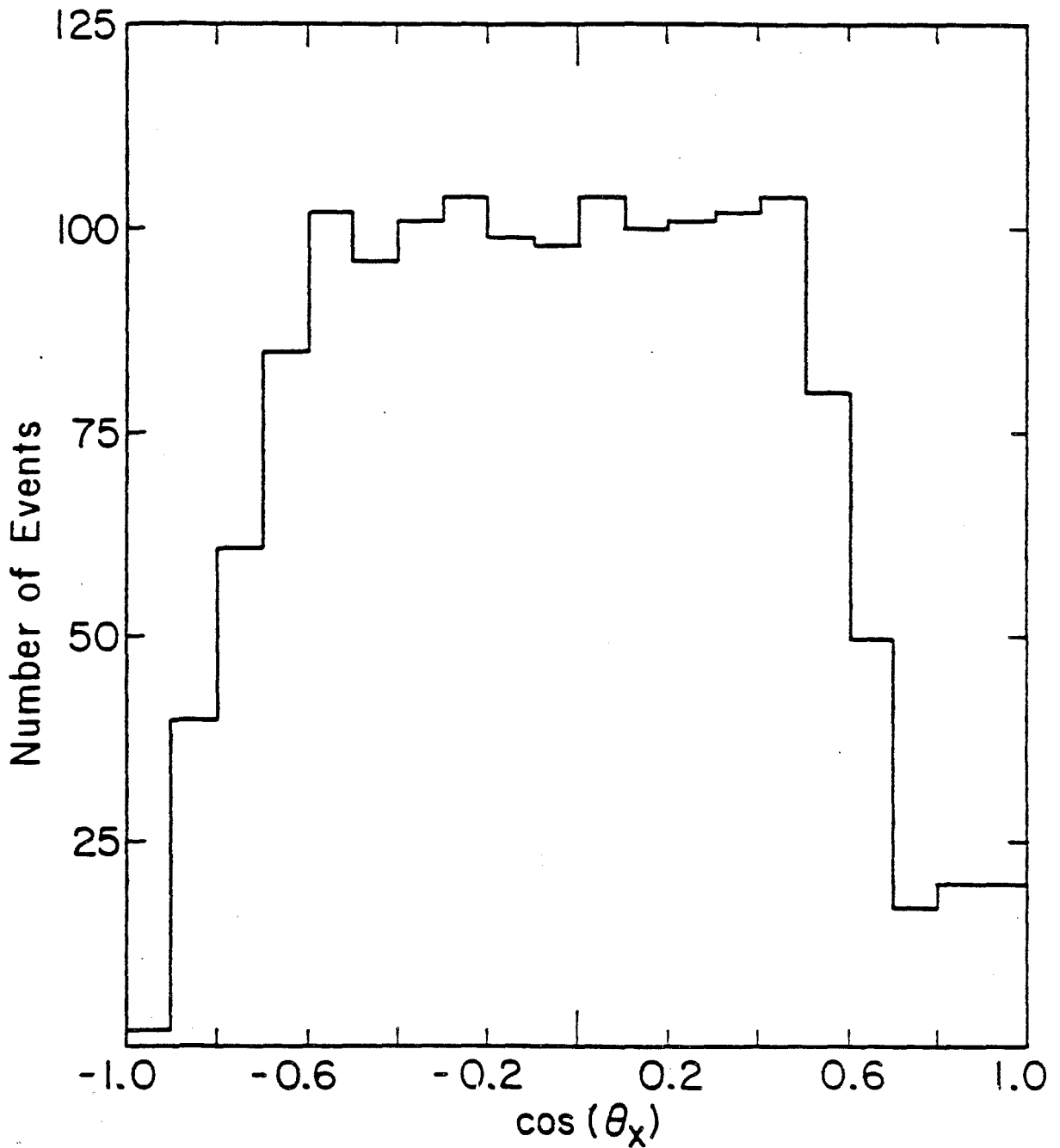


Fig. 37 The $\cos(\theta_x)$ distribution for the "neutron" from Monte Carlo $\Xi^- \rightarrow \Lambda^0 \pi^-$ events reconstructed as $\Sigma^- \rightarrow n \pi^-$.

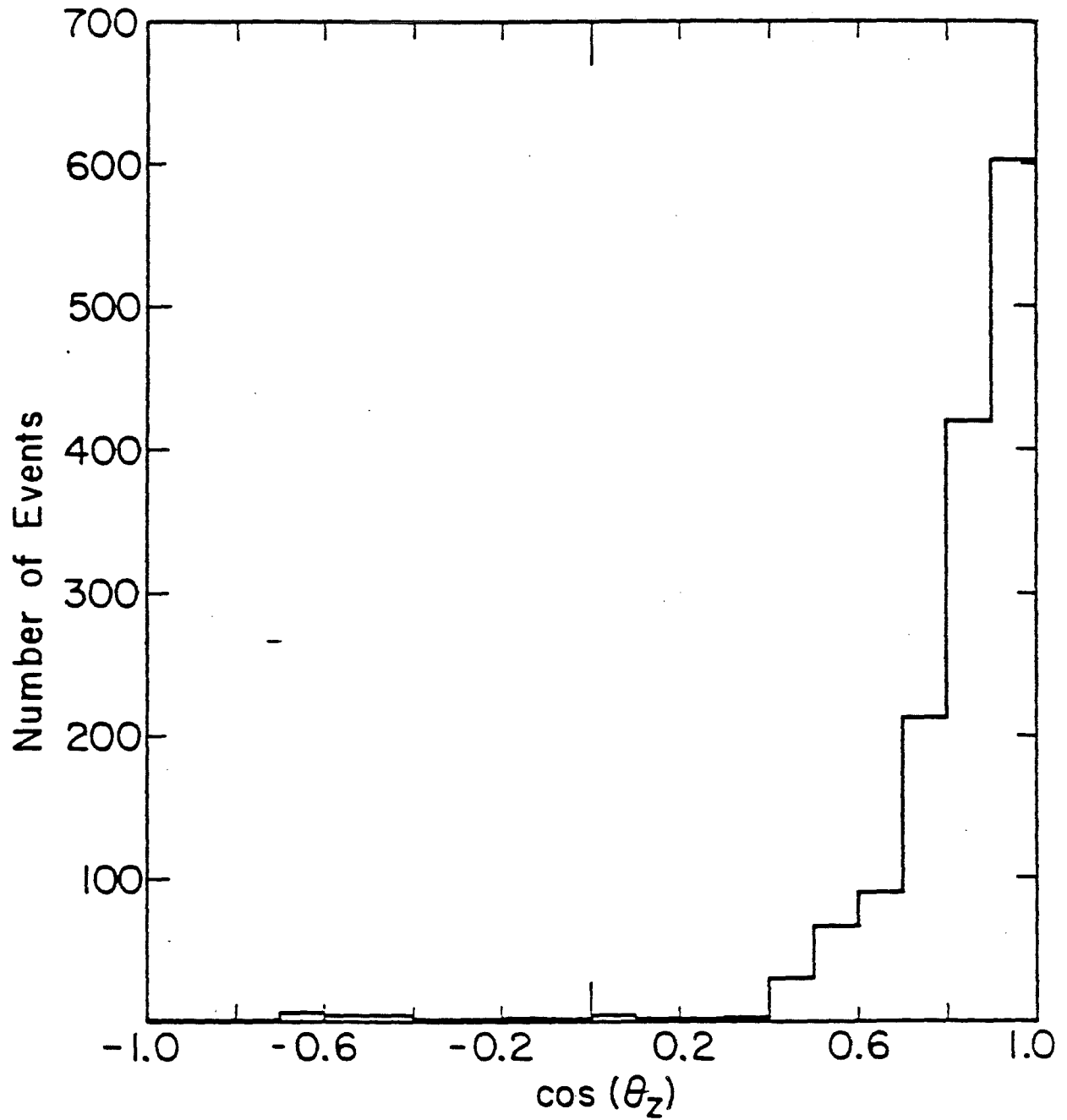


Fig. 38 The $\cos(\theta_z)$ distribution for the "neutron" from Monte Carlo $\Xi^- \rightarrow \Lambda^0 \pi^-$ events reconstructed as $\Sigma^- \rightarrow n \pi^-$.

- 2) The $\cos(\theta_x)$ plot is much less distorted and relatively symmetric about zero.

These two observations imply that the the largest bias will be produced in z , while the effect in x will be largely cancelled out by its symmetry about zero. Let us then consider the effect in z . The χ^2 for determining αP_z is given by:

$$\chi^2 = \sum_i (R_i - A_i (1 + \alpha P_z \cos(\theta_{z_i})))^2$$

where A is the appropriately normalized acceptance function defined in Appendix 3, R_i are the number of real events in $\cos(\theta_{z_i})$, αP_z is the asymmetry signal we are solving for and the sum runs over all the $\cos(\theta_z)$ bins. In practice 20 bins were used to cover the whole range in $\cos(\theta_z)$. The equation which determines αP_z is given by:

$$0 = \sum_i (R_i - A_i (1 + \alpha P_z \cos(\theta_{z_i}))) A_i \cos(\theta_{z_i})$$

or

$$\alpha P_z = \frac{\sum_i (R_i - A_i) A_i \cos(\theta_{z_i})}{\sum_i A_i^2 \cos(\theta_{z_i})^2}$$

Let us assume that there are no biases and the polarization is zero so that the asymmetry we find will be due to the effect of the Ξ^- background alone. We then

have,

$$(R_i - A_i) = 0 \quad \text{for all } i$$

We now introduce the background and ignore the extremely small effect due to the change in normalization. To simplify the calculation we further assume that the background lies completely in one bin, the k^{th} . Inspection of Fig. 35 shows that this is not a bad approximation for Ξ^- 's. These assumptions then give us:

$$(R_i - A_i) = 0 \quad \text{for all } i \neq k$$

so the equation for αP_z becomes,

$$\alpha P_z = \frac{(R_k - A_k) A_k \cos(\theta_{z_k})}{\sum_i A_i^2 \cos(\theta_{z_i})^2}$$

Without specific knowledge of A the sum in the denominator can not be performed, however the shape of the $\cos(\theta_z)$ plot for real Σ^- events (Fig. 37) allows for a crude approximation. We will assume that the acceptance function A is linear in $\cos(\theta_z)$. This approximation gives results very close to correct treatment and makes the calculation more transparent. Let A_i be:

$$A = A_0 - \frac{A_c}{2} \cos(\theta_z)$$

where $A_0 = \frac{N}{20}$ and N is the total number of real events. Then the denominator becomes:

$$\sum_i A_i^2 \cos(\theta_{z_i})^2 = \sum_i \left(A_0^2 - \frac{A_0^2}{2} \cos(\theta_{z_i}) + \frac{A_0^2}{4} \cos(\theta_{z_i})^2 \right) \cos(\theta_{z_i})^2$$

which reduces to:

$$\sum_i A_i^2 \cos(\theta_{z_i})^2 = A_0^2 \quad (7.7)$$

For the +7.5 production angle data the relative percentage of Ξ^- background after cuts was measured to be $0.256 \pm 0.003\%$. Assuming all of these events went into the $\cos(\theta_z)=1$ bin means a contribution to the asymmetry of:

$$\alpha_{P_+} = \frac{\left(\frac{A_0}{2}\right) (0.00256) (N) (1)}{A_0^2 (7.7)} = 0.0033$$

If the percentage of background in the -7.5 mr data were the same then the asymmetry calculated above would cancel completely when the two production angles were subtracted and would only contribute to the bias without affecting the result. However the measured percentage of Ξ^- background in the -7.5 mr data did differ slightly. It was measured to be $0.241 \pm 0.003\%$ or 6.7% lower than the +7.5 mr data. It produces an asymmetry of:

$$\alpha_{P_-} = \frac{\left(\frac{A_0}{2}\right) (0.00241) (N) (1)}{A_0^2 (7.7)} = 0.0031$$

When these 2 asymmetries are subtracted, cancellation is not complete and we obtain

$$\alpha_P = \frac{0.0033 - 0.0031}{2} = 0.0001$$

This signal is however completely negligible compared to our statistical error and can be safely ignored.

The above discussion was specifically considering the effect of a sample of UNPOLARIZED Ξ^- 's on the Σ^- asymmetry calculation. However it has been determined that the Ξ^- 's are produced polarized with a polarization of about 12%.⁽⁷⁾ Furthermore the polarization after precession lies all along $-x$ for positive production angle since $\frac{S_{\Xi}}{2} = 1$. Therefore since the asymmetry of the Λ^0 's from $\Xi^- \rightarrow \Lambda^0 + \pi^-$ decay is given by,

$$\frac{dN}{d\cos(\theta)} = 1 + \alpha_{\Xi} \bar{P}_{\Xi} \cos(\theta)$$

where $\alpha_{\Xi} = -.467 \pm .004$,⁽¹⁾ the magnitude of the asymmetry produced in x due to a .249% Ξ^- contamination would be:

$$(0.467)(0.12)(0.00249) = 0.00014$$

and would in fact not cancel in the subtraction procedure since the polarization changes sign between production

angles. Even so, the signal so produced is still much smaller than our statistical error and is therefore negligible.

REFERENCES

1. Particle Data Group, Rev.Mod.Phys. 51, 5283 (1980).
2. D.P.Barber et.al., Phys.Rev.Lett. 43 , 1915 (1979)
3. G.Bunce, R.Handler, R.March, P.Martin, L.Pondrom, M.Sheaff, K.Heller, O.E.Overseth, P.Skubic, T.Devlin, B.Edelman, R.Edwards J.Norem, L.Schachinger, and P.Yamin, Phys.Rev.Lett. 36 , 1113 (1976)
4. K.Raychaudhuri et.al., Phys.Lett. 90B , 319 (1980)
5. K.Heller, O.E.Overseth, G.Bunce, F.Dyđak, and H.Taureg, Phys.Lett. 68B , 480 (1977)
6. P.T.Cox, Ph.D. Thesis, University of Michigan UMHE-80-19, (1980) (unpublished)
7. R.Rameika, Ph.D. Thesis, Rutgers University (1981) (unpublished)
8. C.Wilkinson, R.Handler, B.Lundberg, L.Pondrom, M.Sheaff, P.T.Cox, C.Dukes, J.Dworkin, O.E.Overseth, A.Beretvas, L.Deck, T.Devlin, K.B.Luk, R.Rameika, R.Whitman, and K.Heller, Phys.Rev.Lett. 46 , 803 (1981)
9. R.Grobel, Ph.D. Thesis, University of Wisconsin (1980) (unpublished)
10. T.A.DeGrand, and H.I.Miettinen, University of California, Santa Barbara, TH-27 (1981)
11. K.Heller et.al., Phys.Rev.Lett. 41 , 607 (1978) See also Ref. 8.
12. See, for example, M.Leon, "Particle Physics - An Introduction", (Academic Press 1973)
13. P.T.Cox, J.Dworkin, O.E.Overseth, R.Handler, R.Grobel, L.Pondrom, M.Sheaff, C.Wilkinson, L.Deck, T.Devlin, K.B.Luk, R.Rameika, P.Skubic, K.Heller, G.Bunce, Phys.Rev.Lett. 46 , 877 (1981)

14. L.Schachinger, G.Bunce, P.T.Cox, T.Devlin, J.Dworkin, B.Edelman, R.T.Edwards, R.Handler, K.Heller, R.March, P.Martin, O.E.Overseth, L.Pondrom, M.Sheaff, and P.Skubic, Phys.Rev.Lett. 41 , 1348 (1978)
15. G.E.Brown, M.Rho, and V.Vento, Phys.Lett. 97B, 423 (1980)
16. A useful summary of the models for magnetic moments has been made by J. Rosner, in Proceedings of the Twentieth International Conference on High Energy Physics, Madison Wisconsin 1980.
17. R.G.Sachs, Phys.Rev. D23 , 1148 (1981)
18. R.B.Teese, Phys.Rev. D24 , 1413 (1981)
19. M.A.B.Beg, B.W.Lee, A.Pais, Phys.Rev.Lett. 13 , 514 (1964)
20. A.DeRujula, H.Georgi, S.L.Glashow, Phys.Rev. D12 , 147 (1975)
21. D.A.Geffen, W.Wilson, Phys.Rev.Lett. 44 , 370 (1980)
22. N.Isgur, G.Karl, Phys.Rev. D21 , 3175 (1980)
23. M.Bohm, R.Huerta, A.Zepeda, paper # 819, XX International Conference on High Energy Physics, Madison, Wisconsin (1980)
24. R.Verma, "Magnetic Moments of Baryons in Broken Unitary-Spin Symmetry", Univ. of Alberta, THY-5-80 (1980) (unpublished)
25. S.Oneda, et.al., paper # 772, XX International Conference on High Energy Physics, Madison, Wisconsin (1980)
26. Y.Tomozawa, Phys.Rev. D19 , 1626 (1979)
27. H.J.Lipkin, Phys.Lett. 89B, 358 (1980)
28. B.L.Roberts, C.R.Cox, M.Eckhause, J.R.Kane, R.E.Welsh, D.A.Jenkins, W.A.Lam, F.D.Barnes, R.A.Eisenstein, J.Miller, R.B.Sutton, A.R.Kunselman, R.J.Powers, and J.D.Fox, Phys.Rev. D12, 1232 (1975)

29. G.Dugan, Y.Asano, M.Y.Chen, S.C.Cheng, E.Hu,
L.Lidofsky, W.Patton, C.S.Wu, V.Hughes, D.Lu,
Nucl.Phys. A254 , 396 (1975)
30. see for example V.Bargmann, L.Michel, V.L.Telegdi,
Phys.Rev.Lett. 2 , 433 (1959)
31. P.L.Skubic, Ph.D. Thesis, University of Michigan
Technical Report, UMHE-77-32, (1977)
32. R.Thun, C.W.Akerlof, P.Alley, D.Koltick,
R.L.Loveless, D.I.Meyer, M.Zumberge, D.Bintinger,
R.A.Lundy, D.D.Yovanovitch, W.R.Ditzler, D.A.Finley,
F.J.Loeffler, E.I.Shibata, and K.C.Stanfield,
Nucl.Inst.Meth. 138, 437-444 (1976)
33. G.Bunce, Nucl.Inst.Meth. 172, 553 (1980)

CURRICULUM VITAE

Leslie Ludwig Deck

- 
.
- 
.
- 1972-1976 Physics major, Rutgers University, New Brunswick, New Jersey.
- 1974-1976 Worked on an R & D project for controlled nuclear fusion.
- 1976 B.A., Rutgers College.
- 1976-1981 Teaching Assistant for undergraduate Physics recitations and advanced laboratories.
- 1978-1981 Graduate Assistant in High Energy Experimental Physics. Worked with the Neutral Hyperon group at Fermi National Lab, Batavia, Illinois. Active participation in E495, E361, and, E620.
- 1979 Worked on conversion of the Neutral Hyperon beam at FNAL to a charged hyperon beam designed to detect and measure polarizations and magnetic moments for the Ξ^- , Σ^- , and Σ^+ .
- 1980-1981 Thesis Experiment--Completed data taking and analysis of the Σ^- polarization and magnetic moment.
- 1981 Article: "Polarization of Σ^+ Hyperons Produced by 400 GeV Protons", Physical Review Letters, Vol.46, No.13, p. 803.
- 1981 Article: "Precise Measurement of the Ξ^0 Magnetic Moment", Physical Review Letters, Vol.46, No.14, p. 877.